UNIVERSITÀ DEGLI STUDI DI PADOVA

Dipartimento di Ingegneria Industriale DII

Corso di Laurea Magistrale in Ingegneria Aerospaziale

TESI DI LAUREA

SAFETY RANGE AND LOAD ANALYSES OF A HYBRID SOUNDING ROCKET

Relatore: Prof. Barato Francesco
Correlatore: Prof. Pavarin Daniele

Lucia Zeni

Anno Accademico 2019-2020

" Don't judge each day by the harvest you reap but by the seeds that you plant."

Robert Louis Stevenson

Abstract

T4i - "Technology for Propulsion and Innovation", a spin-off company of the University of Padua, in collaboration with the university is developing a sounding rocket propelled by a hybrid engine. The sounding rocket will serve as a technology demonstrator for the engine developed by the company. The objective is to start a launch campaign and reach an altitude of at least 10 km with the first flight. Afterwards, thanks to this first experience, it will be possible to improve the performance and reach higher altitudes of major scientific interest. For the success of the sounding rocket launch, it is fundamental to ensure the rocket does not break during its flight and that in every phase, from the rocket preparation on the rail to its recovery, the safety requirements are respected. Thus, a load analysis and a safety range analysis have been carried out. The loads acting on the rocket during its flight have been analysed. This analysis has allowed to identify the sections on which the loads have higher magnitude. These are the most critical sections of the rocket and the loads acting on them must not cause a structural failure. Before the real launch campaign can begin, all the appropriate authorisations must be obtained. A safety analysis must be carried out to grant that the rocket during all its flight phases does not represent a threat to public safety. In particular, the rocket should not cause damages to buildings or casualties among the populations. To evaluate the casualty probability, as a first step the nominal dispersion impact area is determined with a Monte Carlo analysis. The focus is then shifted towards the possibility of an accident, which could cause the rocket trajectory and impact point to deviate significantly.

Sommario

T4i - "Technology for Propulsion and Innovation", uno spin-off dell' Università degli Studi di Padova, in collaborazione con l'università sta sviluppando un sounding rocket a propulsione ibrida. Il sounding rocket servirà come dimostratore tecnologico per il motore sviluppato dall'azienda. L'obbiettivo è di poter iniziare la campagna di volo e di riuscire a raggiungere un'altitudine di almeno 10 km con il primo lancio. In seguito, grazie a questa prima esperienza, sarà possibile migliorare le performance per arrivare ad altitudini più elevate e di maggiore interesse scientifico. Per il successo della missione è fondamentale che, in primo luogo, il razzo non subisca danni o rotture a causa dei carchi che agiscono su esso ed, in secondo luogo, che in ogni fase, dalla preparazione in rampa al recupero, siano rispettati i requisiti di sicurezza. Si sono perciò eseguite un'analisi sui carichi e un'analisi sulla sicurezza. Si sono analizzati i carichi agenti sul razzo durante le fasi di volo evidenziando le sezioni in cui risultavano essere più gravosi. Queste sono le sezioni più critiche del razzo ed è importante che i carichi agenti su di esse non possano causare un fallimento strutturale. Prima di poter iniziare la vera e propria camapgna di lancio si devono ottenere tutte le opportune autorizzazioni. É quindi necessario eseguire un'analisi di sicurezza in modo da garantire che durante il volo il razzo non rappresenti un pericolo per la sicurezza pubblica, e, nello specifico, non possa causare danni agli edifici o perdite alla popolazione. Per poter determinare la probabilità che il razzo causi delle perdite, come primo step si è determinata la zona nominale d'impatto attraverso un'analisi Monte Carlo. L'attenzione si è poi spostata sulla possibilità di avere incidenti durante il volo, i quali possono modificare in maniera significativa il punto d'impatto al suolo.

List of Figures

List of Tables

Contents

Introduction

T4i - Technology for Propulsion and Innovation, a spin-off company of the University of Padova, is developing a sounding rocket as a technology demonstrator for their hybrid technology. The hybrid engine developed by *T4i* is powered by hydrogen peroxide and a grain of paraffin, respectively as liquid oxidizer and solid fuel. The main objective of this project is the developing, testing and launch campaign of the sounding rocket. The target of the first launch is to reach an altitude of about 10 km and later to recover the entire rocket. The recovery will allow a thorough analysis of the engine and of the whole rocket after the flight. With the experience gathered thanks to this first flight, the rocket could be improved and, if necessary, redesigned in some of its components to achieve better performance and reach higher altitudes of greater scientific interest.

The work presented in this thesis is divided into five main chapters. The first chapter provides a general overview of sounding rockets and hybrid propulsion history. Then, the sounding rocket developed by *T4i* is briefly described. After this first general descriptions, the rocket dynamic model is presented. The focus shifts then towards the analyses effectuated, which are the Load analysis and the Safety Range analysis.

Sounding rockets are often used for experiments and scientific measurements. The sounding rockets have become popular in the last years thanks to some peculiar characteristics as a relatively easy and cheap access to space and their usefulness as validation devices for new technologies. More important, sounding rockets are a great learning opportunity both for students and for research projects because they cover the entire development phases, from the preliminary design to the launch phase. Thus, sounding rockets allow to build new experience on which bigger and more advanced programs can be based.

Hybrid propulsion systems are characterized by the oxidizer and fuel stored separately, one in solid phase and the other in liquid or gaseous phase. Hybrid systems have unique characteristics and have been attracting more and more attention in the last years. Among these, there are their intrinsic safety, mass flow control, low costs and low environmental impact. Unfortunately, among the many advantages, the hybrid systems have also some disadvantages that prevented their development contemporaneously to the liquid and solid systems in the first decades of rocket science. Thus, the hybrid systems are less advanced than the other systems. To fully develop the hybrid technology, the classical issues of hybrid propulsion must be resolved maintaining at the same time all the advantages inherent to this propulsion system, like simplicity and safety.
In the last decades, several hybrid sounding rockets have been launched setting new records. Among them, there are the Atea I, the Stratos rockets, the Heros rockets and Nucleus. With the launch of the Atea I in 2009, Rocket Lab became the first private company of the southern hemisphere to reach space. In the projects, the rocket should have reached an altitude of more than $100\,km$ and a velocity above Mach 5. However, since the second stage was never recovered, its actual performance were never assessed. The Stratos rockets have been developed by Dare - Delft Aerospace Rocket Engineering - a team of students of the Delft University of Technology. The Heros rockets have been developed by HyEnD - Hybrid Engine Development - a student-based project at the University of Stuttgart. In 2016, the Heros III rocket reached an altitude of $32.2\,km$ setting the altitude record for European students and amateur rocketry and the world altitude record for hybrid rockets built by students. Nucleus has been developed by Nammo as a step in the demonstration of the feasibility of hybrid propulsion for sounding rocket and micro-launcher. In 20018, it was launched from Andøya Space Centre in Northern Norway. It reached an altitude of $107\,km$ and was the first European rocket to reach space in more than 50 years. These examples show the potential of hybrid rocket propulsion, and in particular of the hybrid sounding rockets.

The sounding rocket behaviour and trajectory are evaluated using a 6 Degree of Freedom in-house code. A correct trajectory simulation implies a correct and exhaustive description of the characteristics of the rocket, which

include the external geometry with the total length and diameter. Other parameters important in the rocket description are the mass, its distribution and variations, and the inertias.
The trajectory evolution in time is determined from the aerodynamic forces, i.e. the lift and the drag, from the jet damping and from the presence of misalignments, like misalignments in the thrust vector or in the fin attachment to the main body. These forces can create moments around the centre of gravity of the rocket. The aerodynamic forces are determined with the aid of another code, which evaluates the aerodynamic coefficients with respect to the flight condition, i.e. altitude, Mach velocity and angle of attack. The thrust can be characterized by a not perfect misalignment with the rocket axis. This misalignment can be described with four parameters which delineate the absence of perfect centering of the thurst application point, the in-plane and off-plane angles and the rotation between the body system of the rocket and of the system in which the thrust is defined. The fin misalignment has different effects on the rocket dynamic. The fin misalignment can be expressed with three components, two of which create various forces and moments on the rocket, while the third creates a spinning moment.

In the Load Analysis, the rocket reactions to the applied loads have been evaluated and, more important, the ability of the main structure to withstand all the loads without suffering deterioration or permanent deformation has been verified.
The loads can have different natures and causes. They can derive, among the others, from the handling and transportation phases, from the flight loads, from the vibrations or shocks. This analysis has focused on the loads acting during the flight phases. This choice derives from the unpredictable nature of the other types of load and because the flight ones are considered to be among the heaviest the rocket could experience.
The structure reacts to the applied loads developing axial and shear force and bending moment. These can then be translated into load diagrams in order to evaluate the sections of the rockets where the loads are more critical. The magnitude of the loads on the entire rocket, and more specifically on these sections, must not cause a structural failure of the rocket or any of its components.

The focus was then shifted towards the Safety Range analysis. As a

safety requirement, a casualty probability lower than 10^{-6} must be ensured. To have a higher safety margin and simplify the analyses, instead of evaluating the casualty probability if the rocket falls on the ground, a requirement of a land impact probability lower than 10^{-6} has been set.
To ensure the respect of the safety requirement set, different analyses have been carried out. The analyses have been divide into different categories. The first distinction is based on the type of trajectory: nominal or non-nominal. Non-nominal trajectories are flight paths where manufacturing errors, wind and other statistical or deterministic effects bring the rocket to deviate from an undisturbed trajectory, i.e. nominal. The distinction on the type of trajectory is made with the flight path angle, if possible, or with the axial component of the velocity. During thrusted flight, the axial component must always increase and the flight path angle must always decrease. If these conditions are not met then the rocket is flying on a non-nominal trajectory. A second distinction is on the absence or presence of accidents, like a nozzle-turn malfunction or the fin loss.
In the absence of accidents, it is possible to evaluate the nominal dispersion area using the Monte Carlo technique, taking into account all those parameters whose values could vary due to manufacturing errors or atmospheric conditions at launch. From the Monte Carlo results it is possible to determine an impact envelope and the probability of a rocket impact behind the launch site. In the analyses without accidents is included the evaluation of the wind influence. The wind conditions could change as the rocket is waiting for the lift-off on the launch pad or as it is flying. Thus, it is important to determine how any changes in the wind magnitude or direction could influence the rocket trajectory and impact point.
A first possible accident that should be analyzed is the possibility of an explosion of the HTP stored in the oxidizer tank. The explosion could occur both during ground operations and flight. The blastwave overpressure generated could create casualties and damages to buildings, thus it is important to evaluate the range in which an explosion could be of concern for public safety. Another consequence of an explosion is the generation of fragments. These can be created by the different parts of the rocket, from the tank itself to the metallic parts of the fluidic lines and the catalytic. The blastwave accelerates them and, thus, the maximum distance they can

travel must be evaluated.
After an evaluation of the possible failure and response mode of the rocket, two major accidents are chosen for further analyses: the nozzle-turn malfunction and the fin loss. In the event of an accident, a destructive Flight Termination System is installed on the sounding rocket.
The Flight Termination System is composed of two independent systems, each one including a battery, an electric actuation and an explosive device. On activation it should break the rocket into two main parts, breaking the tank lower end-closure and releasing the HTP still stored in it before hitting the ground. Also, the explosion should cut the feeding line shutting-off the main engine. With the FTS activation, in addition to the two main parts, several smaller debris could be generated. The main objective of the FTS is to prevent the rocket or any of its parts from exiting the safe zone and reach areas where it could cause damages or casualties. The Flight Termination System is not activated instantaneously in the event of an accident, but its activation time depends on the flight conditions and takes into account the human response time. The activation time is of 3 *seconds* or 1 *second* depending on the rocket flying condition. The different times correspond to two different alarm codes: green code and orange code. The green code corresponds to a nominal trajectory, while the orange code corresponds to a non-nominal trajectory.

The analyses carried out in this thesis allow to ensure that the sounding rocket respects the safety requirements considered during all the phases of its flight. Thus, the rocket during flight can withstand all of the applied loads and it does not pose any threat for public safety.

CHAPTER 1

Sounding Rocket and Hybrid Propulsion Overview

1.1 Sounding Rockets

Sounding Rockets, also known as research rockets, are sub-orbital rockets often used for experiments or scientific measurements. Their name comes from the nautical terms "to sound" which historically had the meaning "to take measurements", making their names in line with their use. Starting from the '50s sounding rockets were used mostly for meteorological measurements and scientific studies of the upper layers of the atmosphere. Their peculiar characteristic is to reach the upper layer of the atmosphere but not to end up in space, in fact, they are sub-orbital rockets and thus they mainly follow a parabolic trajectory and end up returning to the ground.

The principal components of a sounding rocket are: the propulsive system, which historically is a solid-state propellant and more recently a hybrid system; the control system, which includes all the instruments necessary for the tracking, the data transfer and the recovery modules; and the scientific payloads, which depend on the specific objectives of each launch and can therefore be measurements instruments, experiments, etc...

In recent years the popularity of the sounding rocket has been growing thanks to some peculiar characteristics which make them unique in the rocket area. Some of these characteristics are listed below

- *They provide unique conditions for scientific research:* Considering their parabolic trajectory and high altitudes reached, they permit to have unique conditions which allow specific experiments on the

upper atmosphere and microgravity experiments. The microgravity can last up to 20 minutes depending on the altitude reached and on the specific conditions of the flight. After the flight, the rocket can be entirely recovered or, where this would results too complex, the recovery system can be designed to act on the payload sacrificing the rest of the rocket. The payloads and the experiments can thus be recovered and studied or when necessary re-launched;

- *They provide relatively easy, quick and cheap access to space:* Sounding rockets can reach high altitudes but are not designed to enter into orbit. Not having to end up in orbit, their propulsive systems are less complex than others and, thus, their costs are not as elevated. Since payloads or instruments can be recovered, their costs can be spread over multiple launches;

- *They are useful for device validation and new technologies development:* Sounding rockets are the perfect vectors to test new technologies especially thanks to their relatively low complexity and low costs. In fact, new systems not yet tested or properly validated don't flight on full-blown satellite programs since their failure could damage other payloads or the entire satellite;

- *Learning:* Considering the characteristics described above, sounding rockets are the perfect programs for students or novice engineers to follow a research project in all its phases, from early developments to launch. Thus, sounding rockets allow to build new experience on which bigger and more advanced programs can be based.

1.2 Hybrid Propulsion

Sounding rockets and, more in general, all rocket and orbital vectors have three possible types of propulsion systems: solid, liquid and hybrid. They differ in the phase in which the propellant is stored. In solid systems, propellant and oxidizer are mixed together to create a solid matrix which is then stored inside the combustion chamber. In a liquid system, oxidizer and propellant are stored in liquid phase in different tanks and they are

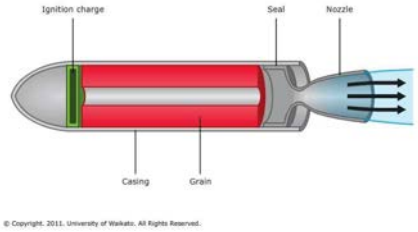

(a) Solid system

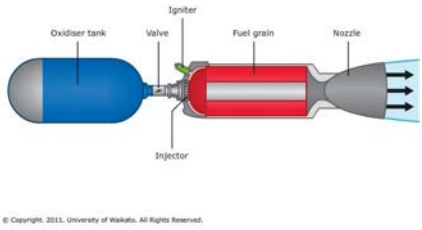

(b) Hybrid system

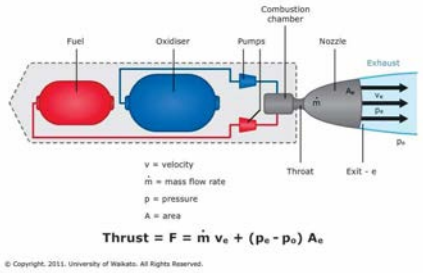

(c) Liquid system

Figure 1.1. *Solid, Liquid and Hybrid Propulsive System Schematics.*

later injected in the combustion chamber. In more general terms, a liquid system can include also those systems in which oxidizer and propellant are stored in gaseous or gelled form. Following this inclusion, a liquid system can be described as a propulsive system in which oxidizer and propellant are stored separately in tanks and they mix after their injection in the combustion chamber. For a long time, hybrid systems were considered to be intermediate between solid and liquid systems, having no major advantage in performance. However, hybrid engines have unique characteristics and many differences from solid and liquid systems. A schematic of the three propulsion system is shown in figure 1.1.

A hybrid propulsion system sees one of the components stored in liquid, gaseous or gelled phase in a tank and the other is stored in solid form inside the combustion chamber. Two main configurations of hybrid systems exist: classical and reverse. The classical configuration has the oxidizer in liquid form while the propellant is stored inside the combustion chamber in solid form. The reverse configuration has the propellant in the liquid form while the oxidizer is solid. Classic and reverse configuration schematics are shown in figure 1.2 along with other possible schematics.

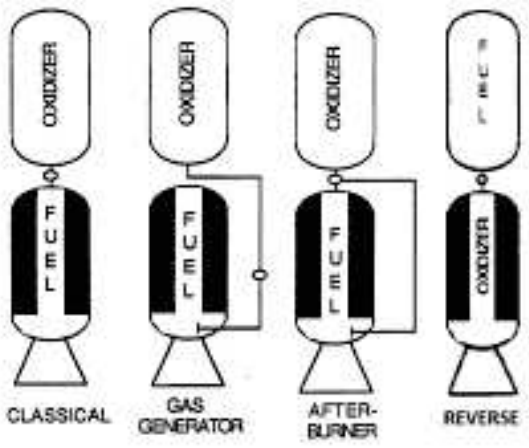

Figure 1.2. *Examples of possible hybrid schematics.*

The most part of the work up to now on sounding rocket regards the classical configuration. This depends on the higher energetic content of liquid oxidizer than solid ones. Exceptions are cryogenic oxidizers, like solid oxygen which can be seen as a solidified version of liquid oxygen. Storing a cryogenic solid is even more complex than storing their liquid counterparts, reason why cryogenic solids are not used. An almost infinite combination of solid fuels exists for hybrid propulsion while generally, the choice of oxidizer is much limited, both in solid and liquid form. Moreover, manufacturing a solid oxidizer requires a binder. Considering the different characteristics of both the classical and reverse configuration, most of the research done so far has focused on the classical configuration.

Up to now hybrid systems have received low attention and the focus was on solid and liquid engines. Considering the characteristics of the various systems, military and commercial market preferred solid and liquid, leaving the hybrid systems low space to develop. Hybrids found their slot in research and academic and amateur projects. The reason for that is related to the peculiar characteristics of the three systems and the requirements deriving from the historical period in which rocket science had its major developments. In fact, space programs had their major advancements after the Second World War and during the Cold War. No surprise if extensive investments push forward those systems that most interested the military.

Solid engines are simple, can be prepared and remain ready for launch for long times without excessive problems and their impulse density makes them ideals for applications with strict requirements on dimensions like military missiles, sounding rockets and boosters. Liquid engines have a high specific impulse, can be started and turned off several times making them ideals for launchers and spacecraft. Historically not much space was left for the development of hybrid engines.

Most of the studies and the advancements in rocket science date back to the '50 and '60. To those decades trace back most of the designs and tests on the technologies used in the following years. Only the most promising technologies were chosen for extensive further works. Due to some issues, hybrid engines were left out of this main growth. The impact of this exclusion still slows down the advancement of hybrid systems. After the first few decades of the space era, the investments began to reduce more and more preventing the hybrid engines to reach a level of maturity similar to solid and liquid. In the last years, the propulsive system requirements have undergone deep changes, more attention is now given to safety, reliability, costs and environmental impact. These changes shifted the attention of the space sector towards hybrid systems.

In the past hybrid propulsion was seen as an intermediate system between solid and liquid. However, it is important to underline how it has unique peculiarities that make it a completely different propulsion type and not just an in-between. In a solid engine, fuel and oxidizer are mixed intimately in the grain and have a specific and fixed O/F ratio. The propellant burns developing a thin flame close to the surface, only a few micrometers from it. The flame position influences deeply the characteristics of the combustion process. The amount of propellant which enters the flame depends on the linear regression of the grain surface, which in turn depends on the chamber pressure. The average O/F ratio is dependent on the grain composition and on the mass flow that enters the flame and can be controlled with a proper design of the fuel grain. In a liquid engine, fuel and oxidizer are injected into the combustion chamber with a feeding system. The O/F ratio depends on the mass flows injected. The total mass flow and thus the O/F ratio can be controlled, at least nominally with the feeding system. Generally in a hybrid engine, the oxidizer is stored in a tank and is injected

at the head end of the combustion chamber mixing with pyrolyzed fuels in a macroscopic turbulent diffusion flame. The regression rate depends on the convective heat exchange between the flame and the fuel surface. In a hybrid engine, the oxidizer mass flow can be controlled with the feeding system, while the fuel mass flow is dependent on the complex physic of its coupled fluid dynamic/combustion. The regression rate in a hybrid has a time and space variability. The O/F ratio and the total mass flow are not independent variables. This complex coupling between motor parameters, the difficult prediction/scaling and the space variability of hybrid regression makes hybrid physics and design more complex and difficult to deal with. This added complexity has always hampered the realization of a competitive hybrid rocket unit. Due to its peculiar characteristics, hybrid propulsion has several advantages compared to solids and liquids. Here a general list:

- *Safety:* The fuel is inert and can be manufactured, transported and handled safely as standard commercial products. The system is non - explosive because an intimate mixture of oxidizer and fuel is not possible. NASA classifies hybrid $LOX - HTPB$ (liquid oxygen / hydroxylterminated polybutadiene) combination as 0 TNT equivalent. In case of an abort procedure, the motor can be stopped turning off the liquid flow. Unlike solid rockets, fuel grain cracks are not catastrophic because burning occurs only when the fuel encounters the oxidizer flow. Hybrid combustion is diffusion-controlled so it's usually not pressure-sensitive as in liquid and solid systems. This in turn makes hybrid propulsion less prone to catastrophic failures due to thermoacoustic instabilities or other parameters shifting outside nominal conditions. Hybrid failures are usually benign in nature;

- *Reliability:* A hybrid rocket requires roughly only half of the components of a liquid motor. Compared to solid motors, the grain is much more insensitive to defects. Being diffusion-controlled, hybrid combustion is more tolerant than in both solid and liquid rockets;

- *Mass flow control:* The engine can be throttled by modulating only the liquid flow rate. This is simpler than in liquid propulsion where two liquids have to be modulated simultaneously. This doesn't require

only double plumbing but also synchronization between the two flows. The engine can be started and stopped several times if a suitable ignition system is used;

- *Propellant versatility:* The selection of propellants is (nominally) much greater than with either solid or liquid systems. However, the focus has been directed to a narrower band of combinations. Liquid oxidizers are more energetic than solid oxidizers used in solid propulsion. Metals particles can be added easily in a solid matrix to improve performances liquid systems, where the formation of slurries implies several drawbacks, such as sedimentation and issues in feeding-pressurization and atomization issues;

- *Temperature sensitivity* Because the temperature effect on the burning rate is small (as in liquid systems), ambient launch temperature variations have little effect on operating chamber pressure. Thus, the concern (typical for solid rockets) in designing for a maximum expected operating pressure (MEOP) is greatly reduced (this claim is partially negated in case of self-pressurized oxidizer);

- *Propellant specific impulse and density:* Hybrid rockets have theoretical specific impulse higher than solid ones and comparable to liquid ones, except for those using cryogenic fuels. With the addition of metals in the fuel grain, the specific impulse of hybrid systems can be even higher than the one of liquid rockets of the same class. Indeed, the highest possible experimental has been achieved with a tribrid configuration. The density impulse is lower compared to solid systems, but nominally higher compared to liquid ones, particularly for metal loaded fuels;

- *Low cost:* Considering the components composing the inert mass fraction of a rocket propulsion system the cost of a hybrid should stay between the more complex and expensive liquid systems and the simpler and cheaper solid ones. However, the total operational costs of a hybrid should take advantage of its safety characteristics and inert propellant. Manufacture of the fuel can be done in a commercial facility that does not require the large areas and many solid-propellant

manufacturing facilities. Furthermore, the system can tolerate large design margins, resulting in lower fabrication costs. Transport and handling costs are greatly reduced;

- *Low environmental impact:* Several low-polluting propellant combinations are possible for hybrid propulsion; many of them have been commonly used.

Unfortunately, hybrid rockets have also some disadvantages:

- *Low regression rate:* Hybrid systems are generally characterized by low regression rates. This in turn requires a large burning area to achieve the required thrust. This large area could be obtained with a very long combustion chamber resulting in a too-long motor. Moreover, the resulting web thickness is small concurring to a very poor volume loading (fuel volume/total volume). The problem is increased with scale-up for several reasons. First, the port area is proportional to the thrust while the web thickness is proportional to the product of the burning time with the average regression rate. Usually, burning time increases with scale-up much more slowly than thrust, resulting in a much higher ratio between the internal diameter and web thickness. Moreover, hybrid regression rate decreases with scaling, exacerbating the issue. A better alternative is the use of a multiport grain, some example of multiport configurations are reported in figure 1.3. However, multiport design implies several other problems, like high residuals, deviations of regression rate for different ports, change of the port shape with time, structural issues (e.g. need for web support), generally higher O/F shift than single-port design (even stronger if merging of ports is allowed), increased complexity and manufacturing costs. Several ways to increase the regression rate have been proposed and tested; almost no one has reached operational status, but some of them present an interesting potential for the future, particularly for up to medium scales;

- *Packaging issues:* In a liquid rocket the large part of the system is composed of the storage propellant tanks. This is increased particularly for low thrust to total impulse ratios (e.g. spacecraft). Tanks can

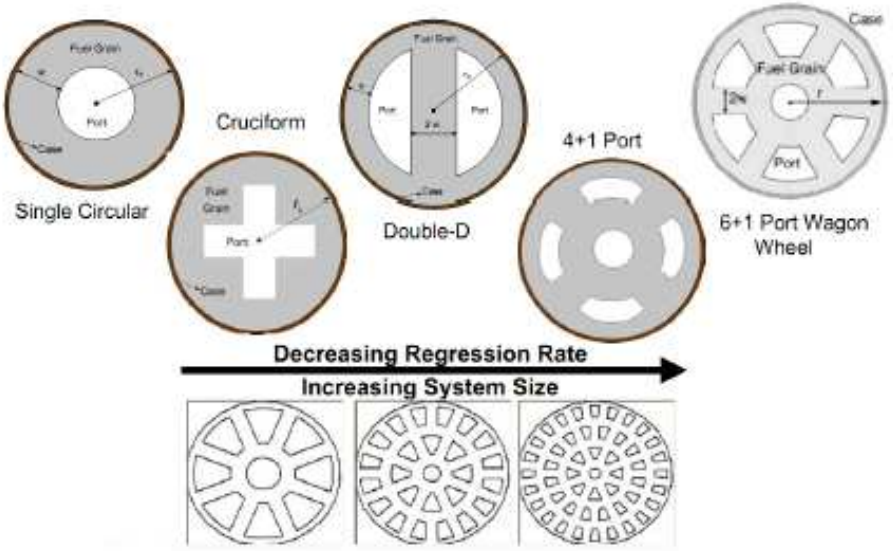

Figure 1.3. *Examples of multiport grain configurations.*

be easily packaged choosing different configurations in terms of tank number, shape and positions. Solid rockets are composed mainly of the combustion chamber that encloses the solid grain (plus the nozzle). Several geometrical solutions are available for solid motors allowing to fulfil multiple different mission constraints (e.g. different L/D ratios), moreover, the propulsion engineer can tailor the regression rate and the grain shape for the specific needs. In a hybrid rocket, the liquid oxidizer can be easily packaged as in a liquid rocket. The hybrid combustion chamber geometry is dictated by the solid fuel envelope. Due to the complex dependency of the hybrid regression rate on several parameters (like oxidizer flux), it is not possible to easily alter geometries as in solid propulsion where the mass flow is readily related to the burning area. On the contrary in a hybrid motor the fuel mass flow changes even with a constant burning area. That s why a constant burning area (e.g. star-shaped) grain produces a neutral burning in a solid while it is strongly regressive in a hybrid configuration [21](inducing also a significant O/F shift for a constant oxidizer flow). For this reason, for hybrid rockets, a star-shaped grain is not an attractive option to increase the burning area and the volume loading

as it is for solid ones. Usually, hybrid combustion chambers tend to be slender. Often it is stated that this is related to the low regression rate and should not be a problem for low-thrust/long-duration applications. However, this is not completely correct. Considering a classical design (single or multiport), even with complete freedom on the regression rate it is difficult to design a performing system exceeding a certain ratio between the initial and final oxidizer flux (amount of O/F shift, max flux limited by flooding or exit Mach number, lower flux limited by chuffing etc.). This in turn fixes the ratio between the internal and external port diameter and consequently the required regression rate and L/D ratio (for a given motor O/F). Very fat hybrid motors are not likely possible for low-thrust/long burning time systems. An exception could be other alternative configurations like the vortex pancake which however bring its own issues. Another important aspect compared to liquid rockets is that it is not possible to design a propulsion unit that can be used on different spacecraft with different total impulse requirements because, again, the combustion chamber contains the solid fuel. On the contrary, a liquid motor can be combined with different tanks to deliver different total impulses;

- *Combustion efficiency:* As previously said, a hybrid system tends to produce rougher and less complete combustion compared to solid and liquid ones, causing a larger penalty compared to theoretical values;

- *O/F shift:* The impossibility to maintain the motor O/F ratio fixed at the optimal value leads to a decrease of the average specific impulse. Careful design can reduce these losses to less than 1

- *Slower transients:* Ignition transients are generally slower for hybrid systems. The response to throttling is slower too. The combustion chamber of a hybrid is much bigger than an equivalent liquid because it must contain the solid fuels, moreover, the chamber volume changes with time reaching its maximum value at the end of burning when the grain is consumed. Also, the thermal lag in the solid fuel changes with time and reaches its maximum towards the end. This prevents hybrid systems to be used when a very accurate, repeatable, fast response is

necessary (in which case hypergolic liquid mono-bipropellant operating in multi-pulse mode is preferred), but in general, it should be no major issue.

Even with all their advantages, the hybrid systems are still less attractive than solid and liquid if only a few performance parameters must be maximized for a specific task. This is one of the main reason which brought the hybrid to be discarded during the early development of rocket science. Another main reason is their low regression rate. Moreover, the complex coupling between the different motor parameters makes hybrids less attractive from an ideal design point of view.

Another fundamental aspect to underline is how some of the claimed main advantages of hybrid propulsion cannot be reached due to problems related to the propellant choice or to the system configurations(this can be partially be incorporated with the other two propulsion types even to a less extent). Typical examples are the *LEX Sounding Rocket* and the *Firebolt*, which are presented later. One more aspect to highlight is how some of the solutions suggested so far to solve some of the disadvantages prevented the achieving of some of the main advantages. An example of this trade-off is the use of a small amount of oxidizer in the composition of the grain fuel to increment the regression rate. However, even if the grain is safer than traditional solid fuel, it loses the complete inertness which gives the hybrid system its fundamental safety attribute.

Most of the comparison between hybrids and the other propulsive systems are ill-posed. For example, the ablative cooling system of hybrids is simpler than a regenerative cooling for liquids. This comparison has a wrong point of view because it does not consider that even liquids can have an ablative cooling system and hybrids could have a regenerative cooling system. The same kind of comparison could be posed for other subsystems, like the pressurization ones.

In the description of hybrid engines some of their characteristics, as safety and simplicity, could lead indirectly to performance advantages. For example, a safer and simpler propulsion system has more chances to exploit the advantages of air launch. Considering their low cost, these systems can be tested multiple times in a smaller time-frame. This allows for continu-

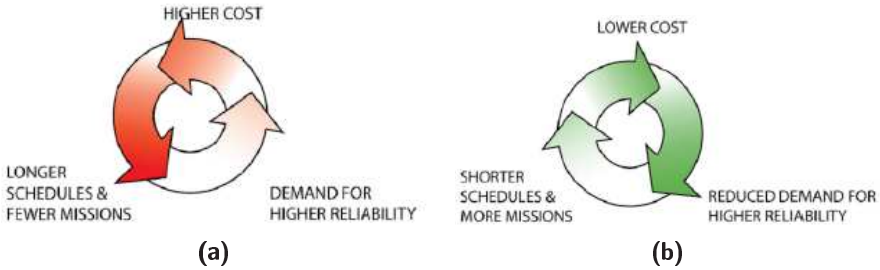

Figure 1.4. *Space Spiral, how it is now,* **a***, and how it should be,* **b** *[29].*

ously upgrading, optimize and improve the systems with new state of the art technology like, for example, new materials. Moreover, a bigger number of tests can lead to important innovation even during times of low investments like the current one.

Analysing the technologies used nowadays on the launchers and spacecraft it is evident how they aren't the real state of the art of the same technologies. The reason lies in the high costs of space and the impossibility, or almost so, to repair failures. Thus, the technologies must be highly reliable. In the choice between an old but highly reliable or new but no so tested technology, the choice often falls on the former. High reliability drives up the costs, and higher costs increase the demand for high reliability. Thus the phenomenon known as space spiral is created [29]. In figure 1.4 there is a representation of how the space spiral is and how it should be. A typical example of the choice of old technology instead of new ones is the fact that a common *PC* has more capability than the computers used in the *ISS*. Any improvement needs to be tested over and over before being actually introduced in real use. This behaviour has prevented for decades a real birth of a large private autonomous space business concentrating most activities on a limited number of government funded projects. In the last years, more and more private companies forced themselves on the market, bringing new life to the space sector.

Nowadays without governmental supports and funding, the space sector would have many difficulties and it could collapse. A drastic reduction in the cost is necessary to allow the space-spiral to reverse and allow considerable developments and innovations. A decrease in the space costs, paired with more flexible systems, could bring lower reliability requirements which,

in turn, could bring a further decrease in the costs which could bring an expansion in the number of missions. An increased number of missions could create the ground for a real sustainable business. Hybrid propulsion could be one of the key features to achieve this objective. However, this could happen only if hybrid engines can grant a significant cost reduction and not only reaching the same level as solid and liquid engines. Considering the exponential in the Tsiolkovsy formulas, only a limited loss of performance is allowed. With bigger losses, the costs indirectly rise and the dimensions must increase. To achieve all these ambitious objectives the classic issues of hybrid propulsion must be resolved, the advantages inherent to this type of propulsion, like safety and simplicity, must be maintained, yet granting high reliability and very low cost [12].

1.3 Hybrid Rocket History

The first developments of hybrid propulsion date back in the '30s, decade in which the foundations of modern rocketry were laid [1]. The first hybrid rocket, even if sometimes is considered a liquid one, is the *Grid09*, launched in 1933 and developed by soviet scientists. One of them was Korolev, which later participated to the creation of the Soyuz program. The *Grid09* worked with liquid oxygen fed by its own pressure and gelled gasoline supported on a metal mesh, its combustion chamber and the entire rocket are shown in figures .

After the liquid oxygen of the *Grid09* the experiments focused on the carbon as a fuel. Carbon has a very low regression rate due to its heat of ablation and was soon abandoned as fuel. In the '40s and '50s, the Pacific rocket Society, General Electric and Jet Propulsion Laboratory kept investigating hybrid propulsion. These first experiments underlined the principal characteristics of these engines, like the low regression rate, the crack insensitivity, the dependence of the regression rate on the oxidizer flow and, thus, the possibility to regulate the thrust varying the oxidizer mass flow.

In the '60s, thanks to the Sputnik success and the Moon race, huge investments and great achievements characterized rocket propulsion. Even if to a lesser degree than solid and liquid, hybrid propulsion took advantage of

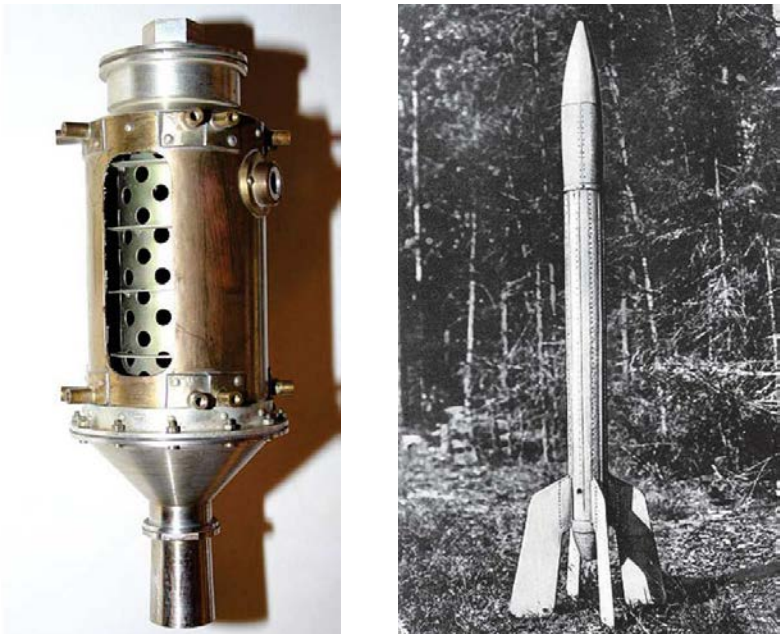

(a) (b)

Figure 1.5. *Grid09 combustion chamber and complete rocket.*

these investments. New fuels and oxidizers were tested defining the foundation of hybrid engine behaviour. One of the major outcomes of this decade is the following formula which correlates well with the regression rate

$$\dot{r} = aG_0^n L^m \tag{1.1}$$

where:

- G_0 is the oxidizer flux;
- L is the length of the combustion chamber;
- a,m and n are coefficients determined empirically.

With this equation, a wide number of studies on possible designs were possible and equations were developed to determine the stoichiometric length and to predict thrust and O/F shift with time.

During the same decade, UTC and Beech Aircraft started to work on Sandpiper and later on HAST - High Altitude Supersonic Target. Later

Figure 1.6. *FireBolt Drone.*

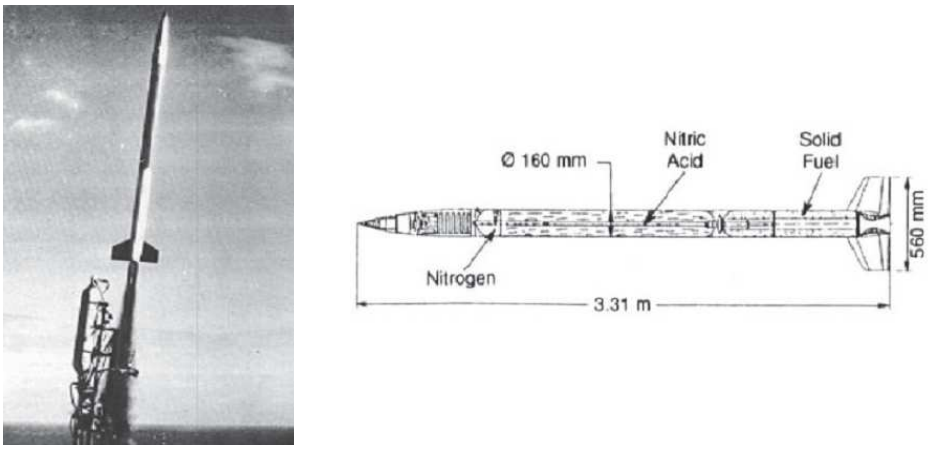

(a) **(b)**

Figure 1.7. *LEX sounding rocket during launch,* ***a****, and its schematic,****b****.*

these programs became the *FireBolt* Target Missile System produced by Teledyne Ryan Aircraft. The *FireBolt* is shown in figure 1.6

In Europe two major activities culminated in the successful ground and flight tests of hybrid sounding rockets. One was realized in France by ONERA, the Lithergol EXperimental - LEX [2]. In Sweden, Flygmotor developed two new fuels, the Tagaform and the Sagaform, and launched two large sounding rocket. It is important to underline how the LEX still remains one of the better performing hybrid rocket ever developed, achieving a very high combustion efficiency. The LEX sounding rocket and its schematic are reported in figure 1.7.

LEX and *Firebolt* programs were not abandoned due to poor perfor-

mance, which were, in fact, excellent, but because the costs and complexities were too high. This is in contrast with the common view of hybrid engines, which sees them as cheap and poor performing.

Hybrid propulsion saw a renewed interest in the '80s. The growth of a commercial satellite market and the international competition drove for low-cost space access. the company *Starstuck* was created to develop a large sounding rocket. After a failed launch, the company was reorganized e renamed AMROC - AMerica ROcket Company, which started to work on a low-cost launcher, the AQUILA [14]. The basic philosophy was to use high design margins to reduce development and production costs and to increase the reliability of the system. Thus, the hybrid propellants were ideally suited for the task. AMROC fired the largest hybrid engine ever tested up to that moment. They relied on a multiport configuration to obtain the necessary burning area and had to solve different problems related to the stability of the combustion. This work laid the foundations for the modern knowledge of large hybrid systems. An attempted launch of a large rocket called SET-1 turned into a failure, but showed some of the peculiar attributes of hybrid systems: in fact, the damages of two different accidents were very limited, showing the intrinsic safety and non-explosiveness characteristics even on large scale. Hybrid systems were considered compelling since they granted a large tolerance in the manufacturing of the grain, they had benign failure modes and the motor could be stopped during flight.

In the '90s the research on hybrid systems had new attention since the end of the Cold War shifted the driving performance parameters of rocket science. The pure performance were abandoned promoting safety, low costs and environmental friendliness. New and old ideas thrived and were tested in order to increment the low regression rate, which was seen as one of the major stoppers of this kind of propulsion. One of the solutions of major success proposed at the time was the swirl or vortex injection. In this configuration, the injection of the oxidizer is tangential to the chamber walls and so it creates a rotating flow field. The strong swirling flow inside the combustion chamber has numerous consequences that can enhance an increment in the efficiency and an improvement of the regression rate velocity.

Yuasa experimented the swirl injection wherein the oxidizer entered the combustion chamber at the head end as in conventional hybrids [35]. At

ORBITEC - ORBital TEchnologies Corporation - Knuth experimented a double vortex where the swirl oxidizer was at the aft end of the grain fuel, opposite to the Yuasa configuration. Knuth design generated a pair of coaxial, co-rotating, bidirectional vortices reaching a high combustion efficiency and an impressive regression rate, more than 7 times the classical values of hybrid systems [16]. At the end of the '90s, the Vortex Flow Pancake - VFP - was developed by Surrey. In this configuration, the swirling oxidizer flow was generated between two disks of fuel which burned in opposite direction. The combustion was very smooth and a high-efficiency value was reached.

More recently Nammo Raufoss used the vortex injection at the head end on a $H_2O_2 - HTPB$ hybrid motor [22]. This solution has the advantage to allow a catalytic decomposition prior to the combustion chamber. Most of the studies on the vortex injection see the oxidizer in gaseous phase, mainly GOX. Nevertheless, in most real systems the oxidizer must be stored as liquid due to performance reasons. Liquid vortex injection was given less attention and the works on it are less impressive than those with gaseous injection. To avoid the liquid injection, it is possible to gasify the oxidizer before it enters the combustion chamber, although this adds complexity to the system. In this way, the full potential of gaseous vortex injection can be exploited on an operation motor. Nammo configuration resulted in a motor that is stable, throttleable, with a good efficiency and with a regression rate several times higher than a classical hybrid. Moreover, the hot products of H_2O_2 decomposition are able to ignite the solid fuel. In this way, the motor can be started and stopped several times without the need for a separate ignition device.

In 1999 Lockheed Martin started the HYSR program - HYbrid Sounding Rocket Program [3]. The goal was to develop and launch a large hybrid sounding rocket, showing the advancing readiness level and the positive attributes of these systems. The three-year technology demonstration program was a partnership between Lockheed Martin and NASA with a 6 million budget. During the program, Lockheed Martin developed and tested two hybrid sub-systems. The first was a small hybrid rocket with gaseous oxygen (GOX) to ignite the main engine and maintain stable the combustion. The second relates to the pressurization technique: to meet the budget and the time constraint, a pressure-fed solution was chosen but a special

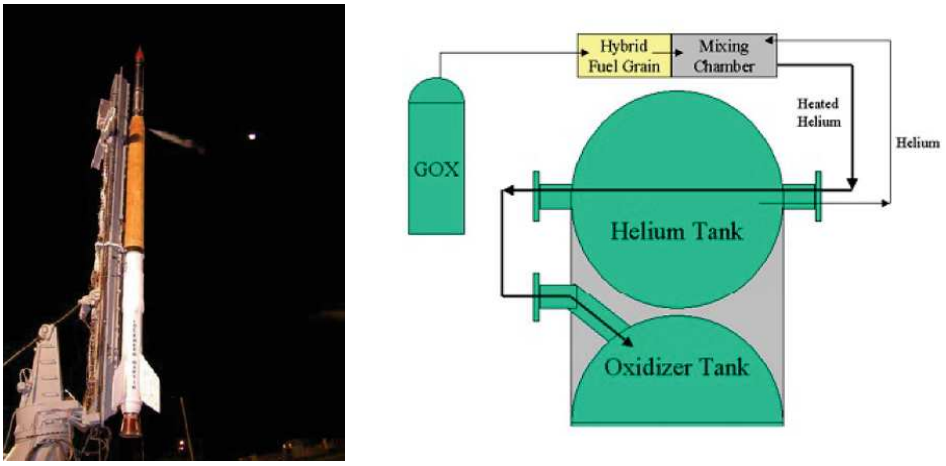

Figure 1.8. *HYSR sounding rocket at launch,* ***a****, and LM patented heated helium pressurisation system,* ***b****.*

upgrade was conceived to limit the volume and weight of the entire pressurization system. The HYSR was launched from Wallops in December 2002 reaching an altitude of 42 kilometres.

Based on the previous experience, LM participated to the DARPA Falcon Small Launch Vehicle - SLV - program to develop and demonstrate an affordable and responsive space lift capability. LM tested a 3 rows 43 ports upper stage motor in 2005 [13]. The rocket schematic and motor before and after the test are shown in figure 1.9.

Finally, other five projects are considered worthy to be cited and described: SpaceShipOne by Scaled Composites, Atea 1 by Rocket Lab, Stratos by Dare - TU Delft, Heroes by HyEnD - University of Stuttgart and Nucleus by Nammo.

1.3.1 SpaceShipOne - Scaled Composites

The greatest success of hybrid propulsion is certainly the Space Ship One - SS1 - of Burt Rutan's Scaled Composite which won the Ansari X Prize. The Ansari X Prize was a contest for the first commercial agency able to fly twice over 100 km. Scaled Composites built a two-stage airplane, whose first stage was an air-breathing plane called White Knight and was used as a carrier for the second stage, the before-mentioned SS1. SpaceShipOne

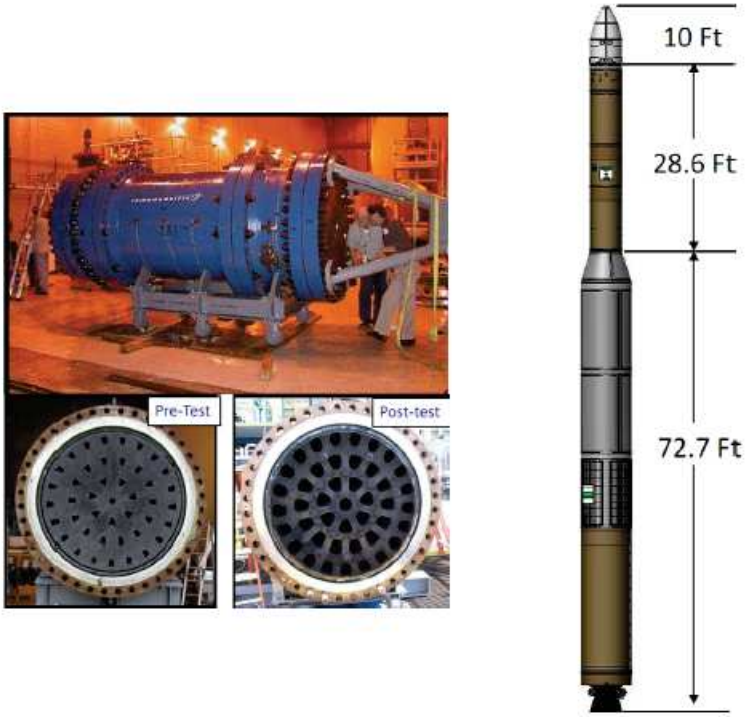

Figure 1.9. *Falcon hybrid rocket, Lockheed Martin - DARPA [36].*

had a $N_2O - HTPB$ hybrid engine. To win the Ansari X prize, Scaled Composite elaborated multiple unique and innovative solutions. SS1 was completely designed around the hybrid engine and oxidizer tank, which was bonded to the inner airframe structure. The tank had a metallic internal liner with composite fiber overwrap. In 2004 SpaceShipOne flew above $100\,km$ winning the X Prize. Thanks to this victory, hybrid propulsion became known outside the restricted area of propulsion engineers.

The Scaled Composite choice of a hybrid system confirmed some of its positive attributes, as safety, good performance, low system costs, quick turnaround and the possibility to stop the thrust. SS1 showed the success of hybrid system implementation, mainly in the use of composites material, self pressurization and integrated design [26].

Scaled Composites together with Sierra Nevada Corporation - SNC - is developing and testing the successor of SS1, the SpaceShipTwo. As for SS1, the SS2 uses an air-breathing plane as first stage carrier, the White Knight Two. SpaceShipTwo will be bigger than SS1 and the projects see two pilots

Figure 1.10. *SpaceShipOne and White Knight carrier.*

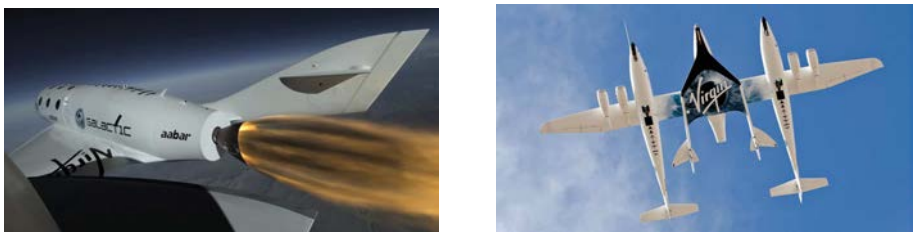

Figure 1.11. *SpaceShipTwo and White Knight Two carrier.*

and a passenger deck, with up to six passengers. Virgin Galactic planes to use SS2 for suborbital flights for paying tourists.

SpaceShipOne is now in Washingotn D.C at the Smithsonian Institute's National Air and Space Museum.

1.3.2 Atea 1 - Rocket Lab

In 2009 the New Zealand company Rocket Lab successfully launched the Atea-1 sounding rocket. With its successful launch from the Great Mercury Island in New Zealand, Rocket Lab became the first private company in the Southern Hemisphere to reach space.

The Atea-1 is a two-stage rocket with a first stage hybrid booster and a second stage inert dart. It has a diameter of $0.15\,m$ and a length of $6\,m$. The flight structures, pressure vessels and the combustion chamber are crafted with composite materials. The inert, dry mass of the vehicle is less than $20\,kg$ with a lift-off mass of $60\,kg$. The peak thrust is $6.7\,kN$.

In the projects the Atea-1 should have burned for around 20 seconds, reaching Mach 5 and an altitude of more than 100 km. However, unfortunately, the second stage was never recovered and so the real performance and achievements were never assessed. Nevertheless, it is a demonstration of how the correct use of composite materials on sounding rocket could allow good propellant mass fraction for hybrid sounding rocket.

1.3.3 Stratos - Dare - TU Delft

Stratos I was launched from Kiruna, Sweden, in 2009 reaching an altitude of $12.3\,km$ and setting the European altitude record for student rocketry at the time. It was a two-stage, solid-propellant rocket. The first stage had

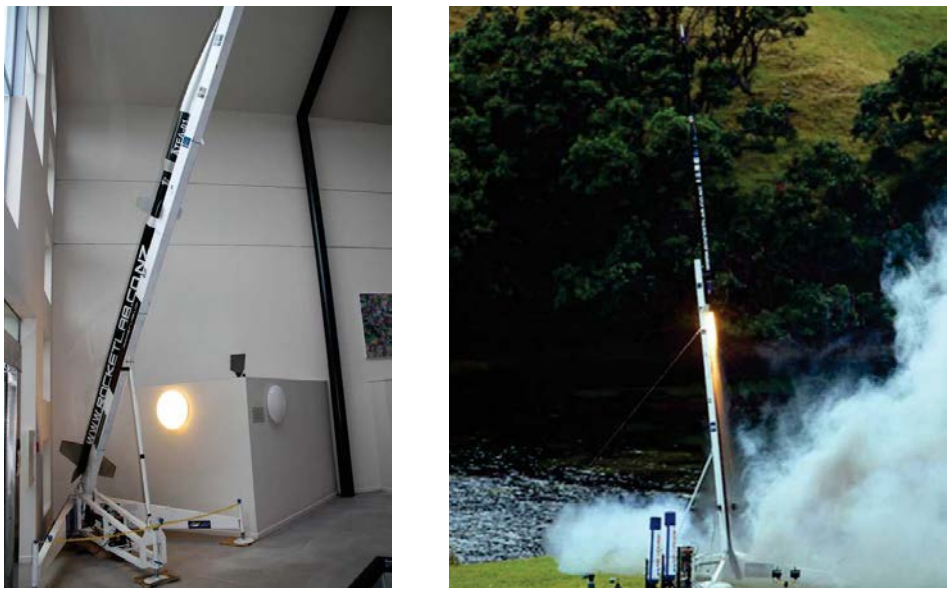

Figure 1.12. *Atea-1 sounding rocket.*

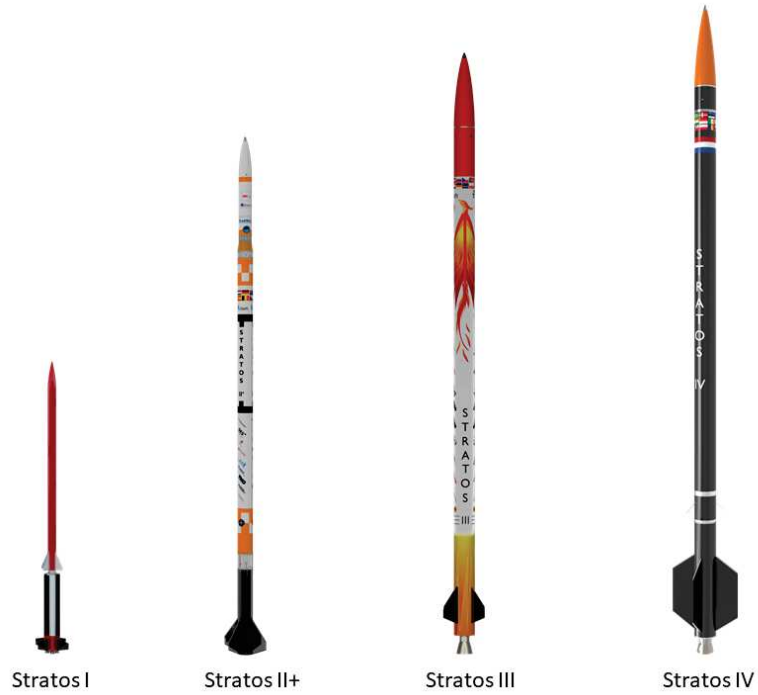

Figure 1.13. *Representation of the Stratos rockets.*

four booster motors, each one capable of developing a $1.5\,kN$ thrust. The projects did not see the recovery of the entire rocket but only of the top section of the rocket with the electronics and experimental payloads. Unfortunately, the separation did not and, thus, the parachute never deployed. The rocket hit the ground at high speed and no data could be extracted from the electronics module also due to the months between the crash and the rocket recovery.

After Stratos I, DARE designed Stratos II. In 2014 there was an attempted launch, but a misfire prevented the engine to fire up. The misfire was due to a leak in the oxidizer feed system[15]. They failed launch of Stratos II brought a redesign of some of the rocket components, a the new rocket was called Stratos II+. Stratos II+ had a length of $6.9\,m$ and was powered by a single stage hybrid rocket engine. The engine used nitrous oxide as oxidizer and as fuel a mixture of paraffin and aluminium powder. The engine could develop a $180\,kNs$ total impulse and a burn time of 23 seconds. The recovery system consisted of two parachutes, a small drogue parachute and the main parachute, which had to slow down the rocket. Stratos II+ was launch from El Arenosillo in Spain on the 16^{th} of October 2015. It reached an altitude of $21.5\,km$ breaking the European record set by Stratos I.

The new European altitude record was then broken in 2016 by the Heros 3 hybrid rocket, by the Hybrid Engine Development from Stuttgart University. Stratos III was designed to improve the European altitude recorded. The engine had an average thrust of $15\,kN$ and a burn time of 28 seconds. The Stratos III was launched on the 26^{th} of July 2018. After 20 seconds of flight, the rocket disintegrated at an altitude of approximately $10\,km$ [34].

Dare is now working on the development of Stratos IV. Stratos IV has a total length of around $8.3\,m$ and a diameter of $27.8\,cm$. Its engine should develop an average thrust of $10\,kN$. The rocket should be launched from South-Africa in the summer of 2021 and in the projects it should reach an altitude of more than $100\,km$.

1.3.4 Heros - HyEnD - University of Stuttgart

Heros sounding rockets have been developed by HyEnD, Hybrid Engine Development, a student-based project at the University of Stuttgart. HyEnD was founded in 2006 and in the following years it focused on the development of its own hybrid engine. In 2012 they applied for the project Studentische Experientalraketen (student experimental rockets) STERN of the German Aerospace Centre(DLR). In the three-year project, HyEnD developed and built its experimental rocket.

Heros rockets used paraffin as solid fuel and nitrous oxide, N_2, as liquid oxidizer. This choice allows for relative safe handling. The motor had a thrust of more than 10 kN. Heros rockets were launched from ESRANGE, close to Kiruna in Sweden. This site is used for the launch of many European sounding rockets [18].

In October 2015 Heros 1 was launched. Shortly after launch, the rocket was damaged. After the recovery of the rocket, the examination pointed to a structural failure. In particular, some instabilities in the combustion chamber caused by low temperature N_2 caused a motor case burn-through.

One year later, Heros 2 and Heros 3 were launched. Heros 2 was launched on the 31^{st} of October 2016. A failure of the on-board electronics and telemetry prevented the recording of any positional data during or after the flight. A search of the nominal impact area did not reveal the rocket position[24].

Heros 3 was launched on the 8^{th} November 2016. The rocket was 7.5 m long and had a dry mass of only 75 kg. The low dry mass was mainly due to the use of carbon fibre for the rocket structure. During its flight, it reached a maximum velocity of $720\,m/s$ which corresponds to Mach=2.3. The Heros 3 rocket is shown in figure 1.14.

With the launch of Heros 3 a new altitude record was set for European student and amateur rocketry and for world hybrid rocket built by student. The record is 32.3 km. This record shows the potential of the rocket hybrid propulsion and in particular of the hybrid sounding rocket [17].

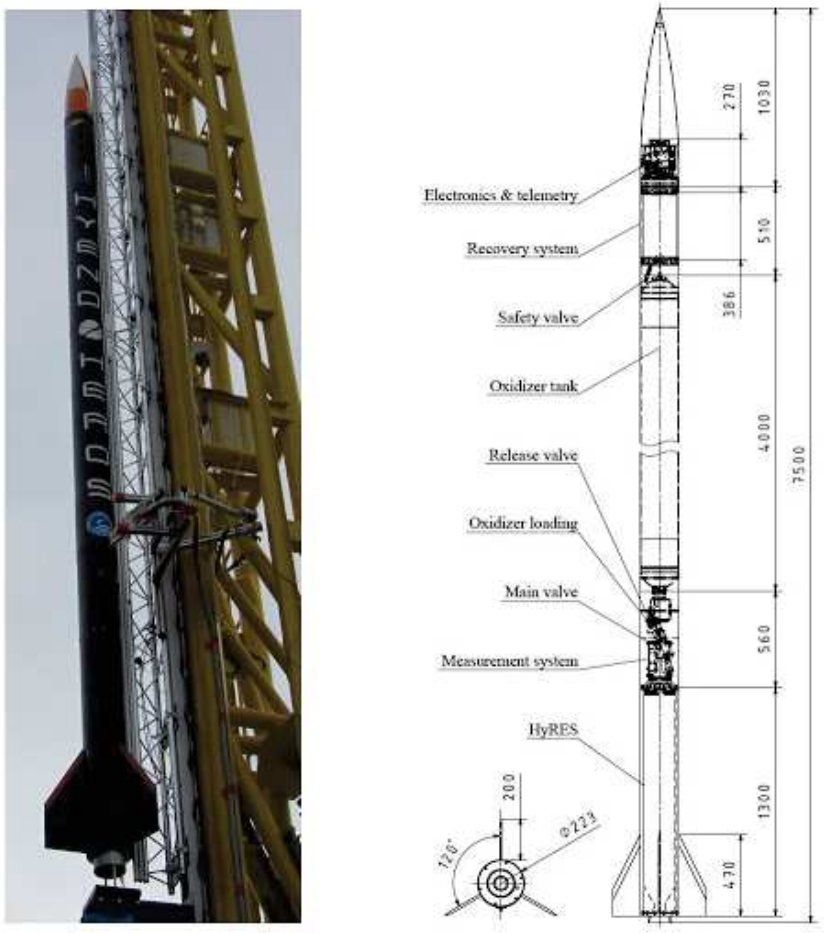

Figure 1.14. *Heros III rocket and schematic [17].*

Figure 1.15. *Nucleus sounding rocket.*

1.3.5 Nucleus - Nammo

In September 2018 Nammo launched Nucleus, a hybrid sounding rocket, from Andøya Space Centre in Northern Norway. Nucleus reached an altitude of $107\,km$ and was the first rocket powered by a Norwegian motor design to reach space and the first European rocket to do so in more than 50 years. Nucleus is a single-stage spin-stabilized rocket powered by a $30\,kN$ hybrid motor[9].

Nucleus was developed inside the Future Launcher Preparatory Program - FLPP - contract with ESA as a step on the demonstration of the feasibility of hybrid propulsion for sounding rocket and micro-launcher.

Nammo hybrid technology uses a combination of H_2O_2 and HTPB. This combination enhances the intrinsic characteristics of safety and simplicity of hybrid systems with respect to liquid and solid, making this technology very attractive for applications were the driving parameters all low costs, environmental friendliness and good performance[10].

The oxidizer is stored as a liquid. However, before being injected in the combustion chamber it runs through a catalytic and decomposes reaching temperature above $600\,°C$. Thus, the injections in the combustion chamber is of a hot gas and this allows the combustion to start without the need of any igniter due to the high temperature which vaporizes the solid fuel. The vortex flow field generated during the injections of the oxidizers allows to maintain a high heat flux towards the grain surface and so the combustion

is stable due to an appropriate mixing of oxidizer and fuel[8].

The successful launch of Nucleus and the good performance during the entire flight showed the performance of the entire hybrid system and the maturity level reached by this technology. Nucleus is now flight-qualified and can be used for experiments and researches. Different altitudes can be reached thanks to the possibility to change the filling level of the oxidizer, even at launch day if necessary.

Nammo is working on Aurora, a sounding rocket that could be able to reach a 350 km altitude, allowing experiments and researches on the high atmosphere and microgravity conditions. Proceeding on the FLPP, Nammo is up-scaling its motor from $30\,kN$ to $100\,kN$ and it could be used as first or second-stage engine for hybrid micro-launcher. Thrust is not the only aspect that needs improvement in order to achieve the characteristics of a micro-launcher. The dry mass needs to be reduced and the use of a motor case in carbon could reduce the mass and the manufacturing costs.

CHAPTER 2

Sounding Rocket Design

The sounding rocket has been designed by a team of students and employees of *T4i-Technology for Propulsion and Innovation*, a spin-off company of the University of Padua. It is propelled by a hybrid system with liquid hydrogen peroxide and a solid grain of paraffin respectively as oxidizer and fuel. *T4i*, during its various activities, has already designed, built and tested similar motors. The main goals of this project are to further develop the motor and the connected technology and then to validate the hybrid technology developed. After a first launch, the system should be further improved to reach higher and better performance, both in the motor thrust and in the altitude reached. The sounding rocket is expected to launch in 2021 and reach an altitude of more than 10 km.

It is worth to underline how many figures and descriptions in this chapter refer to older versions of the project. They are here reported only for explanatory purposes and do not necessarily represent the final design. Moreover, the project is still in development, therefore many parts could undergo revisions and changes.

2.1 General Requirements

The general functional requirements of the sounding rocket are:

- *Thrust*: 5 kN;
- *Burning time*: 30 s;

- H_2O_2 decomposed in a catalytic reactor and then injected into a single port, cylindrical grain of paraffin. Hot, decomposed gas must start the ignition, no igniter is required;
- Pressure - fed pressurization system using N_2 as pressurizer;
- External body made of carbon fiber reinforced epoxy composite;
- Oxidizer tank integrated with the external cylindrical body and without liner;
- Total length not exceeding 6 m and a diameter not exceeding 0.2 m;
- Recovery system with parachutes and inflatable float to retrieve the entire rocket after the mission.

2.2 General Overview

The design of the sounding rocket can be divided into 5 main topics, each one representing a different sub-system:

- *Structures*: which include the external cylindrical case, the nosecone, the junctions, the fins and all components assembly;
- *Recovery System*: which includes the parachutes, the floats and the controls and actuators;
- *Fluidic System*: which includes the pressurized N_2 cylinder, the oxidizer tank and the feeding pipes and valves;
- *Motor*: which includes the catalytic reactor, the grain, the nozzle and the thermal protection;
- *Payload*: which includes the avionic and telemetry, the diagnostics and the controls.

Only the first 4 sub-systems will be described in the following paragraphs. The payload, with all of its components, was not developed as part of the student project and, thus, is not described.

In figure 2.1 there is a CAD representation of the Sounding Rocket and its different parts.

(a) CAD representation

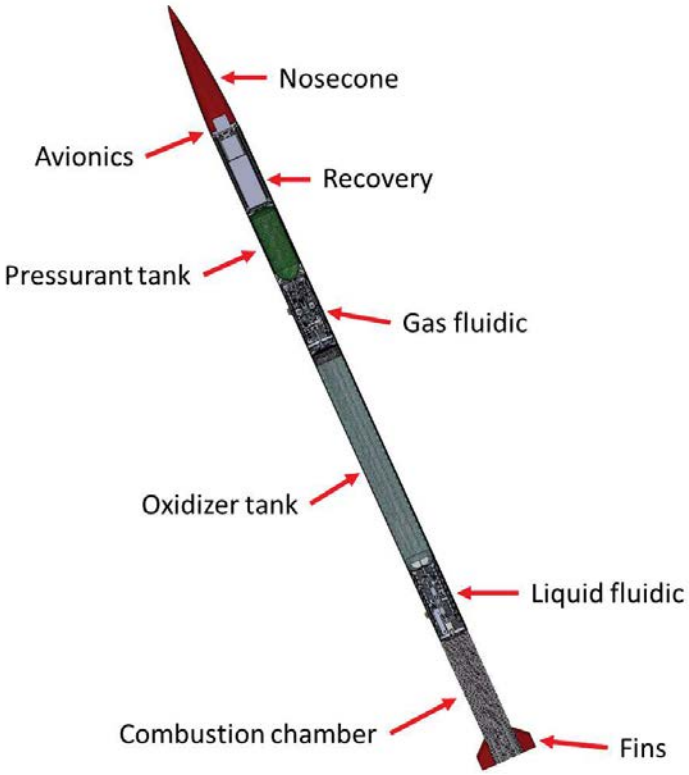

(b) Sub-systems position

Figure 2.1. *Sounding Rocket CAD representation and sub-systems position.*

2.3 Structures

The Structure sub-system is not completely independent from the other. The nosecone is part of the recovery, the interstages enclose the fluidic line and the fins are connected with the motor outer case. The structure design is developed on aerodynamic and trajectory studies. The description of the structures of the sounding rocket focuses on four main parts:

- *Nosecone*;
- *Junctions*;
- *Fins*;
- *Interstages*.

The structural description of the sounding rocket is helpful to give a general idea of the rocket layout.

2.3.1 Nosecone

The nosecone has a Von Karman profile to reduce the drag acting on the rocket during flight. The choice of the profile depends on the maximum Mach number which should be reached during flight. Von Karman's profiles are built using the mathematical equations reported below

$$\theta = \arccos\left(1 - \frac{2\,x}{l}\right)$$
$$y = \frac{r}{\sqrt{\pi}}\sqrt{\theta - \frac{\sin(2\theta)}{2}} \tag{2.1}$$

where:

- r: is the final radius, $r = 99.1\ mm$;
- l: is the total length, $l = 930\ mm$;
- x: is the distance from the nosecone tip;
- y: is the local diameter along the distance from the nosecone tip.

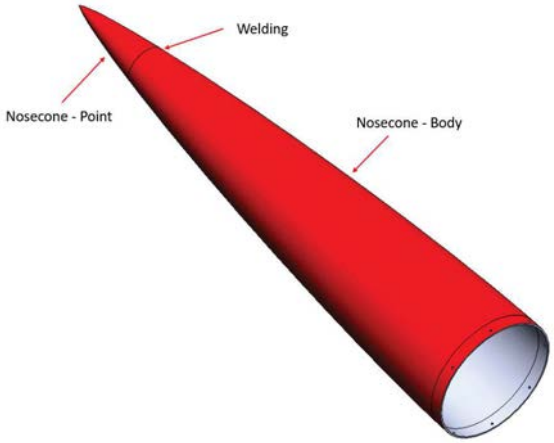

(a) CAD rendering

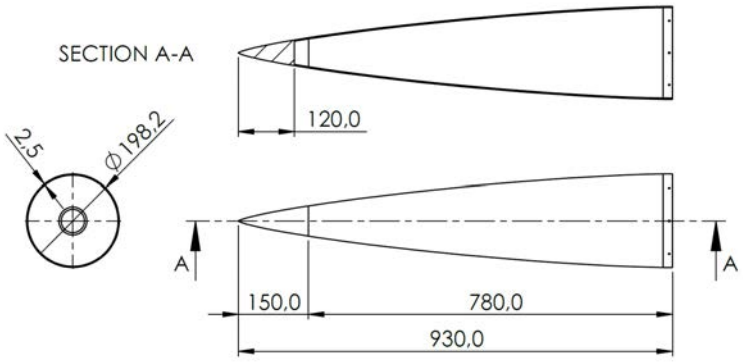

(b) Dimensions

Figure 2.2. *Nosecone CAD rendering and general dimensions.*

The nosecone will be manufactured using aluminium alloy to ensure good strength against the heigh temperature that could be reached during the flight due to the drag. The temperature on the tip of the nosecone could reach $300°C$ while on the body it should not exceed $200°C$. In figure 2.2 are reported a CAD representation of the nosecone and its general dimensions. To grant the preservation of the aerodynamic characteristics during the entire flight, the tip must not change its geometrical characteristics. Thus, the nosecone tip is not empty and so it ensures a better strength against high temperatures.

2.3.2 Junctions

The sounding rocket is not a unified structure but is composed of different segments connected together with metallic junctions. These junctions simplify the handling and assembly of the rocket. The junctions are:

- *Junction 1*: between the core engine and the liquid line structure;
- *Junction 2*: between the tank and the gas line structure;
- *Junction 3*: between the gas line structure and the recovery bay;
- *Junction 4*: between the recovery bay and the nosecone.

The junctions are made in ergal and they are bonded to the main structure with adhesive. The junctions are divided into two parts, each one connected to a different part of the rocket and are held together by screws. The junctions position and the CAD representation of one of them are shown in figure 2.3. The junctions differ from one another due to specific characteristics or requirements, but the overall structure is the same.

2.3.3 Fins

The rocket has four trapezoidal fins arranged symmetrically around the nozzle-end of the rocket. The fins have a flat profile with wedges. The choice of the aerodynamic profile is a trade-off between drag and robustness. Other profiles, like the diamond profile, have a lower drag coefficient. However, the diamond profile is not as robust as the one chosen and suffers more of problems like the flutter.

The fin thickness is 6 mm. The root chord is 216 mm while at the tip is 108 mm with a span of 171 mm. The sweepback angle of the trailing edge is 0° while at the leading edge is about 57°.

The wings can reach a temperature of 200° C and since they are fundamental for the rocket stability, they have to maintain perfectly their aerodynamic characteristic throughout the entire flight. Thus, they are manufactured in ergal. The fins are connected with the main structure via two appendices on the aluminium rocket end and with screws with collars. The fins are connected in this way to guarantee a high accuracy of alignment. The fins general design is shown in figure 2.4.

(a) Junctions position in the rocket

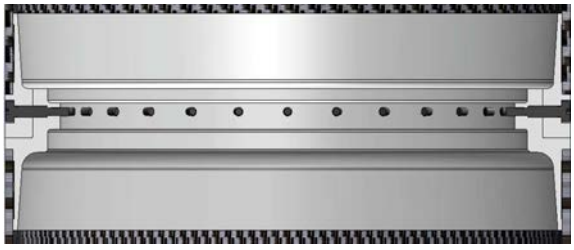

(b) Junction general schematic

Figure 2.3. *Junctions position in the rocket and general schematic.*

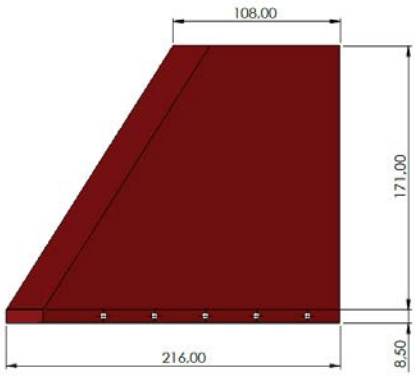

(a) General dimensions

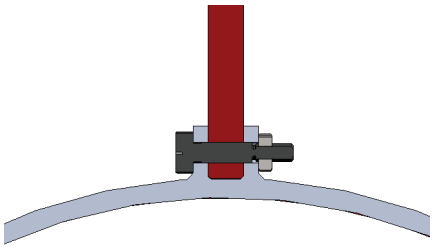

(b) Connection with the main structure

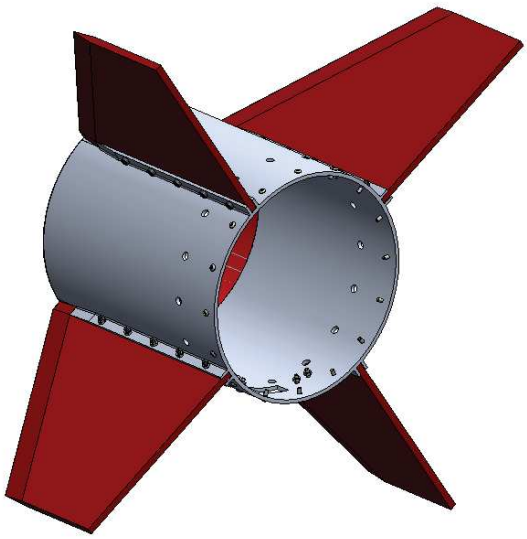

(c) Design

Figure 2.4. *Fins general design.*

2.3.4 Interstages

The main structure can be divided in different sub-parts, or interstages, which are:

- *Liquid Interstage*;
- *Gas Interstage*;
- *Recovery Interstage*.

The different parts are connected together with the use of metallic junctions.

The liquid interstage extends from the main engine to the gas line, including the liquid line and the tank. The external cylindrical case, with the addition of two end-cups adhesively bonded to it, acts as oxidizer tank.

The gas interstage extends from the upper end-cup of the oxidizer tank to the recovery interstage, including the gas line and the pressurized N_2 gas cylinder.

Due to the complexity of the fluidic lines, both liquid and gas, and to the necessity to have access to them prior to launch, some openings are created in the main structure. All openings will be closed with hatches during flight. The openings in the fluidic line are four, two located on the gas line between the pressurized N_2 gas cylinder and the oxidizer tank, and two on the liquid line, between the tank and the main engine. These openings are 90° wide and, thus, only half of the structure will remain intact and carry the loads. Since the presence of the openings distorts the stress distribution on the structure, several reinforcements have been positioned in correspondence of the openings. These reinforcements stiffen the structure and allow the connection of the hatches. A reinforcement is present also on the hatches to allow the connection. The reinforcements are made in ergal and are connected to the main structure and hatches through adhesive bonding. In figure 2.5 are shown the internal reinforcements of the main structure and the lateral hatch which closes the opening.

The recovery interstage extends from the gas interstage to the nosecone. An opening similar to the openings in the fluidic line is present in the recovery bay to allow the ejection of the parachute. The opening in the recovery interstage is larger than on the fluidic lines due to the parachutes and floats ejection. The opening during flight will be closed by a panel.

Figure 2.5. *Internal reinforcements adhesively bonded to the main structure and lateral hatch.*

2.4 Recovery System

The recovery system should gradually reduce the rocket velocity allowing a gentle sea land. Thus, the rocket should not be damaged on impact and it should be recovered. The recovery will allow a complete analysis of the flight data. The recovery system is placed between the nosecone and the pressurized N_2 gas cylinder. Its position is reported in figure 2.6.

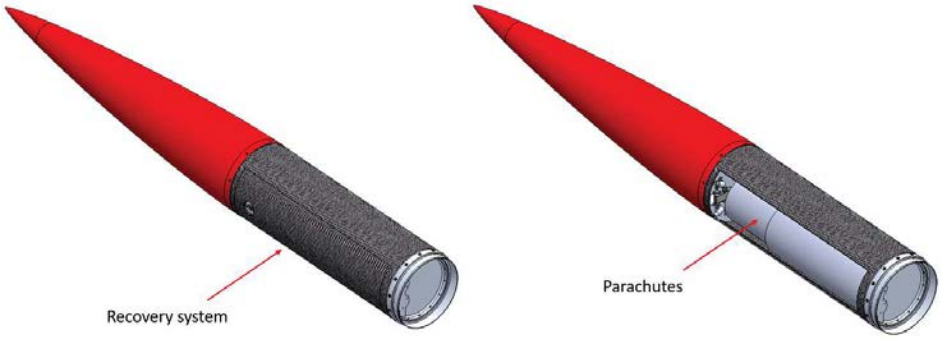

Figure 2.6. *Recovery system.*

To allow the correct recovery of the rocket, three parachutes are installed in different locations along the rocket length and, to avoid the rocket sinking after landing, a floating system is also present.

There are three parachutes (first parachute, drogue parachute and main parachute) which will be opened in sequence after the rocket passage at

apogee. The first parachute will be opened as the recovery door is pushed out with the aid of two springs. The drag will inflate the parachute which in turn will release the drogue parachute. The drogue parachute will then release the main parachute. The system operation can be briefly summarized as follows:

- During the flight the recovery bay is closed;
- After the rocket apogee passage, the recovery bay door is pushed out. The door is connected to the first parachute bag and when the bag is removed, the first parachute inflates due to the drag;
- The first parachute is connected to the recovery plate and to the bag of the drogue parachute. A cypres cutter cuts the shock cord connecting the first parachute to the recovery plate, releasing it and pulling away the bag of the drogue parachute;
- Due to the drag force, the drogue parachute is ejected and inflated;
- The drogue parachute is connected to the recovery bay, to the main parachute bag and to the main parachute itself. A cypres cutter cuts the shock cord connecting the drogue parachute to the recovery plate, the main parachute bag is pulled out;
- The main parachute is inflated due to the drag and slows the rocket till it lands on the water;
- As the rocket touches the water, the floats inflate ensuring the rocket buoyancy till it is recovered.

2.5 Fluidic System

The fluidic system of the rocket extends from the N_2 gas cylinder, just below the recovery bay, to the catalytic bed just above the motor. The feeding line can be divided into two main lines:

- *Gas Line*: between the pressurized N_2 gas cylinder and the oxidizer tank;
- *Liquid Line*: between the oxidizer tank and the main engine.

In addition to the two feeding lines, the fluidic system includes the HTP tank. The oxidizer tank is composed of the main cylindrical structure, which acts as sidewalls, and by two domed-shape end-closure. Both the end-closures and the cylinder are made with carbon-reinforced materials and are bonded together with epoxy adhesive. The domes have a steel insert to allow the connection to the liquid lines.

The Gas Line must ensure the flow of the N_2 from its gas cylinder to the tank to ensure the right pressurization of the HTP. The gas pressurization line consists of:

- Fill and drain valve, to charge and discharge the gas tank;
- Main line with redundant valves, one of which is electro-actuated and the other is manually actuated:
- By-pass line to initially pressurize the oxidizer tank;
- Solenoid valve on top of the oxidizer tank acting as venting device.

The Liquid Line provides a constant HTP flow from the tank to the catalytic. Any problems on the line could create irregularities in the oxidizer flow which in turn could create instabilities and problems in the combustion process. The liquid line consists of:

- Fill and drain valve, to charge and discharge the H_2O_2;
- Burst disk acting as safety passive device, that will break in case of high pressure due to an unexpected oxidizer dissociation;
- Main line with double valves, one actuated with a pneumatic actuator and the other manually actuated;
- Cavitating Venturi channel to regulate the mass flow.

A check valve is present on the line to prevent seawater from entering the oxidizer tank. In this way, the tank will improve the overall buoyancy of the rocket helping to keep it afloat till it is recovered. Along the whole line, temperature and pressure sensors are positioned to keep the evolution of the system under control.

Since the fluidic system regulates the HTP flows and influences directly the combustion, some valves must be inserted to ensure complete safety throughout all operations. Bearing in mind the possible safety concerns, on the fluidic line are inserted:

- *By-pass line*: to avoid overheating during the pressurization phases;
- *Non-reclosing passive relief safety device*: in case of unexpected H_2O_2 dissociation it let the tank pressure drop off without any detection or human intervention;
- *Redundant manual valve*: after the main valve is actuated, this valve allows to operate on the rocket in safety conditions during pre-launch phases.

2.6 Motor

The propulsion system of the rocket consists of a hybrid motor that uses paraffin grain as solid fuel and HTP as liquid oxidizer. The system can be divided into three main components:

- *Catalyst bed*: place right below the first junctions it decomposes the HTP before it enters the combustion chamber;
- *Combustion chamber*: a paraffin cylindrical port grain burns reacting with the decomposed HTP.
- *Nozzle zone*: it accelerates the hot exhaust gases generating the thrust.

The motor case is in carbon fibre reinforced composite material. Thus, it important to protect it from the heat of the combustion. A cylindrical HDPE, High Density PolyEthylene, encloses most of the motor, from the catalytic reactor to the nozzle. Additional HDPE thermal protections are placed at both ends on the grain. The pressure inside the combustion chamber can reach a pressure up to 25 *bar*.

CHAPTER 3

Dynamic Model of the Rocket

The rocket behaviour and its trajectory are simulated using an in-house 6 Degree of Freedom code. For a correct simulation, it is important to have a complete description of the geometrical characteristics and the mass distribution and variations of the rocket. It is then necessary to evaluate the effects of the different forces on the rocket trajectory.

The aerodynamic forces are evaluated with the help of another code that allows for the definition of the lift and drag coefficient in relation to the speed and angle of attack of the rocket.

The rocket trajectory depends mainly on the aerodynamic forces, but there are also other parameters to consider, like the Jet Damping or possible misalignments. The misalignments taken into account are those that concern the thrust vector and the fin attachment to the main structure. The misalignments can create forces and moments on the rocket.

3.1 Rocket Parameter

A correct trajectory simulation implies a correct and exhaustive description of the characteristics of the entire rocket. These can be the external geometric characteristics, like the length or the diameter, the mass and its distribution or variation, or the inertia values. In table 3.1 are listed the main parameters of the sounding rocket.

Parameter	*Value*
Length $[m]$	5.629
External diameter $[m]$	0.1962
L/D $[-]$	28.69
Initial L_{cg} $[m]$	3.327
Final L_{cg} $[m]$	3.045
Initial mass $[kg]$	147.49
Final mass $[kg]$	80.1
Initial I_x $[kg\,m^2]$	0.78
Final I_x $[kg\,m^2]$	0.46
Sea level I_{sp} $[s]$	207.72
Sea level thrust $[N]$	4575.8
Nosecone length $[m]$	0.930
Fin root cord $[m]$	0.216
Fin tip cord $[m]$	0.108
Fin span $[m]$	0.171

Table 3.1. *Sounding rocket general data.*

3.2 Aerodynamic Forces acting on the Rocket

The aerodynamic coefficient and the position of the centre of pressure are determined with respect to the rocket altitude and velocity with another code. The altitude influences the aerodynamic coefficient due to the variations in the atmosphere characteristics. The aerodynamic coefficients of the rocket in relation to the Mach number are shown in figure 3.1 while the position of the centre of pressure is shown in figure 3.2.

The lift and drag coefficient can be determined instant per instant using the flight characteristics, like the Mach number. The lift and drag forces depend on the aerodynamic coefficients, on the velocity, on the air density and on the cross sectional area of the rocket, A_{ref}. It is possible to evaluate the lift and drag forces acting on the rocket

$$F_L = \frac{1}{2}\,\rho\,v^2\,c_l\,A_{ref} \tag{3.1}$$

$$F_D = \frac{1}{2}\,\rho\,v^2\,(c_d \cdot c_{d\_correction})\,A_{ref} \tag{3.2}$$

The drag coefficient in the simulation is increased by a multiplying correc-

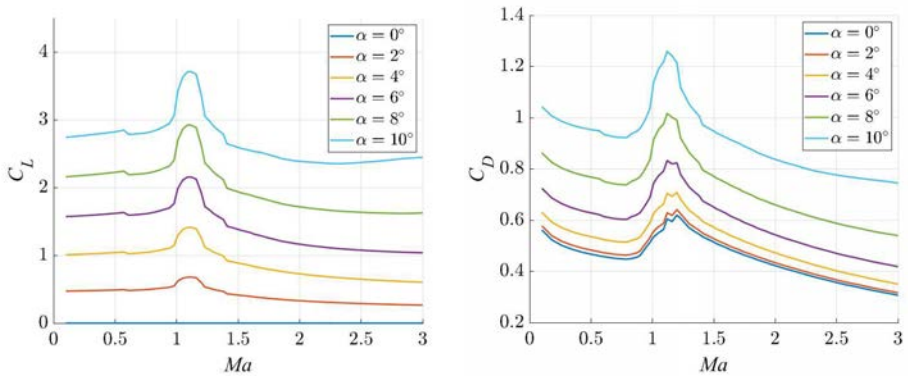

Figure 3.1. *Lift and drag coefficient of the sounding rocket with respect to the Mach velocity.*

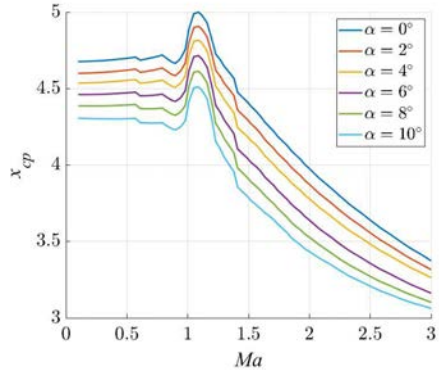

Figure 3.2. *Position of the centre of pressure of the sounding rocket with respect to the Mach velocity.*

tion $c_{d\_correction} = 1.15$. This enables to consider all those sources of added drag, like bolts, junctions or discontinuities in the external geometry, which are not directly taken into account in the drag evaluation of the sounding rocket.

The aerodynamic forces act on the centre of pressure of the rocket. Thus, the moment around the centre of gravity can be expressed as follow

$$\vec{M}_{aer} = \vec{r}_{g-cp} \times (\vec{F}_L + \vec{F}_D) \tag{3.3}$$

where $\vec{r}_{g-cp}$ is the distance between the centre of pressure and the centre

of gravity of the rocket

$$\overrightarrow{r}_{g-cp} = \begin{Bmatrix} (x_{cp} - L_{cg}) \\ y_{cp} \\ z_{cp} \end{Bmatrix} \tag{3.4}$$

where x_{cp} is the position along the rocket axis of the centre of and L_{cg} is the position along the rocket axis of the centre of gravity, both measured from the nosetip. If the centre of pressure is on the rocket axis, then y_{cp} and z_{cp} are both equal to zero.

3.3 Trajectory Equations

Aerodynamic forces and moments influence greatly the trajectory. However, for a complete description of the rocket trajectory, it is necessary to take into account the contributions of other forces and the relative generated moments. The total force and moment acting on the rocket can be evaluated as in equations 3.5.

$$\begin{aligned} \overrightarrow{F}_{tot} &= \overrightarrow{F}_g + \overrightarrow{F}_L + \overrightarrow{F}_D + \overrightarrow{T} + \overrightarrow{F}_{L_{fin}} + \overrightarrow{J_D} \\ \overrightarrow{M}_{tot} &= \overrightarrow{M}_{aer} + \overrightarrow{M}_{thrust} + \overrightarrow{M}_{aer_{fin}} + \overrightarrow{M}_{spin_{fin}} + \overrightarrow{M}_{J_D} \end{aligned} \tag{3.5}$$

where:

- $\overrightarrow{F}_{tot}$ and $\overrightarrow{M}_{tot}$ are the total force and moment acting on the rocket;
- $\overrightarrow{F}_g$ is the Gravity force;
- $\overrightarrow{F}_L$ and $\overrightarrow{F}_D$ are respectively the Lift and Drag force acting on the entire rocket;
- $\overrightarrow{T}$ is the thrust;
- $\overrightarrow{F}_{L_{fin}}$ is the Lift force acting on the fines due to their misalignment;
- $\overrightarrow{J_D}$ is the Jet-Damping force;
- $\overrightarrow{M}_{aer}$ is the moment of the aerodynamic forces;

- $\overrightarrow{M}_{thrust}$ is the moment due to the thrust misalignment;
- $\overrightarrow{M}_{aer_{fin}}$ is the moment due to the fin misalignment;
- $\overrightarrow{M}_{spin_{fin}}$ is the spin moment due do the fin misalignment;
- $\overrightarrow{M}_{J_D}$ is the moment due to the Jet-Damping force.

The aerodynamic forces and moments have already been described. The thrust misalignment, the fin misalignment and the Jet-Damping are analyzed in the following paragraphs.

3.3.1 Thrust Misalignment

The thrust can have a not perfect alignment with the rocket axis. The misalignment can derive from several factors and can be expressed as a not perfect centering of the thrust application point on the rocket axis or as a not perfect parallelism between the thrust vectors and the rocket axis. These misalignments can create loads and moments.

The thrust vector can be represented in relation to a coordinate flame system that is not coincident with the rocket body system, which is positioned in the centre of gravity. The flame system is translated and rotated with respect to the body system. In figure 3.3 there is a representation of the thrust misalignment in the flame coordinate system. It is possible to describe the thrust misalignment in the flame system with three parameters:

- dt: absence of perfect centering of the thrust application point;
- δ: in-plane angle between the thrust vector and the rocket axis;
- η: out of plane angle between the thrust vector and the rocket axis.

Indicating with S the thrust module, the thrust vector in the flame system can be defined as

$$\overrightarrow{T}^{(f)} = S \cdot \begin{Bmatrix} \cos(\eta)\cos(\delta) \\ \cos(\eta)\sin(\delta) \\ -\sin(\eta) \end{Bmatrix} \tag{3.6}$$

To express the thrust in the body system it is necessary to consider the relative position and rotation between the two systems. The two systems

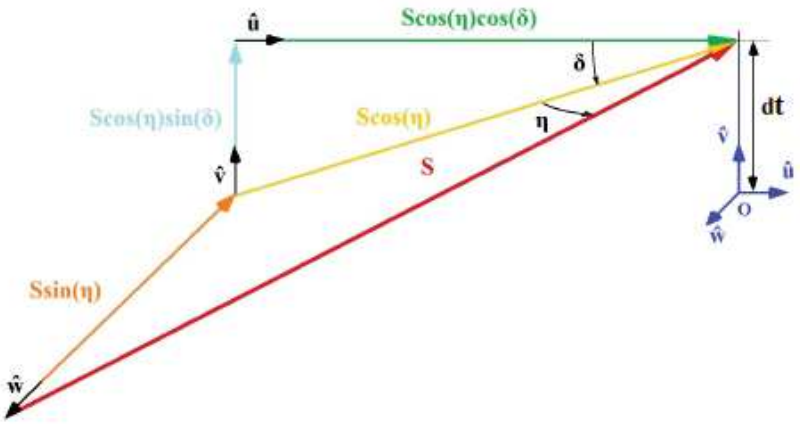

Figure 3.3. *Thrust misalignment representation in the flame coordinate system.*

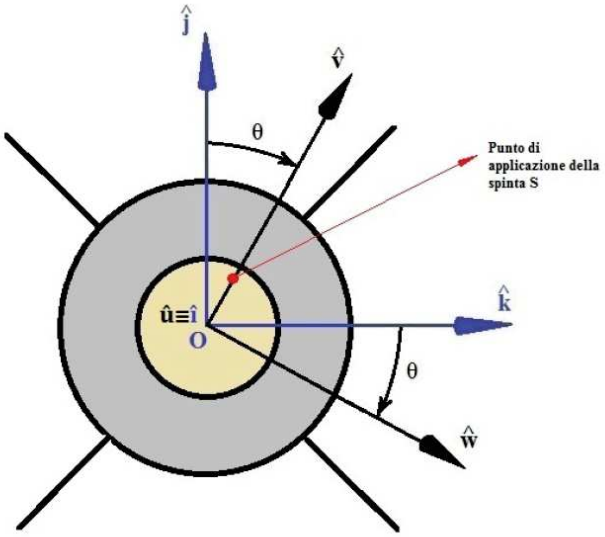

Figure 3.4. *Rotation between the flame and body coordinate systems.*

are rotated of an angle θ as shown in figure 3.4. Thus, the thrust in the body system, $\overrightarrow{T}^{(b)}$, depends on the matrix rotation $[M]_f^b$

$$\overrightarrow{T}^{(b)} = [M]_f^b \ \overrightarrow{T}^{(f)}$$

$$[M]_f^b = \begin{bmatrix} 1 & 0 & 0 \\ 1 & \cos(\theta) & -\sin(\theta) \\ 1 & \sin(\theta) & \cos(\theta) \end{bmatrix} \tag{3.7}$$

The thrust in the body system, which can be written as $\overrightarrow{T}$ since it is the thrust expression used in all further calculations, can then be written as follows

$$\overrightarrow{T} = S \cdot \begin{Bmatrix} \cos(\eta)\cos(\delta) \\ \cos(\eta)\sin(\delta)\cos(\theta) + \sin(\eta)\sin(\theta) \\ \cos(\eta)\sin(\delta)\sin(\theta) - \sin(\eta)\cos(\theta) \end{Bmatrix} \tag{3.8}$$

Once the thrust vector is completely defined in the body system, it is then possible to evaluate the moments it generates around the centre of gravity of the rocket. If $\overrightarrow{r}_{g-n}$ is the vector between the axis origin of the body system and the thrust application point, then the moment around the centre of gravity of the rocket caused by the thrust misalignment can be written as

$$\overrightarrow{M}_{thrust} = \overrightarrow{r}_{g-n} \times \overrightarrow{T} \tag{3.9}$$

The vector $\overrightarrow{r}_{g-n}$ depend on the values dt and θ and on the value $(L_{tot} - L_{cg})$ where L_{tot} is the total length of the rocket and L_{cg} is the position of the centre of gravity measured from the tip of the rocket.

$$\overrightarrow{r}_{g-n} = \begin{Bmatrix} L_{tot} - L_{cg} \\ dt\ \cos(\theta) \\ dt\ \sin(\theta) \end{Bmatrix} \tag{3.10}$$

The total moment due to the thrust misalignment can be written as

$$\overrightarrow{M}_{th} = S \cdot \begin{Bmatrix} -dt\ \sin\eta \\ dt\ \cos\eta\cos\delta\sin\theta + (L_{tot} - L_{cg}) \cdot [\cos\eta\sin\delta\sin\theta - \sin\eta\cos\theta] \\ -\cos\eta\cos\delta\cos\theta - (L_{tot} - L_{cg}) \cdot [\cos\eta\sin\delta\cos\theta + \sin\eta\sin\theta] \end{Bmatrix} \tag{3.11}$$

3.3.2 Fin Misalignment

The fin misalignment effects on the rocket trajectory can be defined as the consequences of three main factors:

- ξ_y: is the misalignments of the fin with respect to the y-axis, it is common to two fins;
- ξ_z: is the misalignments of the fin with respect to the z-axis, it is common to two fins;
- ξ_{diff}: is the differential misalignment of the fins, it is common of all fins.

The first two misalignments can be treated together, while the differential misalignment must be treated separately.

The lift force which derives from the misalignments ξ_y and ξ_z can be written as

$$F_{L_{fin}} = \frac{1}{2}\rho v^2 c_{l_{fin}} 2A_{fin} \tag{3.12}$$

The lift coefficient is a function of the misalignments

$$c_{l_{fin}} = a_0 \cdot \begin{Bmatrix} 0 \\ \xi_y \\ \xi_z \end{Bmatrix} \tag{3.13}$$

The factor a_0 depends on the Mach velocity at which the rocket is travelling

$$a_0 = \begin{cases} \dfrac{2\pi}{1+{}^2/_{AR}} \cdot \dfrac{1}{\sqrt{1-Ma^2}}, & Ma \leq 0.9 \\ \dfrac{2\pi}{1+{}^2/_{AR}} \cdot \dfrac{1}{\sqrt{1-0.9^2}}, & 0.9 < Ma < 1.1 \\ \dfrac{4}{\sqrt{Ma^2-1}} \cdot \left(1 - \dfrac{\Lambda}{2\,AR} \dfrac{1}{\sqrt{Ma^2-1}}\right) & Ma \geq 1.1 \end{cases} \tag{3.14}$$

where Λ and AR depend on the fin geometry

$$\Lambda = \frac{c_t}{c_r} \tag{3.15}$$

$$AR = \frac{b^2}{A_{fin}} \tag{3.16}$$

where c_t and c_r are respectively the chord at the fin tip and fin root, b is the wing span and A_{fin} the fin area. The lift force can be written as

$$F_{L_{fin}} = \rho v^2 a_0 A_{fin} \cdot \begin{Bmatrix} 0 \\ \xi_y \\ \xi_z \end{Bmatrix} \tag{3.17}$$

The moment around the centre of gravity generated by this lift force is

$$\overrightarrow{M}_{aer_{fin}} = \overrightarrow{r}_{g-fin} \times F_{L_{fin}} \tag{3.18}$$

where $\overrightarrow{r}_{g-fin}$ is the vector between the centre of gravity and the fin centre of pressure. The vector can be expressed as

$$\overrightarrow{r}_{g-fin} = \begin{Bmatrix} x_{g-fin} \\ \dfrac{(D\ +\ b)}{2} \\ \dfrac{(D\ +\ b)}{2} \end{Bmatrix} \tag{3.19}$$

Thus, the moment can be written as follow

$$\overrightarrow{M}_{aer_{fin}} = \rho v^2 a_0 A_{fin} \cdot \begin{Bmatrix} \dfrac{(D\ +\ b)}{2} \cdot (\xi_z\ -\ \xi_y) \\ -\ x_{g-fin}\, \xi_z \\ x_{g-fin}\, \xi_y \end{Bmatrix} \tag{3.20}$$

The fin differential misalignment is common to all four fins. Its principal consequence is the spin around the rocket axis. The fin lift force due to the misalignments is

$$F_{L_{spin}} = \frac{1}{2} \rho v^2 c_{l_{diff}} 4 A_{fin} \tag{3.21}$$

The differential lift coefficient depends not only on the differential misalignment ξ_{diff} but also on the velocity with which the rocket is spinning. The rocket, while rotating on its axis, changes the angle with which the fins see the air speed. Considering the velocity triangle shown in figure 3.5, it is possible to evaluate the decreasing in the differential misalignment due to the spin.

$$c_{l_{diff}} = a_0 \cdot \zeta \tag{3.22}$$

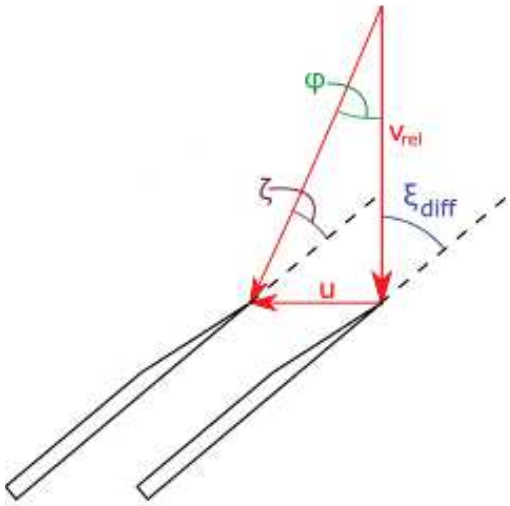

Figure 3.5. *Schematic of the decreasing in the angle between the fin and air due to the rocket spin.*

$$\zeta = \xi_{diff} - \phi \tag{3.23}$$

The angle ϕ can be evaluated from the velocities u and v_{rel}

$$\phi = \arctan \frac{u}{v_{rel}} \tag{3.24}$$

The velocity u with which the fins rotate depends on the angular velocity ω_x and the distance between the rocket axis and the centre of pressure of the fins.

$$u = \omega_x \cdot \frac{D + b}{2} \tag{3.25}$$

The lift coefficient due to the misalignment is then

$$c_{l_{diff}} = a_0 \cdot \left[\xi_{diff} - \arctan \left(\frac{\omega_x \, (D + b)}{2 \, v_{rel}} \right) \right] \tag{3.26}$$

Thus, the lift force deriving from the fin misalignment is

$$F_{L_{spin}} = \rho v^2 a_0 2 A_{fin} \cdot \left[\xi_{diff} - \arctan \left(\frac{\omega_x \, (D + b)}{2 \, v_{rel}} \right) \right] \tag{3.27}$$

Once the lift force deriving from the fin differential misalignment is evalu-

ated, it is possible to evaluate the moment due to it

$$\overrightarrow{M}_{spin_{fin}} = \overrightarrow{r}_{g-fin} \times \overrightarrow{F}_{L_{spin}} \tag{3.28}$$

The moment deriving from the differential misalignment of the fin is only around the rocket axis and can be written as

$$\overrightarrow{M}_{spin_{fin}} = \rho v^2 a_0 A_{fin} \cdot \begin{Bmatrix} (D + b) \cdot \left[\xi_{diff} - \arctan\left(\dfrac{\omega_x (D + b)}{2 v_{rel}} \right) \right] \\ 0 \\ 0 \end{Bmatrix} \tag{3.29}$$

3.3.3 Jet Damping

The Jet-Damping derives from the action of the exhausted gases flowing out of the nozzle. The Jet-Damping force depends on the mass flow of the gasses and on the angular velocity of the rocket, $\overrightarrow{\omega}$

$$\overrightarrow{J_D} = \dot{m} \cdot (\overrightarrow{\omega} \cdot \overrightarrow{r}_{g-n}) \tag{3.30}$$

The vector $\overrightarrow{r}_{g-n}$ is the vector between the centre of gravity and the exit point of the exhausted hot gasses. The product $(\overrightarrow{\omega} \cdot \overrightarrow{r}_{g-n})$ is the velocity of the hot gasses exit point expressed in m/s. The Jet-Damping can be written as

$$\overrightarrow{J_D} = \dot{m} \cdot \begin{Bmatrix} \omega_x \cdot (L_{tot} - L_{cg}) \\ \omega_y \cdot dt \cos(\theta) \\ \omega_z \cdot dt \sin(\theta) \end{Bmatrix} \tag{3.31}$$

The presence of the Jet-Damping can create a moment around the centre of gravity of the rocket.

$$\overrightarrow{M}_{J_D} = \overrightarrow{r}_{g-n} \times \overrightarrow{J_D} \tag{3.32}$$

The moment generated by the Jet-Damping can be expressed as follow

$$\overrightarrow{M}_{J_D} = \dot{m}\, dt \cdot \begin{Bmatrix} dt \cos(\theta) \sin(\theta) \cdot (\omega_y - \omega_z) \\ (L_{tot} - L_{cg}) \sin(\theta) \cdot (\omega_z - \omega_x) \\ (L_{tot} - L_{cg}) \cos(\theta) \cdot (\omega_x - \omega_y) \end{Bmatrix} \tag{3.33}$$

CHAPTER 4

Load Analysis

The main structure of a rocket is composed of the motor case, the supporting structures which should carry all principal loads, the payload associated structures, etc. The rocket airframe should be able to withstand all the applied loads without suffering major deterioration or permanent deformations.

The failure of the rocket main structure can be caused by loads of different nature. The loads can come, for example, from the handling and transportation, from the flight, from the aerodynamic, for thermal changes, from the system vibration, shocks, or buffeting. All applied loads can be divided into different load environments and the reaction of the structure to them changes from one environment to another.

The different loads acting on the structure can be translated into axial force, shear force and bending moment [19].

4.1 Types of Loads on the Rocket

On the main structure act different types of loads. These can differ from one phase of the rocket life to the other, starting from the assembly of the rocket to its flight. If the loads on the rocket exceed the structural limits, the rocket could break and be a threat to the surrounding areas, damaging buildings or causing casualties.

During the handling and transportation phases, the majority of the loads come from vibrations, possible shock and temperature differences or changes. Depending on the specific requirements of each rocket, the han-

dling and transportation can affect the entire rocket or separate parts that can later be assembled together. Launch loads are generally a function of the motor internal pressure, the acceleration of the rocket and the interactions between the rocket and the launch rail. The flight loads comprise the aerodynamic lift and drag, the inertia of the rocket components, the gravity and the internal pressure.

The rocket loading conditions can be divided into four main principal loading environments:

- *Short-Term static loads*: the loads on the structure increase gradually and the inertial loads are negligible;
- *Long-Term static loads*: these are static loads; however, due to their long duration, the material and flow characteristics become important;
- *Repeated loading*: with these loads, the structure experiences many stress variations; the frequency of these variations can be high or low, respectively in the case of vibrations and thermal cycling;
- *Dynamic loads*: these loads are usually of short-duration and can occur during the motor ignition transient behaviour or during handling.

The static loads can be investigated with the aid of load diagrams, in particular the diagrams of the axial and shear forces and bending moment. To study the dynamic loads it is necessary to know the dynamic response of the system. Dynamic amplifications allow the translation of the dynamic loads into equivalent static loads which can then be examined more easily.

The flight load conditions are considered short-term static loading conditions.

4.2 Flight Loads

During the flight phase, the external forces on the rocket are balanced by the body internal forces. Thus, the rocket is in dynamic equilibrium. During its flight, the major forces to which the rocket is subjected are the motor thrust, the aerodynamic lift ad drag forces, the inertial forces of the rocket components and the gravity force.

As already underlined, the rocket during its flight is in a condition of dynamic equilibrium. Thus, the acceleration vector can be evaluated from the equilibrium of the different forces

$$\overrightarrow{a}\, m_{tot} \;=\; \overrightarrow{F}_L \;+\; \overrightarrow{F}_D \;+\; \overrightarrow{T} \;+\; \overrightarrow{F}_g \tag{4.1}$$

where:

- $\overrightarrow{a}$ is the total acceleration of the rocket;
- m_{tot} is the total mass of the rocket;
- $\overrightarrow{F}_L$ is the lift force acting on the rocket;
- $\overrightarrow{F}_D$ is the drag force acting on the rocket;
- $\overrightarrow{T}$ is the thrust force;
- $\overrightarrow{F}_g$ is the gravity force.

The rocket acceleration can be divided in two components, the longitudinal acceleration and the normal acceleration

$$a_x\, m_{tot} \;=\; T \;-\; F_A \;+\; \; m_{tot}\, g_0 \sin(\beta) \tag{4.2}$$

$$a_N\, m_{tot} \;=\; F_N \;-\; m_{tot}\, g_0 \cos(\beta) \tag{4.3}$$

where:

- a_x is the rocket acceleration in the longitudinal direction;
- a_N is the rocket acceleration in the normal direction;
- F_A is the axial force acting on the rocket and derives from the projection of the lift and drag forces on the rocket axis;
- F_N is the normal force acting on the rocket and derives from the projection of the lift and drag forces on the rocket normal direction;
- g_0 is the acceleration due to gravity, 9.81 m/s;
- β is the attitude angle of the rocket, i.e. the angle between the rocket longitudinal axis and the horizontal.

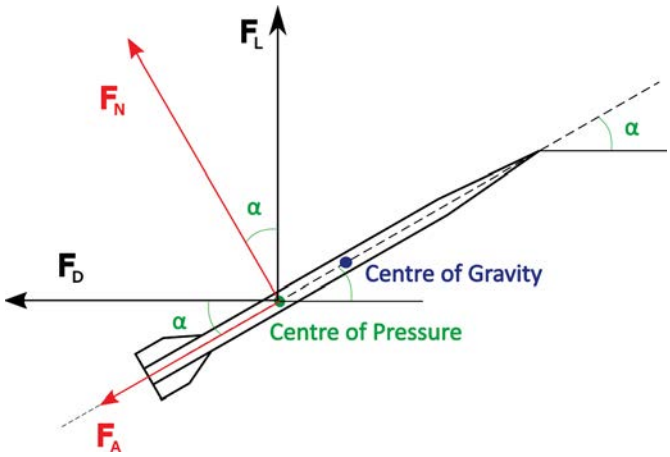

Figure 4.1. *Schematic of the Lift and Drag forces and of the normal and axial forces.*

The aerodynamic forces acting on the rocket are the lift and the drag. These loads can be projected on the rocket body system to obtain their contribution to the axial and normal forces. These contributions depend on the angle of attack, α, as in the schematic representation in figure 4.1.

$$F_A = F_D \cos(\alpha) - F_L \sin(\alpha) \tag{4.4}$$

$$F_N = F_D \sin(\alpha) + F_L \cos(\alpha) \tag{4.5}$$

Thus, it is possible to evaluate the rocket accelerations during its flight

$$a_x = \frac{T}{m_{tot}} - \frac{F_D \cos(\alpha) - F_L \sin(\alpha)}{m_{tot}} + g_0 \sin(\beta) \tag{4.6}$$

$$a_N = \frac{F_D \sin(\alpha) + F_L \cos(\alpha)}{m_{tot}} - g_0 \cos(\beta) \tag{4.7}$$

If the rocket is in thrusted flight, than the thrust has a non-zero value. If the rocket is in free-flight the value of the thrust is zero but the rocket is always in a dynamic equilibrium. Thus, the acceleration value depends on the flight phase analyzed.

In the above equations no misalignments have been taken into account. In the case these were present, their contributions both in the longitudinal and normal direction should be considered. The thrust misalignment and the presence of the Jet-Damping can be analyzed as an explicative example.

The thrust misalignment in the load analysis is a simplified version of the one described in the paragraph 3.3.1. In this analysis the misalignment can be described with two components: dt and δ. Thus, only the in-plane thrust misalignment is considered, ignoring the off-plane components. The thrust misalignment acts both on the axial and normal acceleration. The Jet Damping acts at the point of expulsion of the exhausted gases. It has a direction normal to the rocket axis and, thus, it does not contribute to the axial acceleration but only to the normal acceleration. The axial and normal components of the rocket acceleration become

$$a_x = \frac{T\cos(\delta)}{m_{tot}} - \frac{F_D\cos(\alpha) - F_L\sin(\alpha)}{m_{tot}} + g_0\sin(\beta) \tag{4.8}$$

$$a_N = \frac{T\sin(\delta)}{m_{tot}} + \frac{F_D\sin(\alpha) + F_L\cos(\alpha)}{m_{tot}} - g_0\cos(\beta) + \frac{J_D}{m_{tot}} \tag{4.9}$$

If other misalignments are present, their contribution must be account for in the same way as the Jet Damping and the thrust misalignment just described.

4.3 Loads on the Main Structure

The rocket reacts to the applied loads developing axial and shear forces and bending moments. These are not constant along the rocket length, but they change in consideration of the section at which they are evaluated and at the application point of the applied loads. To determine the variations of these loads along the rocket axis it is possible to divide the rocket into different stations.

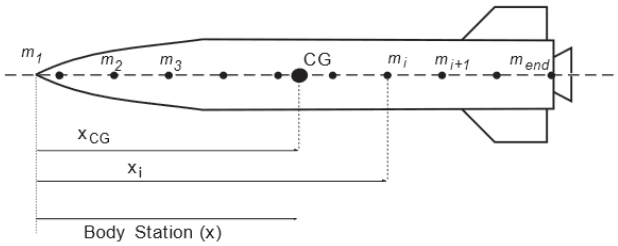

Figure 4.2. *Example of a lumped mass model of a rocket [19].*

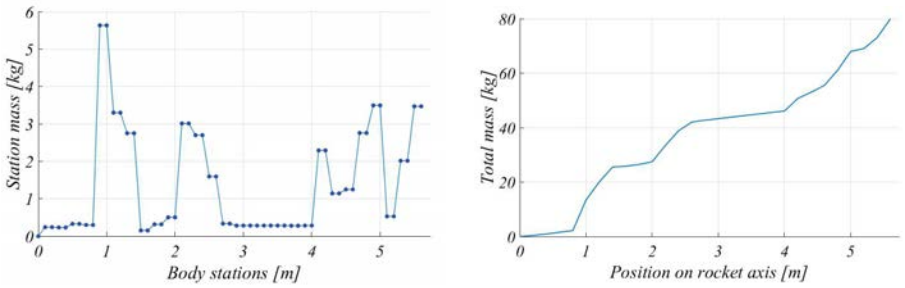

(a) Station Mass **(b)** Total Mass

Figure 4.3. *Mass distribution along the rocket axis.*

The first step in the evaluation of the load variations is the division of the total mass of the rocket into a series of concentrated masses, each one acting on a different station. An example of the rocket division into different masses is shown in figure 4.2. The masses of the different rocket stations are evaluated from the CAD assembly of the entire rocket, the distribution must keep unchanged the total mass of the system and the position of the centre of gravity. The mass distribution of the dry rocket, i.e. without oxidizer and fuel, is shown in figure 4.3. In the figure are reported the station masses and the total mass of the rocket. From the figure, it is possible to see the sections of the rocket which have a high or low mass. The low weight in the first 0.9 m is due to the presence of the nosecone, while the section that goes roughly from 2.5 to 4 m corresponds to the tank. The masses of the stations in such section are lower than the others because no oxidizer is present. The mass distribution and the rocket inertia change during the motor burn.

The lift and drag forces acting on the centre of pressure of the rocket can be divided into smaller forces acting on the different sections. The coefficients of the entire rocket are evaluated with another code as described in the paragraph 3.2. The total lift coefficient is the sum of the lift coefficients of the different segments of the rocket

$$c_{L_{tot}} = c_{L_{nc}} + c_{L_{body}} + c_{L_{fin}} \tag{4.10}$$

where:

- $c_{L_{tot}}$ is the lift coefficient of the entire rocket;

- $c_{L_{nc}}$ is the lift coefficient of the nosecone;
- $c_{L_{body}}$ is the lift coefficient of the rocket body;
- $c_{L_{fin}}$ is the lift coefficient of the fins.

The fin lift coefficient can be evaluated as follow

$$c_{l_{fin}} = a_0 \cdot \alpha \cdot \frac{A_{fin}}{A_{ref}} \tag{4.11}$$

where α is the attack angle a_0 depends on the geometrical characteristics of the fins and on the rocket velocity and the ration A_{fin}/A_{ref} is the ratio between the fin area and the cross-sectional area of the rocket. This ratio is non-dimensional and is necessary to reference all the lift coefficients to the same reference area. The parameter a_0 can be evaluated as

$$a_0 = \begin{cases} \dfrac{2\pi}{1 + 2/AR} \cdot \dfrac{1}{\sqrt{1 - Ma^2}}, & Ma \leq 0.9 \\ \dfrac{2\pi}{1 + 2/AR} \cdot \dfrac{1}{\sqrt{1 - 0.9^2}}, & 0.9 < Ma < 1.1 \\ \dfrac{4}{\sqrt{Ma^2 - 1}} \cdot \left(1 - \dfrac{\Lambda}{2\ AR} \dfrac{1}{\sqrt{Ma^2 - 1}}\right) & Ma \geq 1.1 \end{cases} \tag{4.12}$$

where Λ and AR depend on the fin geometry

$$\Lambda = \frac{c_t}{c_r} \tag{4.13}$$

$$AR = \frac{b^2}{A_{fin}} \tag{4.14}$$

where c_t and c_r are respectively the chord at the fin tip and fin root, b is the fin span. The fin contribution to the lift is a concentrated force acting in the station correspondent with the fin position. The lift contributions of the nosecone and the main body are distributed throughout their entire length. It is important to ensure that the distribution of the lift force does not create moments around the centre of gravity of the rocket. This condition is expressed as

$$c_{L_{tot}} x_{cp} = c_{L_{nc}} x_{nc} + c_{L_{body}} x_{body} + c_{L_{fin}} x_{fin} \tag{4.15}$$

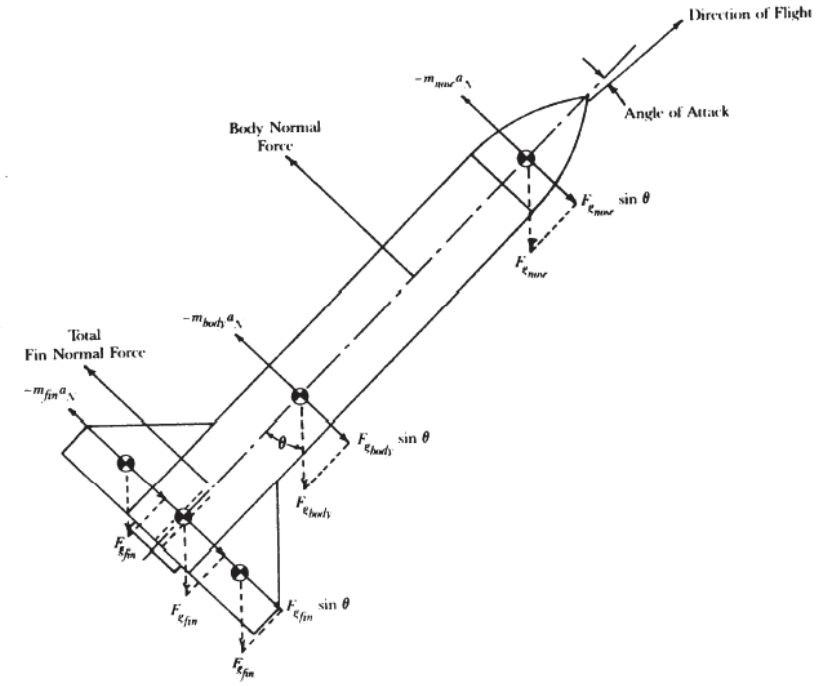

Figure 4.4. *Schematic of concentrated loads acting on a free-flight rocket [19].*

where x_{cp}, x_{nc}, x_{body}, x_{fin} are the positions of the centres of pressure measured from the nosetip. The nosecone and main body lift coefficients are evaluated combining the equations 4.10 and 4.15 in order to respect the total lift coefficient and the equilibrium of the moments. The coefficients so determined are then divided over the segments length to distribute the lift force over the different stations in which the segment is divided.

The same procedure can be used for the evaluation of the drag coefficient of the three section of the rocket. An example of the the scheme with which the forces act on the rocket is reported in figure 4.4.

The rocket longitudinal acceleration remains the same over the entire length of the rocket. However, the normal acceleration changes from station to station due to the presence of the angular acceleration. The angular acceleration contribution is given by the product between its value and the distance between the centre of gravity and the station at which the normal acceleration is being evaluated. The normal acceleration of the i-th station

can be evaluated as

$$a_{N_i} = a_N + \ddot{\theta} \cdot (x_{cg} - x_i) \tag{4.16}$$

The angular acceleration, in turn, depends on the total moment around the centre of gravity of the rocket. This depends on the normal force, i.e. the lift and drag projection on the normal direction, on the Jet Damping and on the thrust if a thrust misalignment is present

$$\ddot{\theta} = \frac{1}{I_{cg}} \cdot [F_N (x_{cg} - x_{cp}) + T \cos(\delta)\, dt + (T \sin(\delta) + J_D) \cdot (x_{cg} - L_{tot})] \tag{4.17}$$

The normal force acts on the centre of pressure of the rocket, the Jet Damping and the normal component of thrust act on the last section of the rocket, at L_{tot}. The axial component of the thrust generates a moment in the presence of a dt misalignment. The angular acceleration is constant for every section of the rocket. Nevertheless, its contribution to the normal acceleration changes due to the distance from the centre of gravity, the point around which the rocket is rotating.

Having determined the acceleration and the mass distribution at every station of the rocket, it is possible do evaluate the load diagrams of the actual forces acting on the rocket. The actual loads are a result of the external, internal and inertial forces. These loads apply primarily to the outer shell of the rocket and do not represent the loads experienced by the individual components.

4.3.1 Axial Load

The axial load comprehends all the forces acting on the longitudinal direction of the rocket. These forces are the motor thrust, the aerodynamic drag and lift components in the longitudinal direction, the inertia of the rocket mass acting in the longitudinal direction and the component of the gravitational force acting along the longitudinal direction. The axial load acting on the i-th section of the rocket can be evaluated as

$$F_{Ax_j} = \sum_{i=1}^{j} F_{A_i} + a_x \sum_{i=1}^{j} m_i + g_0 \sin(\beta) \sum_{i=1}^{j} m_i \tag{4.18}$$

$$F_{Ax_j} = \sum_{i=1}^{j} F_{D_i} \cos(\alpha) - \sum_{i=1}^{j} F_{L_i} \sin(\alpha) + (a_x + g_0 \sin(\beta)) \sum_{i=1}^{j} m_i \quad (4.19)$$

The thrust acts only on the last section of the rocket. Thus, on the last section it must be accounted for

$$F_{Ax_{end}} = F_{Ax_{end-1}} + T \cos(\delta) \quad (4.20)$$

4.3.2 Shear Load

The rocket reacts to the loads in the normal direction developing a shear load. The shear loads acting on the i-th station of the rocket is

$$F_{Sh_j} = \sum_{i=1}^{j} F_{N_i} - \sum_{i=1}^{j} m_i \, a_{N_i} + g_0 \cos(\beta) \sum_{i=1}^{j} m_i \quad (4.21)$$

$$F_{Sh_j} = \sin(\alpha) \sum_{i=1}^{j} F_{D_i} + \cos(\alpha) \sum_{i=1}^{j} F_{L_i} - \sum_{i=1}^{j} m_i \, a_{N_i} + g_0 \cos(\beta) \sum_{i=1}^{j} m_i \quad (4.22)$$

On the last section of the rocket act the Jet Damping and the thrust normal component as follows

$$F_{Sh_{end}} = F_{Sh_{end-1}} + T \sin(\delta) + J_D \quad (4.23)$$

4.3.3 Bending Moment

The bending moment derives from the combined action of the internal forces and external loads. The change in the bending moment between two points in the rocket can be expressed as the integral of the shear loads between those two points

$$M_{bn_j} - M_{bn_{j-i}} = \int_{x_{j-1}}^{x_j} F_{sh} \, dx \quad (4.24)$$

Since the rocket is divided into sections, the forces act only on them. Thus, the integral of the force over the distance between two points can be substituted with the product of the force by the distance

$$M_{bn_j} - M_{bn_{j-i}} = F_{sh_{j-1}} (x_j - x_{j-1}) \quad (4.25)$$

The bending moment can be evaluated from the shear force or directly from the loads that compose the shear load

$$M_{bn_j} = \sin(\alpha) \sum_{i=1}^{j} F_{D_i}(x_j - x_i) + \cos(\alpha) \sum_{i=1}^{j} F_{L_i}(x_j - x_i) \tag{4.26}$$

$$- \sum_{i=1}^{j} m_i \, a_{N_i}(x_j - x_i) + g_0 \cos(\beta) \sum_{i=1}^{j} m_i(x_j - x_i) \tag{4.27}$$

On the last section of the rocket the external moments must be added to all the other moments of the rocket

$$M_{bn_{end}} = M_{bn_{end-1}} + F_{Sh_{end-1}}(L_{tot} - x_{end-1}) - \sum_{i=1}^{n} M_i \tag{4.28}$$

In the sum of the external moments M_i are considered all those forces which were not taken into account in the previous sections like the thrust misalignment and the Jet Damping. There could also be a small moments deriving from the distribution of the normal force F_N along the rocket axis.

4.4 Load Diagram

The Axial and Shear forces depend only on the magnitude of the loads, while the bending moment depends also on the position in which the forces are applied. The Axial and Shear diagrams at the end of the rocket are equal to zero. For the Bending diagram at the end of the rocket, there is a small moment left, this is due to small errors and uncertainty in the forces application points. The load diagrams have been evaluated at $t = 30^-$, i.e. the moment just before burnout. This because in that instant the flight loads are more severe than in other phases.

In figure 4.5 it is possible to see the different components of the forces acting on a rocket with an elevation angle $\beta = 90°$ and a thrust misalignment with $dt = 0.01$ and $\delta = 0.25°$. It is possible to see how the thrust acts only on the last section of the rocket, both for the axial force and for the bending moment. In the latter case, the thrust misalignment is included in the sum of the external moments. The axial force magnitude increases along the rocket axis and this trend is the same in all the simulations because the

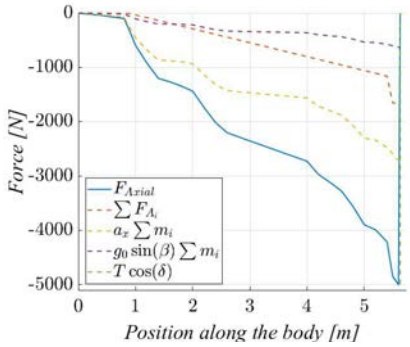

(a) Axial force and its components

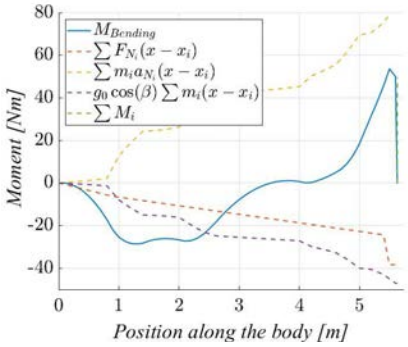

(b) Bending moments and its components

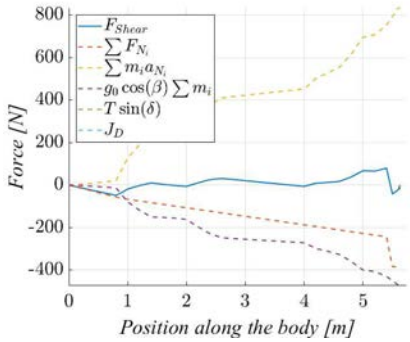

(c) Shear force and its components

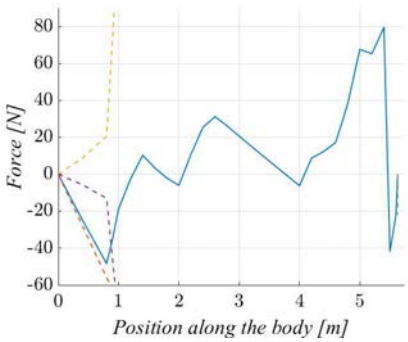

(d) Shear force - zoom

Figure 4.5. *Load diagrams for a trajectory β=90 °, dt=0.01 and δ=0.25 °.*

rocket is thrusted by the engine and all the other forces act against the rocket acceleration.

In figure 4.6 and 4.7 are reported the load diagrams of a trajectory with a launch angle of 90° and different thrust misalignments. The axial load diagrams have the same trend in both cases. The shear and bending diagram have a trend similar but mirrored around the rocket axis. This "mirrored-trend" derives from the fact that the thrust misalignments are one the opposite of the other and the rocket is launched with $\beta = 90°$.

The "mirrored-behaviour" is present but less pronounced if the launch angle is lowered. In the figures 4.8 and 4.9 are shown the shear load and bending moment diagrams for trajectories with $\beta = 80°$. In this case, the axial load diagrams are not reported since they would add no further information since they have the same trend and values of the axial load

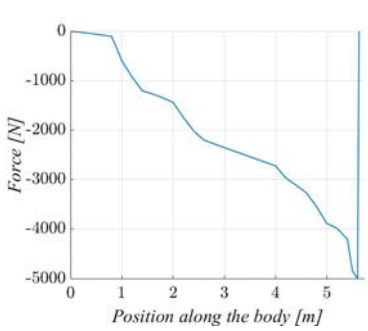

(a) Axial Force

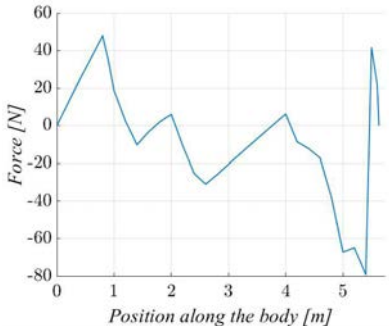

(b) Shear Force

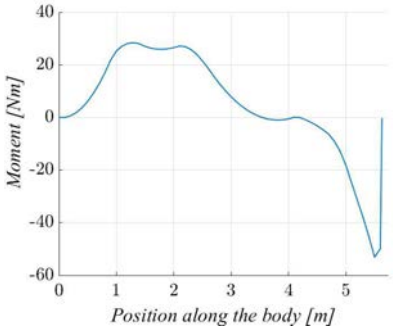

(c) Bending Moment

Figure 4.6. *Load diagrams for a trajectory* $\beta = 90°$, $dt = -0.01$ *and* $\delta = -0.25°$.

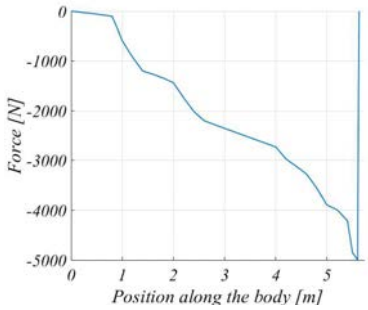

(a) Axial Force

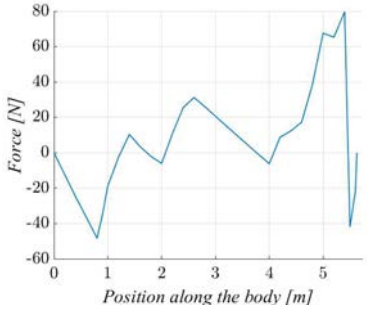

(b) Shear Force

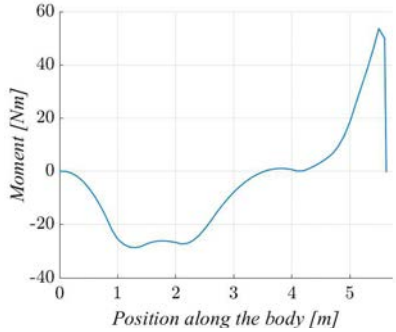

(c) Bending Moment

Figure 4.7. *Load diagrams for a trajectory* $\beta = 90°$, $dt = 0.01$ *and* $\delta = 0.25°$.

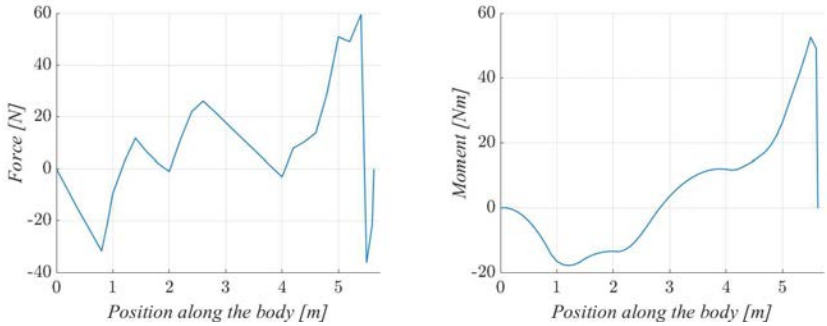

(a) Shear Force **(b)** Bending Moment

Figure 4.8. *Load diagrams for a trajectory* $\beta = 80°$, $dt = 0.01$ *and* $\delta = 0.25°$.

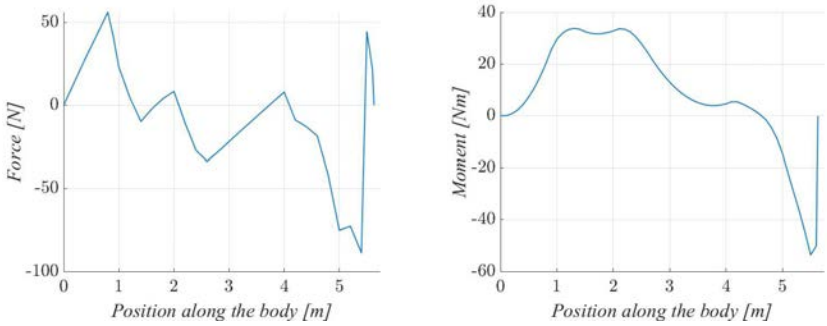

(a) Shear Force **(b)** Bending Moment

Figure 4.9. *Load diagrams for a trajectory* $\beta = 80°$, $dt = -0.01$ *and* $\delta = -0.25°$.

diagrams already reported for the 90° trajectories. It is possible to see how in the case of a non-vertical rocket flight there are some differences in the diagrams. Since the rocket is flying with a launch angle different from 90°, the thrust misalignments act differently if they operate in one direction or the others. In one direction, the misalignments force the rocket to move downward and so their action is helped by the force of gravity, while in the other direction, the misalignments force the rocket to move upward and so they have to fight against the force of gravity. It is possible to see the difference in both the shear and bending maximum values due to this effect.

The diagrams reported so far have misalignments whose effects on the rocket sum together, and, thus the loads on the structure are higher. In figure 4.10 and 4.11 are reported the shear and bending diagrams in the eventuality the effects of the misalignment tend to balance lowering the

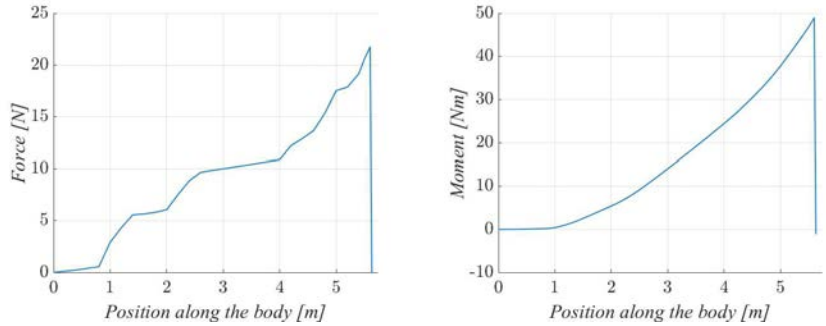

(a) Shear Force **(b)** Bending Moment

Figure 4.10. *Load diagrams for a trajectory* $\beta = 80°$, $dt = 0.01$ *and* $\delta = -0.25°$.

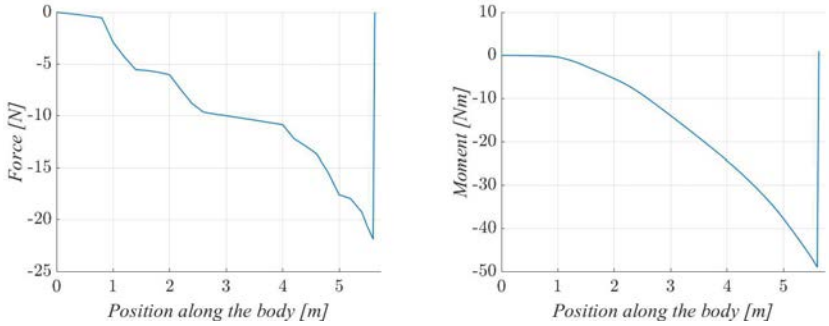

(a) Shear Load **(b)** Bending Moment

Figure 4.11. *Load diagrams for a trajectory* $\beta = 80°$, $dt = -0.01$ *and* $\delta = 0.25°$.

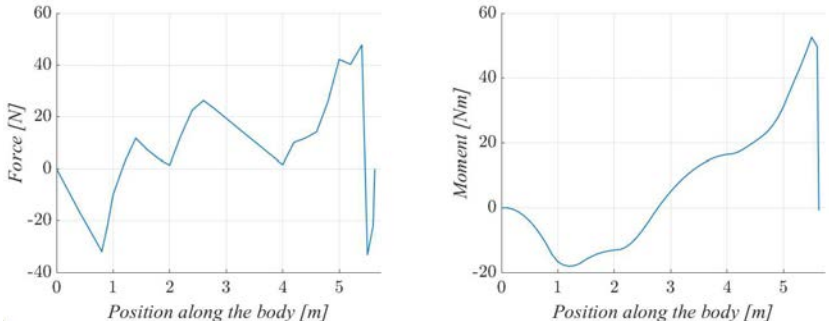

(a) Shear Force **(b)** Bending Moment

Figure 4.12. *Load diagrams for a trajectory* $\beta = 80°$, $dt = 0.01$ *and* $\delta = 0.25°$ *and a wind of* $5\,m/s$.

loads on the structure. The maximum values of the bending moment are the same as it was with the misalignments acting in the same direction, this because the maximum value of the bending moment derives from the thrust misalignment on the last section of the rocket $T\cos(\delta)\cdot dt \approx 5000\cdot 0.1 \approx 50\,Nm$. The shear maximum value is also in the last section of the rocket and depends on the thrust component normal to the rocket axis, which is $T\sin(\delta) \approx 5000\sin(0.25) \approx 22\,N$.

In figure 4.12 are shown the shear and bending diagram for a trajectory with a 5 m/s wind. Confronting the figures 4.8 and 4.12 it is possible to notice how with the same launch angle and thrust misalignments the wind presence does not cause significant changes in the load diagrams.

From the load diagrams reported above it is possible to see how the loads acting on the rocket during the flight phases do not cause the failure of the rocket structure.

CHAPTER 5

Safety Range Analysis

During all the different phases related to the launch of the sounding rocket, a casualty probability lower than 10^{-6} must be ensured. To have a higher safety margin and simplify the analysis, instead of evaluating the casualty probability if the rocket falls on the ground, a requirement of a land impact probability lower than 10^{-6} has been set.

As a first step, the nominal impact dispersion area is evaluated with the Monte Carlo technique. The analyses are then divided into different categories, taking into consideration the type of trajectory and the absence or presence of accidents. The trajectory is divided between nominal and non-nominal, with respect to the evolution over time of the flight path angle or, if not possible, the axial component of the velocity.

$$\gamma = \arctan\left(\frac{\sqrt{{v_y}^2 + {v_z}^2}}{v_x}\right) \tag{5.1}$$

On a nominal trajectory, the flight path angle must always decrease with time and the axial component must always increase during the thrusted flight. If these conditions are not met, then the rocket is flying on a non-nominal trajectory. The accidents force the sounding rocket to deviate significantly from its nominal trajectory. This could occur after an explosion, a nozzle-turn malfunction, or a fin loss.

For safety reasons a Flight Termination System is installed on the rocket. Its main objective is to prevent the rocket from exiting the safe zone and reach any areas where it could cause damages or casualties. The FTS ac-

tivation time depends on the flight condition because the human response time must be accounted for. Two different activation times are considered, 1 *second* and 3 *seconds*. The two times correspond to two different alarm codes, respectively orange code and green code.

5.1 Monte Carlo Simulations

The Monte Carlo is an important technique that allows the simulation of complex systems with many coupled degrees of freedom and models with considerable uncertainty in the inputs.

For safety reasons, it is important to perform a Monte Carlo on the trajectory of the sounding rocket. This because the trajectory is influenced by many factors, which can depend, for example, on the manufacturing of the rocket or the atmosphere condition at launch. With this technique, it is possible to determine a nominal dispersion area since it is possible to consider the non-linear effect of the combination of many different parameters.

To correctly perform a Monte Carlo analysis, it is fundamental to determine which parameters are constant in all simulations and which ones vary. The parameters variation is evaluated mostly taking into account manufacturing errors or variations in the engine behaviour.

With the results provided by these simulations, a nominal impact area can be determined. For a better evaluation of the probability in a specific area, it is possible to use the kernel density estimation.

In the trajectory simulation the three parachutes installed on the rocket are not considered. For this reason, the impact points found are shifted from their real position. Thus, the slant ranges are overestimated since the parachutes will slow the rocket down, shortening its descent range.

5.1.1 Parameters Variations

In the Monte Carlo simulations, a wide number of parameters is set to vary randomly with a probability distribution around a fixed nominal value. The values of these variations are fixed mostly considering the possible manufacturing errors. The nominal values, their variations and the probability distributions of all parameters are listed in the table 5.1.

Launch Parameter

Parameter	*Nominal*	*Variation*	*Dispersion*
Elevation β [°]	-	-0.3/+0.3	3 σ
Wind [m/s]	-	-0.25/+0.25	3 σ

Geometric Parameter

Parameter	*Nominal*	*Variation*	*Dispersion*
L_{cg} - initial [m]	3.327	-0.1/+0.1	3 σ
L_{cg} - end [m]	3.045	-0.1/+0.1	3 σ
y_{cp} [m]	0	-0.05/+0.05	3 σ
z_{cp} [m]	0	-0.05/+0.05	3 σ

Burn Parameter

Parameter	*Nominal*	*Variation*	*Dispersion*
Burning Time [s]	30	-3/+3	3 σ
I_{sp} constant [s]	207.72	-5%/+5%	3 σ

Thrust Misalignment

Parameter	*Nominal*	*Variation*	*Dispersion*
dt [m] *	0	-0.01/+0.01	3 σ
δ [°]	0	-0.25/+0.25	3 σ
η [°]	0	-0.25/+0.25	3 σ
θ [°]	0	0/360	Uniform

* the tail of the gaussian are cut at 5 mm

Fin Misalignment

Parameter	*Nominal*	*Variation*	*Dispersion*
ξ_y [°]	0	-0.1/+0.1	3 σ
ξ_z [°]	0	-0.1/+0.1	3 σ
$\xi_{differential}$ [°]	0	-0.1/+0.1	3 σ

Aerodynamic Parameter

Parameter	*Nominal*	*Variation*	*Dispersion*
c_d correction [-]	1.15	-0.15/+0.15	3 σ

Table 5.1. *Parameters nominal values and variations in the Monte Carlo simulations.*

Elevation angle β [°]	85.00	83.25	82.00	80.75	79.25	78.25
Wind Speed $[m/s]$	0	1	2	3	4	5

Table 5.2. *Elevation angle and wind speed pairs.*

Considering the manufacturing technique of the sounding rocket, the thrust misalignment value *"dt"* can be limited to a maximum of 0.005 m. Thus, still considering the same variation and distribution, if the randomly generated value is greater than 0.005 m, it is re-evaluated till it is lower.

In the table the nominal value for the elevation angle β and the wind speed are not listed. This because the Monte Carlo analysis is divided into 6 different sets of simulations, one for every wind speed between 0 and 5 m/s. For each wind level, a different elevation angle for the launch rail is implemented. One of the requirements in the selection of the elevation angle for every wind level is to prevent the rocket from impacting the ground more than 3 kilometres behind the launch site. In table 5.2 are listed the nominal values of all the pairs of elevation angle and wind speed used in the simulations.

The wind considered in the simulations is a tailwind, no headwind is considered. This because only a tailwind can create safety concerns. The rocket during thrusted flight experiences the weathervane effect. Therefore, a tailwind will force the trajectory to higher up and thus, the rocket could fall close to or behind the launch site. A headwind will force the trajectory to lower and, thus, it will not force the rocket to move close to the launch site. Being of no threat to public safety, since it moves the rocket far from the areas where it could cause damage, the headwind is not taken into account in the conduction of the Monte Carlo. In case of a tailwind, if the wind speed increases, the elevation angle of the launch rail must be lowered to prevent the rocket from moving too far behind the launch point.

The maximum wind speed considered in the simulation is 5 m/s, this because with a greater wind velocity the launch should be rescheduled.

5.1.2 Monte Carlo Results

The Monte Carlo analysis consists of a total of 120000 launches, 20000 for each of the $\beta - wind$ pair. The impact points deriving from the simulations

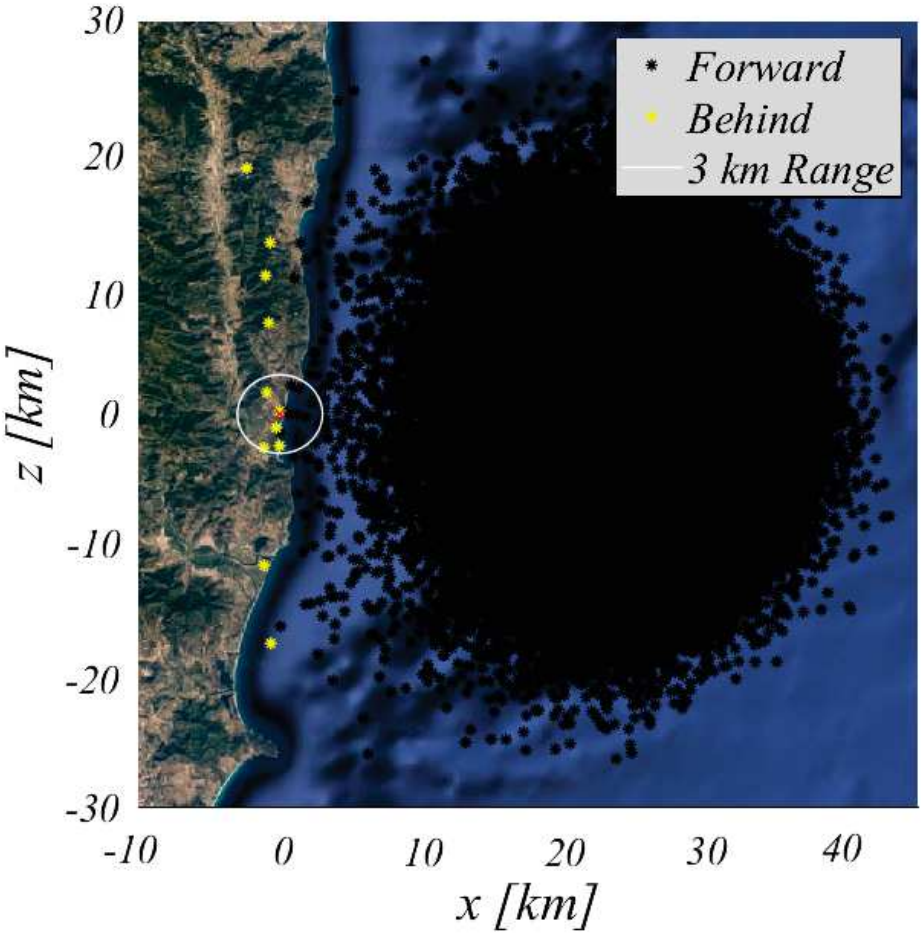

Figure 5.1. *Monte Carlo impact points overlaid with the map of the launch site.*

do not contemplate the presence of the parachutes on the rocket. Thus, the impacts are not in the same location where they will be if the parachute system works as designed. The presence of the parachute system will have different consequences on the impact points. The parachute should slow down the rocket, forcing it to shorten its descending phase. Thus, the slant range should be shorter.

The impact points obtained in the Monte Carlo are shown in figure 5.1. The launch site is denoted with the red cross and the white circle is a 3 km range around the launch site. On the map, the launches falling forward or behind the launch site are drawn with different colors.

The results of the Monte Carlo for each set of $\beta - wind$ pair are reported

in the tables 5.3. The distribution of the impacts in the various range of x-coordinates is almost the same for all the data sets. This is because the elevation angle has been lowered in order to avoid the rocket from falling behind the launch site as the wind speed increases. Thus, even if the wind speed changes from set to set, the distribution remains almost the same since the elevation angle of each set was initially fixed precisely to obtain this effect.

In 4 of the sets the rocket falls behind the launch site. For safety reasons, it is important to further analyse the impact point of these cases. The launches behind the launch site are divided into three categories: all the impacts behind the launch site; impacts behind the launch site with a slant range bigger than $3\,km$; impacts behind the launch site whose x-coordinates are behind $-3\,km$. In table 5.4 are listed the impacts belonging to these categories. In all the cases none of the impacts fall behind the $-\,3\,km$ line. A total of 11 launches fall behind the launch site and 6 of these have a slant range bigger than $3\,km$.

From this table it is possible to evaluate the probabilities for an impact behind the launch site. However, since the Monte Carlo provides only a limited data set, it is also possible to evaluate the cumulative probability of the same events. The cumulative distribution function describes the probability that a random variable, Ψ, which has a given probability distribution, is equal or less than ψ. Thus, the cumulative distribution function is given as

$$F_{\Psi}(\psi) = P(\Psi \leq \psi) \tag{5.2}$$

For the analysis of the impact points, a 90% cumulative probability is chosen as a reference value. The most probable value and the 90% cumulative probability for every $\beta - wind$ pair are listed in the tables 5.5. For every combination of elevation angle and wind speed, none of the launches falls more than $-3\ km$ behind the launch site. Thus, the probability of this event is 0.0% and the cumulative probability at 90% is 0.0115% for every single set. In table 5.6 are listed the 90% cumulative probability and the most probable value evaluated with all the launches.

$\beta = \mathbf{85.00}^\circ$

x [km]	#	*Probability*
< 0	3	0,02
5	27	0,14
10	162	0,81
15	815	4,08
20	3124	15,62
25	6214	31,07
30	6577	32,89
35	2843	14,22
40	230	1,15
45	5	0,03

$\beta = \mathbf{83.25}^\circ$

x [km]	#	*Probability*
< 0	0	0,00
5	10	0,05
10	90	0,45
15	477	2,39
20	2077	10,39
25	5395	26,98
30	7473	37,37
35	4017	20,09
40	449	2,25
45	12	0,06

$\beta = \mathbf{82.00}^\circ$

x [km]	#	*Probability*
< 0	0	0,00
5	19	0,10
10	99	0,50
15	560	2,80
20	2304	11,52
25	5515	27,58
30	7224	36,12
35	3783	18,92
40	479	2,40
45	17	0,09

$\beta = \mathbf{80.75}^\circ$

x [km]	#	*Probability*
< 0	3	0,02
5	21	0,11
10	123	0,62
15	646	3,23
20	2339	11,70
25	5579	27,90
30	7120	35,60
35	3720	18,60
40	442	2,21
45	7	0,04

$\beta = \mathbf{79.25}^\circ$

x [km]	#	*Probability*
< 0	1	0,01
5	13	0,07
10	93	0,47
15	532	2,66
20	1896	9,48
25	4975	24,88
30	7405	37,03
35	4405	22,03
40	670	3,35
45	10	0,05

$\beta = \mathbf{78.25}^\circ$

x [km]	#	*Probability*
< 0	4	0,02
5	34	0,17
10	136	0,68
15	687	3,44
20	2346	11,73
25	5356	26,78
30	7059	35,30
35	3858	19,29
40	512	2,56
45	8	0,04

Table 5.3. *Distribution of the impact points with the the x-coordinate of the point used as criterion.*

β	#	*Range* $>$ 3 *km*	$x < -3$ *km*
85.00°	3	1	0
83.25°	0	0	0
82.00°	0	0	0
80.75°	3	2	0
79.25°	1	1	0
78.25°	4	2	0
Total	**11**	**6**	**0**

Table 5.4. *Launches behind the launch site for the Monte Carlo simulation, all launches, launches with slant range > 3 km and launches with x < -3 km.*

Behind launch site

β	#	*Most probable*	90% *Cumulative*
85.00°	3	0.015%	0.033%
83.25°	0	0.0%	0.012%
82.00°	0	0.0%	0.012%
80.75°	3	0.015%	0.033%
79.25°	1	0.005%	0.019%
78.25°	4	0.020%	0.044%

Behind launch site Slant range > 3 km

β	#	*Most probable*	90% *Cumulative*
85.00°	1	0.005%	0.019%
83.25°	0	0.0%	0.012%
82.00°	0	0.0%	0.012%
80.75°	2	0.010%	0.027%
79.25°	1	0.005%	0.019%
78.25°	2	0.010%	0.027%

Table 5.5. *Probabilities of an impact behind launch site for each set of Monte Carlo simulations.*

	#	*Most probable*	90% *Cumulative*
Behind Launch site	11	0.009%	0.014%
Slant range $>$ 3 *km*	6	0.005%	0.009%
Behind $-$ 3 *km*	0	0.0%	0.002%

Table 5.6. *Overall probabilities of an impact behind launch site.*

5.1.3 Impact Envelope

With all the impact points of the Monte Carlo, an impact envelope for the nominal flights can be evaluated. As a requirement, this envelope must include at least the 99.7% of the impacts.

To include a high number of launches keeping the dimensions limited a complex shape has been chosen, a rendering of the shape of the impact envelope is shown in figure 5.2. The impact envelope is composed of three parts:

- *Initial Cone*: starting from the launch site, the impact envelope has a cone shape; the height in this part is not constant, it starts from zero at the launch site and increases with a fixed climbing angle till it reaches the maximum altitude;
- *Central Rectangular*: the central part of the envelope is a rectangle with a constant height equal to the maximum height;
- *Final Semi-Ellipse*: the closure of the envelope is a semi-ellipse whose centre lies at the end of the central rectangle; its height is not constant, at the connection with the central rectangle the height is the maximum height and then it decreases till it is equal to zero at the farthest point from the launch site.

The dimensions of the envelope are evaluated considering the coordinates of the impact points. The semi-ellipse centre is given by the mean values of all the impact points. The semi-axes of the ellipse are set equal to the $3\,\sigma$ dispersion of all impact points. The central rectangular dimensions depend on the dimensions of the semi-ellipse z-axis. Its width is the same as the semi-ellipse and it connects the initial cone with the semi-ellipse. The opening angle of the initial cone is the maximum angle calculated using the coordinates of the impacts, while the climbing angle is the maximum angle calculated using the apogee point of the impact whose slant range is the smallest. The length of the initial cone is calculated using the opening angle and the semi-ellipse width. In the evaluation of the parameters of the envelope, all launches falling forward the launch site are taken into account.

The dimensions of this impact envelope are listed in table 5.7 and its projection on the ground is shown in figure 5.3. The axis origin corresponds

Figure 5.2. *Impact Envelope 3D shape.*

with the launch site. The impact envelope includes the 99.76% of the total launches. The opening and climbing angles are respectively almost 180° and 90°. Thus, the initial cone is almost non-existent and the impact envelope is composed mostly of the central rectangle. Due to these characteristics, for safety reasons it is better to determine another envelope whose dimensions are smaller.

For the new impact envelope, instead of taking into account all launches forward the launch site, the 0.1% (i.e. 20 impacts over each set of 20000) are excluded. The launches excluded are those falling forward the launch site whose x-coordinates are the smallest. The parameters of the impact envelope so evaluated are listed in table 5.8 and its projection on the ground is shown in figure 5.4. This impact envelope includes the 99.72% of the total launches.

Considering the difference in the number of launches included in the two envelopes, this is less than 0.04%. However, the dimensions are very different. Both envelopes are completely forward the launch site, but the first envelope is very close to the vertical line passing through the launch site due to the initial cone opening angle. In the impact envelope with the smaller opening angle, the safe zone described is farther from any areas where the rocket could cause damages or casualties.

Properties	*Value*
Initial cone - opening angle [°]	179.70
Initial cone - length [km]	0.05
Ellipse centre - x [km]	25.53
Ellipse centre - z [km]	0.00
Ellipse radius - x [km]	16.85
Ellipse radius - z [km]	20.45
Maximum height [km]	34.00
Climbing angle [°]	89.63
Launches Included	99.76%

Table 5.7. *Impact envelope dimensions considering all launches.*

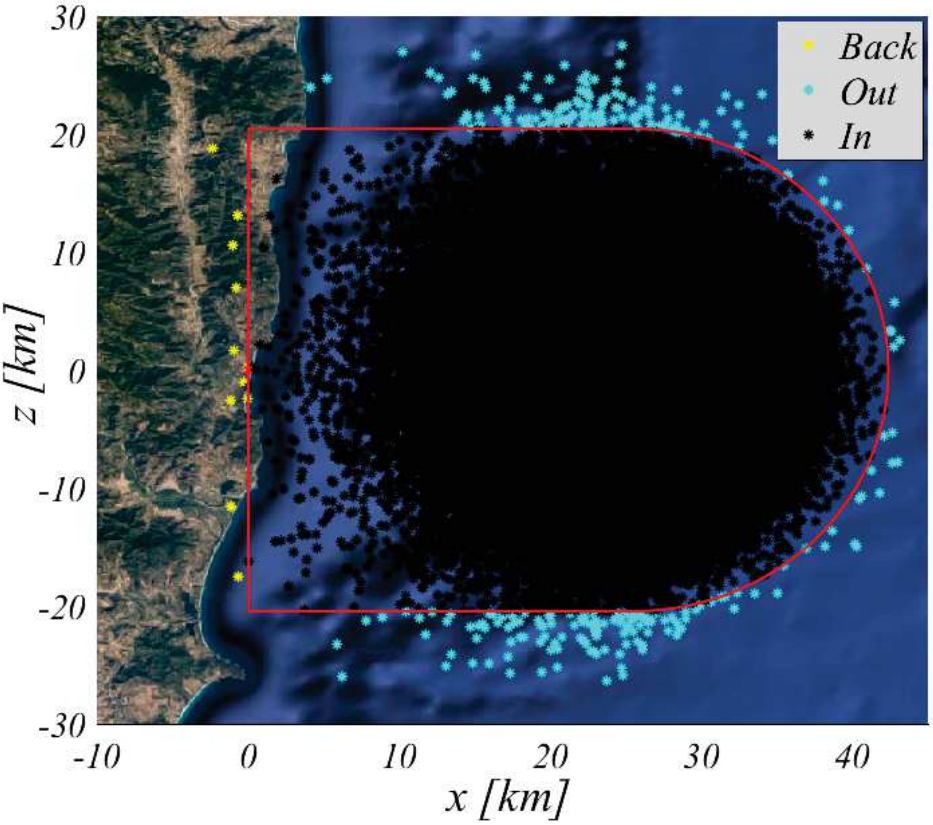

Figure 5.3. *Impact envelope ground projection considering all launches.*

Properties	*Value*
Initial cone - opening angle [°]	153.06
Initial cone - length [km]	4.89
Ellipse centre - x [km]	25.55
Ellipse centre - z [km]	0.00
Ellipse radius - x [km]	17.72
Ellipse radius - z [km]	20.44
Maximum height [km]	34.00
Climbing angle [°]	85.02
Launches Included	99.72%

Table 5.8. *Impact envelope dimensions excluding the* 0.1% *of launches.*

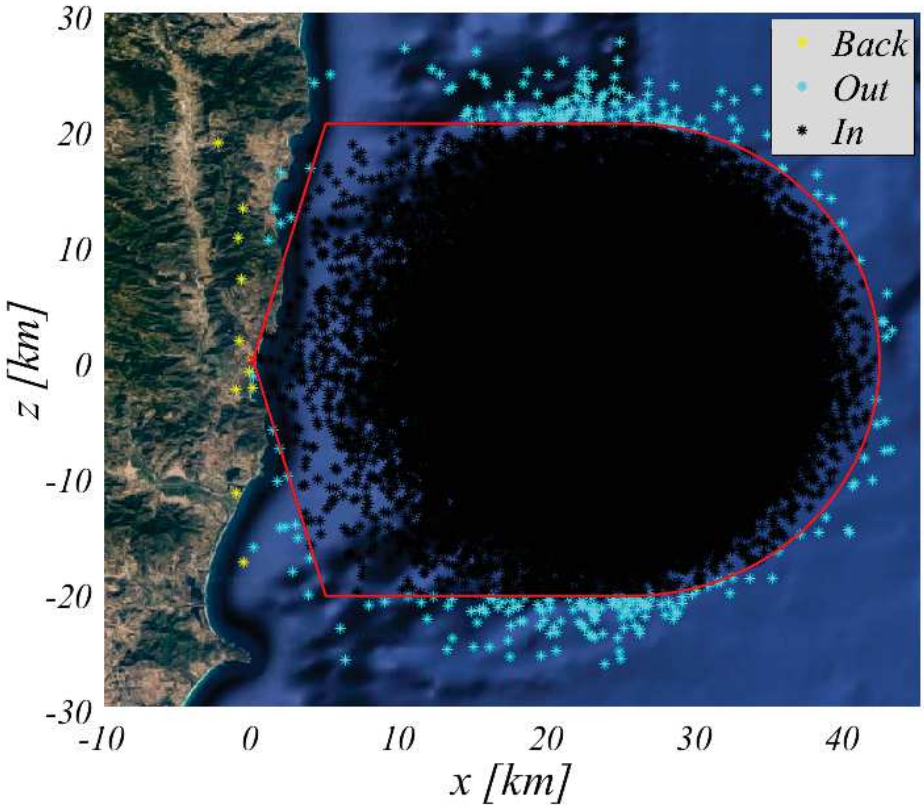

Figure 5.4. *Impact envelope ground projection excluding the* 0.1% *of launches.*

The two impact envelopes include both more than 99.7% of the impacts as required. Observing the differences in the ground projections, for safety reasons it is preferable to choose the envelope evaluated with the 0.1% exclusion.

5.1.4 Kernel Density Estimation

The Monte Carlo technique provides a wide number of impact points deriving from the action of different combinations of parameters that vary randomly. However, to evaluate the probability of an impact in a specific area, it is possible to calculate the kernel density of the impact probability. Using a kernel function, it is possible to transform a "sharp" point location, such as the rocket impact point, into an interval centred around the initial point. Thus, the probability of an impact in a specific area depends not only on the actual impacts in that area, but also on those impacts close to it.

The impact probability is calculated using a Kernel Density Estimation across a grid created on the impact area. The size of the grid cells defines the resolution of the probability density. A point influences the surrounding areas and its influence radius depends on the parameters used in the kernel density estimation.

Considering the $\{x_1, ..., x_n\}$ to be independent and a sample of n observations. The observations are of a population with a probability distribution function unknown $f(x)$. The kernel estimation $\hat{f}(x)$ of the original distribution function $f(x)$ is evaluated with a kernel function $K(x_i, t)$ defined for every $i - th$ point

$$\hat{f}(x) = \frac{1}{n} \sum_{i=1}^{n} K(x_i, t) \tag{5.3}$$

The kernel function transforms a sharp point location into an interval centred at the point. However it does not change the overall value. Thus, the integral of the kernel function must be equal to 1

$$\int_{-\infty}^{+\infty} K(x_i, t)dt = 1 \tag{5.4}$$

The above property of the integral of the kernel function ensures the nor-

malization of the kernel density estimation as follows:

$$\int_{-\infty}^{+\infty} \hat{f}(x)dt = \frac{1}{n}\sum_{i=1}^{n}\int_{-\infty}^{+\infty} K(x_i,t)dt = 1 \tag{5.5}$$

The kernel function can be defined both with symmetric and asymmetric functions. Considering a symmetric property, the kernel function can be written as

$$K_{sym}(x,t) = \frac{1}{h}K\left(\frac{x-t}{h}\right) \tag{5.6}$$

where h is the Bandwidth of the kernel and is a smoothing factor applied to the sample. The use of different bandwidths in the kernel evaluation influences the final result. Figure 5.5 shows as the value of the smoothing parameter h has a great influence on the overall final value. If the bandwidth is too large there is an over-smoothing of the sample and important information can be lost, if the value is too small insignificant detail can be shown instead of the overall behaviour. There are many criteria for the bandwidth selection, however, it is better to adjust its value as a compromise in relation to the data sample analyzed. The kernel function can have different shapes, considering a Gaussian distribution, the value of the kernel is

$$K(t) = \frac{1}{2\pi}e^{t^2/2} \tag{5.7}$$

The univariate case described above can be extended to a bivariate case with good results. Considering a bivariate symmetric kernel function, $\hat{f}(x,y)$ is

$$\hat{f}(x,y) = \frac{1}{nh_xh_y}\sum_{i=1}^{n} K\left(\frac{x_i-x}{h_x}, \frac{y_i-y}{h_y}\right) \tag{5.8}$$

where $\{x_i, y_i\}, \quad i = 1,2,..,n$ is a sample of data and h_x and h_y are the bandwidths in the two different direction. In practice, the bivariate kernel function can be determined with the product kernel estimator which can be written as follows

$$\hat{f}(x) = \frac{1}{nh_xh_y}\sum_{i=1}^{n} K\left(\frac{x_i-x}{h_x}\right) K\left(\frac{y_i-y}{h_y}\right) \tag{5.9}$$

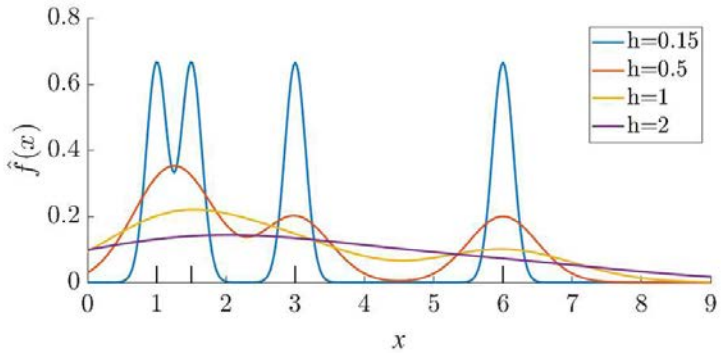

Figure 5.5. *Example of kernel density estimation with different bandwidth values.*

Considering the impact points of the Monte Carlo simulation, the kernel density estimation allows for a better evaluation of the impact probability over a specific area.

The kernel density is estimated on a grid where the cells have a dimension of roughly 0.11×0.12 km. The Bandwidths are equal in both directions and this value should not be too small respect to the cell sides. In the following figures, from 5.6 to 5.8, there are the kernel density estimations of the rocket impact probability evaluated with different bandwidth value, specifically 1.5 km, 3 km and 0.1 km. For all the bandwidth values, both a colormap and a map of the launch area overlaid with the isolines are shown.

Confronting figure 5.6 and figure 5.7, it is evident the effect of the bandwidth as smoothing factor. Considering the figure 5.8, the kernel density estimation has a shape more similar to the scatter plot of the impact points than to the other kernel density estimations. This happens because the bandwidth is small and has the same magnitude order as the cell dimensions. Thus, the impact points are shown more like a sharp point than like an interval centred on the impact point.

The integral of the kernel density estimations with all bandwidths is above 0.99. For definition, it should be equal to 1. However, its value is slightly lower because the grid points are the only points where the kernel is evaluated and, thus, if a point falls in the middle of the cells its peak value will not be seen on the grid points, which will see only lower values.

For safety reasons, it is important to evaluate the possibility of an impact

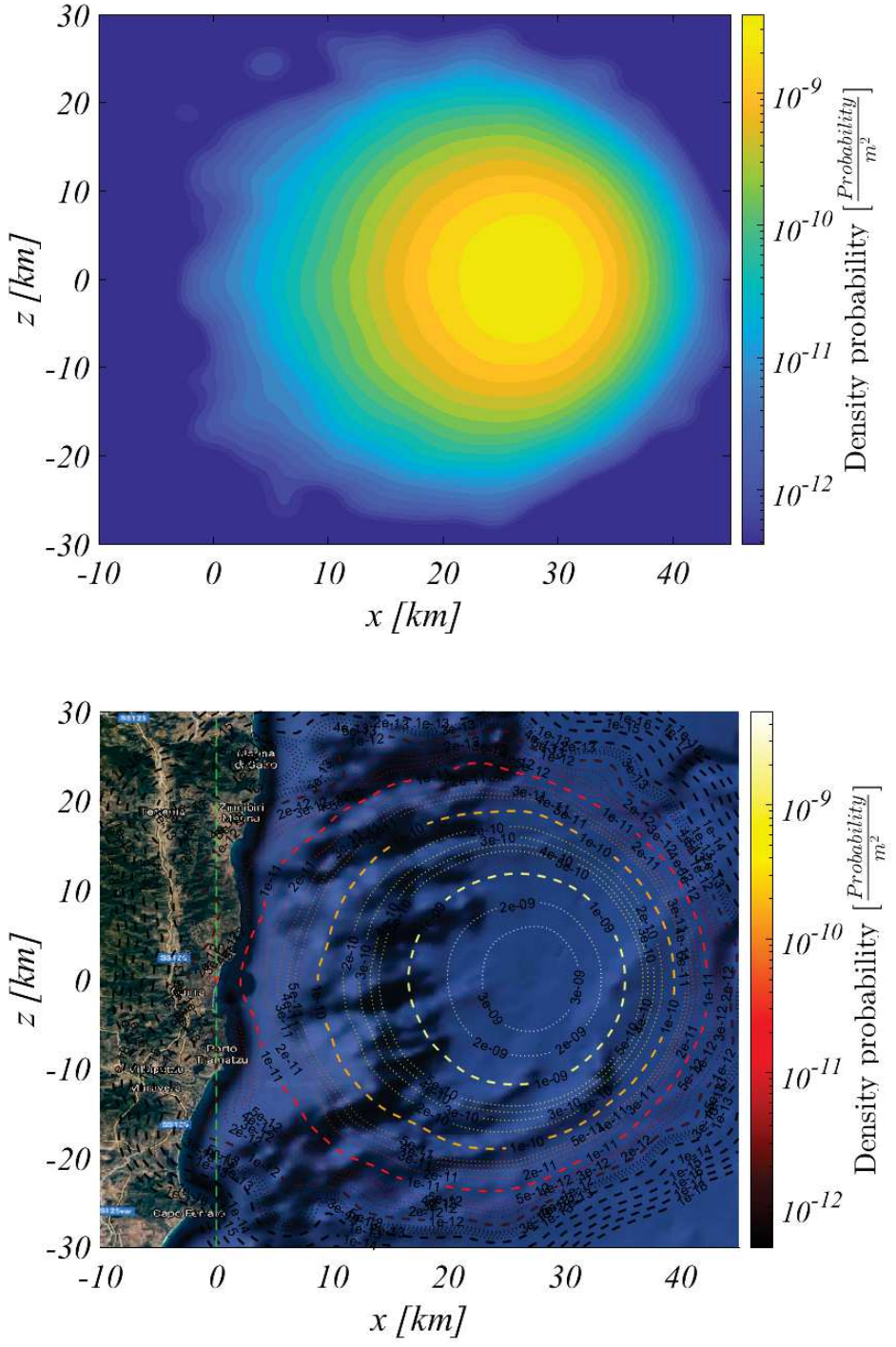

Figure 5.6. *Kernel density estimation with bandwidth* $1.5\,km$.

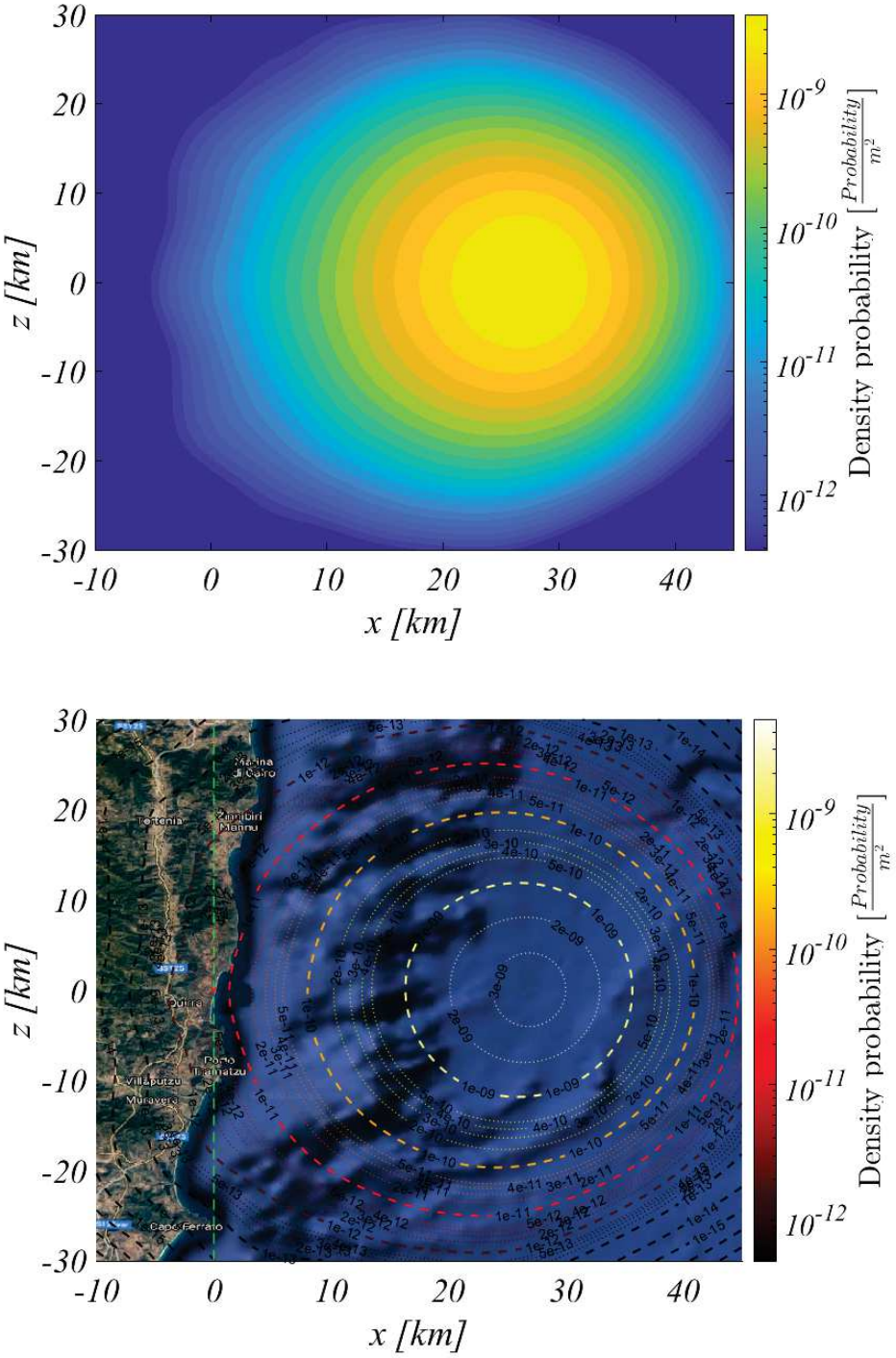

Figure 5.7. *Kernel density estimation with bandwidth* $3.0\,km$.

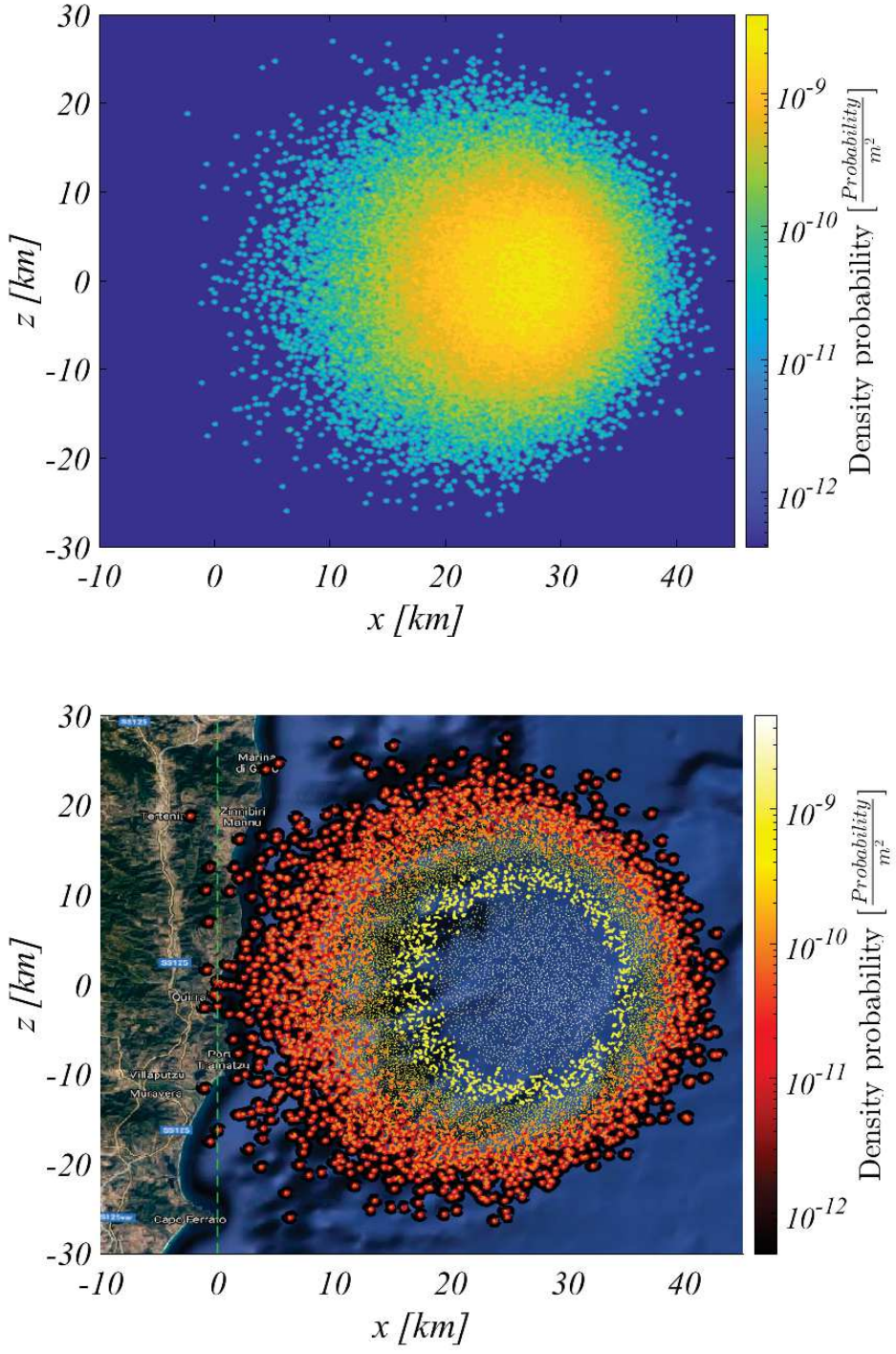

Figure 5.8. *Kernel density estimation with bandwidth* $0.1\,km$.

	Behind launch site	Behind $-3\ km$
Most Probable	0.0092%	0.0%
Cumulative Probability 90%	0.0138%	0.0019%
Kernel Density $h = 0.1\ km$	0.0101%	$2.6 \cdot 10^{-15}$%
Kernel Density $h = 1.5\ km$	0.0114%	0.0009%
Kernel Density $h = 3.0\ km$	0.0256%	0.0049%

Table 5.9. *Probability of an impact behind launch site evaluated with different methods.*

behind the launch site. Using the kernel density estimation it is possible to integrate the kernel function from the end of the grid to the vertical line passing through the launch site. The value so obtained should be roughly the same as the probabilities already determined in the previous paragraphs for the same event. The probabilities evaluated from the integration of the kernel density, the 90% cumulative and the most probable values are reported in table 5.9.

The integral of the kernel density estimation with a bandwidth of 0.1 km is very close to the most probable value. This because the small value of the bandwidth allows only a few points to contribute significantly to the integral. In particular, looking at the probability of an impact behind the $-3\ km$, it is evident how the small bandwidth value creates a value almost equal to zero, as it is for the most probable value.

The integral with the 3 km bandwidth has a bigger value than all the others. Even if this probability is higher, it must be considered how in this case many points contribute to the integral behind the launch site. In fact, with a 3 km bandwidth even the launches falling 1 km forward the launch site contribute to the kernel integral behind it.

Leaving aside the case with bandwidth 3 km, it is possible to infer how the probability of an impact behind the launch site is lower than 0.015% and the probability of an impact more than 3 kilometres behind the launch site is lower than 0.002%.

5.2 Wind Influence

The wind can have important effects on the trajectory of the sounding rocket. Thus, it is important to evaluate how any changes in its magnitude or direction could affect the impact points. The launch rail is set prior to launch to compensate for the prevailing winds. The elevation angle β balances the longitudinal winds, while the azimuth angle ψ balances the lateral winds.

The rocket is more susceptible to the wind effects when its velocity is low. This is explained by the ratio between the wind velocity and the rocket velocity. As the rocket accelerates, the ratio decreases and the effects become less significant. The wind has different effects on the rocket when it's thrusting and when it isn't, respectively the weathervane turning and the drift.

The wind considered in the Monte Carlo is a wind moving from west to east. This wind forces the rocket to return to land during its thrusted flight due to the weathervane effect. If the wind has the opposite direction it lowers the rocket trajectory and so there is no reason to further analyze this eventuality since it is of no danger.

For safety reasons, in the analyses only a wind velocity up to 5 m/s is considered. With a wind velocity above 5 m/s the launch should be rescheduled. However, a wind velocity above this value has a very low probability to occur, as shown in figure 5.9. The data on the intensity and strength distribution are recorded at the weather station of Capo San Lorenzo, about 3 km from the actual launch site. From the figure, it is also possible to infer how a longitudinal wind is more probable than a lateral one.

The wind influence analysis is divided into three strands:

- *Wind speed time variability*;
- *Wind weighting function*;
- *Lateral wind.*

To determine the correct angles for the launch rail, the frequency of the wind speed fluctuations must be evaluated. This because the time

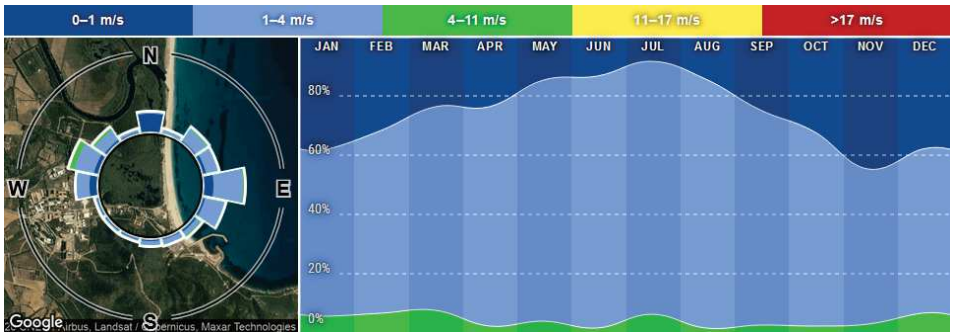

Figure 5.9. *Wind direction and strength distribution measured at Capo San Lorenzo, close to the launch site.*

between the wind measurement and the actual rocket lift-off can vary and it is important to ensure how a possible change in the wind speed will pose no threat to safety.

The wind intensity is measured at the launch site. However, as the rocket moves and climbs higher in the atmosphere, both the speed and the direction of the wind could change. These variations can depend on numerous factors, one of which is the altitude. Thus, it is important to weight the effects of a change in the wind velocity with altitude and how far from the nominal impact point the rocket could fall.

In the Monte Carlo analysis only a longitudinal wind is implemented. Thus, the effects of a lateral wind are not taken into account in the Monte Carlo results. The deviation from the nominal impact point must be evaluated to ensure it will not pose any threat to public safety.

5.2.1 Wind Speed Time Variability

The rail launch elevation angle is set prior to launch to compensate for the prevailing longitudinal winds. However, since ground operations before launch can take some time, it is necessary to evaluate the time variability of the winds.

In figure 5.10 there is a representation of the energy spectrum of the wind speed. There are three peaks in the energy corresponding to different time variability. The peaks correspond to a 4-day cycle, a 12 hours cycle (diurnal peak) and cycles of a few minutes (turbulent peak). Between the diurnal and turbulent peaks, there is a spectral gap.

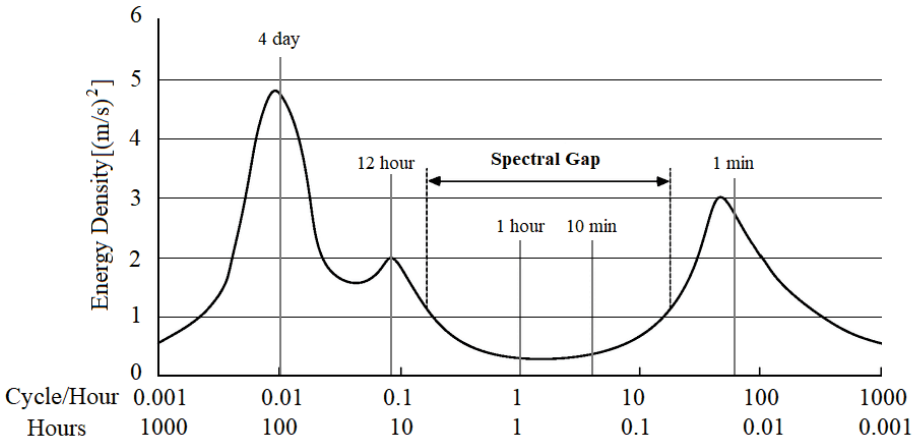

Figure 5.10. *Energy spectrum of near-ground wind speed.*

Bearing in mind the presence of the spectral gap, it is possible to justify the adjustment of the elevation angle with the wind measured prior to launch. The time variability within a couple of hours has a very low energy density.

The turbulent peak has a cycle of a couple of minutes. Thus, the wind speed can change from the value for which the launch rail is set. However, since the cycle is so short, it is possible to monitor the wind instantaneous velocity and wait for the right minute to launch.

Taking into account the different wind speed fluctuations, it is possible to compensate for the prevailing winds. The fluctuations with a cycle between a couple of hours and 10 minutes have a very low energy density, justifying the adjustment of the launch rail in consideration of the winds. The turbulent peak has a cycle of a couple of minutes. It is not possible to adjust the launch rail to compensate for these winds. However, it is possible to set the launch rail compensating for those winds with longer fluctuations cycles and then wait for a couple of minutes with the rocket ready for launch till the winds measured instantly match the desired value.

5.2.2 Wind Weighting

The launch rail elevation angle is set depending on the wind speed measured on the ground before launch. However, the wind speed could change at different altitudes. Thus, it is important to evaluate the wind weighting

function and so to determine the influence of possible changes in the wind speed intensity while the rocket is flying.

To examine the wind influence, several simulations with all nominal values for the rocket and different wind conditions are performed. In particular, the nominal trajectories with $\beta = 85.00°$ and $\beta = 83.25°$ are analyzed. In both cases, the trajectory on which the wind weighting function is evaluated is without wind, i.e. a wind speed of 0 m/s, and he impact point is used as a reference. For each wind level, another reference point is determined when the wind acts on the entire rocket trajectory. Then the trajectories with the wind acting only above a certain altitude are simulated. Below this altitude, the wind velocity is set equal to zero.

The weighting function is described by equation 5.10.

$$Weight_i = \frac{(x_0 - x_i)}{(x_0 - x_{ref})} \cdot 100 \tag{5.10}$$

where:

- $Weight_i$ is the weighting function value for a fixed altitude;
- x_0 is the impact point with a 0 m/s wind speed;
- x_i is the impact point with a a constant wind acting only above a fixed altitude;
- x_{ref} is the impact point with a constant wind acting during the entire flight.

The wind weighting function is determined for both elevation angles for all wind levels, i.e. from 1 m/s to 5 m/s. In figure 5.11 are shown the weighting function for all wind levels for $\beta = 85.00°$. The difference between the weighting functions is low and so the mean value can be used instead of all the different functions. The mean value of the wind wieghting function for $\beta = 85.00°$ and $\beta = 83.25°$ are represented in figure 5.12.

The wind weighting function decreases rapidly as the altitude increases. The wind accomplishes 90% of its effects in the first 0.5 km and this value increases to 95% at 1 km. Taking into account an altitude of 200 m, the wind weighting function has a mean value of less than 20%. Assuming the

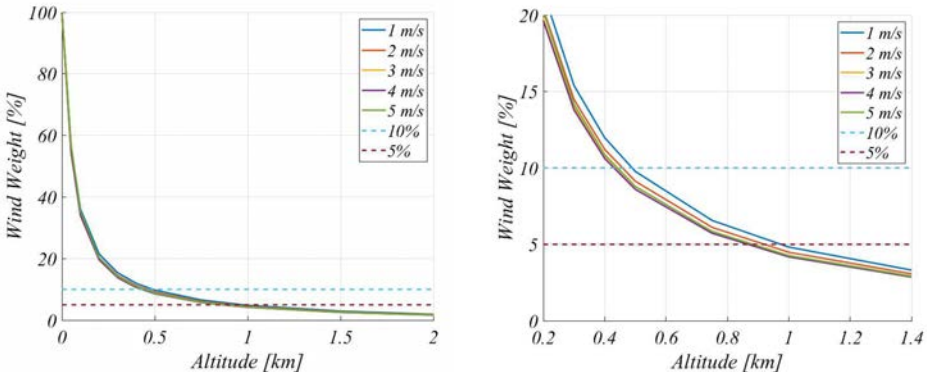

Figure 5.11. *Wind weighting function with* $\beta = 85.00°$ *for all wind levels.*

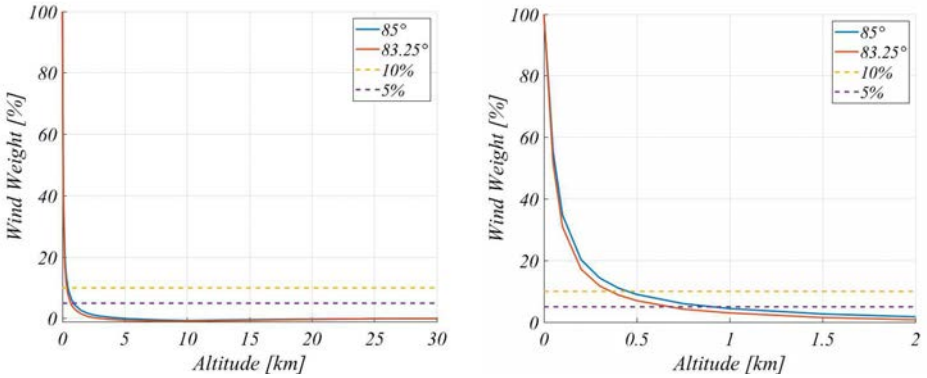

Figure 5.12. *Wind mean weighting function* $\beta = 85.00°$ *and* $\beta = 83.25°$.

wind velocity to be constant in the first 200 m, any changes in the wind velocity up to 5 m/s should create a shift in the impact point of less than 20% of its nominal value. Assuming the wind velocity to be constant in the first 500 m, any changes in the wind velocity should create a shift of less than 10%. Specifically, in this latter case, an elevation angle of 85° without wind has an impact point of 25.2 km from the launch site, while with a 5 m/s wind the impact is 22.2 km, thus with a shift of less than 9%.

The analyses on the wind weighting function justify the elevation angle adjustment with the wind measured on the ground, yet knowing how its value could change while the rocket climbs higher in the atmosphere.

5.2.3 Lateral Wind

The wind implemented in the Monte Carlo is a west-east wind, along the longitudinal direction of flight. No lateral wind is considered. Thus, for safety reasons, the effects of a lateral wind on the rocket trajectory must be evaluated. This allows for a correction of the azimuth launch angle to prevent the rocket from deviating too much from its nominal trajectory.

As shown in figure 5.9, the lateral winds have lower intensities than the longitudinal ones. Thus, for the analysis on the lateral wind, its intensity is fixed at 1, 2, 3 m/s. The nominal trajectories without lateral winds are used as a reference to determine the deviation values. The lateral deviations for all elevation angles are listed in table 5.10. The lateral deviation with the same later wind is similar for all elevation angles. As the lateral wind intensity increases, also the lateral deviation increases. The azimuth angle needed to correct the lateral deviation increases as the lateral wind intensity increases. For the same lateral wind velocity the azimuth angle needed to correct the lateral deviation is higher for the higher elevation angles. This is due not to the elevation angle itself, but to the value of the longitudinal wind. In fact, to every elevation angle corresponds a different intensity of longitudinal wind.

Elevation β	1 m/s *lateral wind Deviation* $[km]$	2 m/s *lateral wind Deviation* $[km]$	3 m/s *lateral wind Deviation* $[km]$
85.00°	6.69	13.00	18.53
83.25°	6.57	12.74	18.18
82.00°	6.60	12.81	18.25
80.75°	6.62	12.83	18.25
79.25°	6.52	12.61	17.87
78.25°	6.52	12.59	17.84
Mean	6.59	12.76	18.15

Table 5.10. *Lateral deviations on nominal trajectories with different lateral wind velocity.*

For every elevation angle and lateral wind, it is necessary to evaluate the azimuth angle which cancels the lateral deviation. The required azimuth angles are listed in table 5.11.

Looking at the azimuth with $\beta = 85°$ and $w_{lat} = 3\ m/s$, the angle

Elevation β	1 m/s *lateral wind Azimuth* ψ	2 m/s *lateral wind Azimuth* ψ	3 m/s *lateral wind Azimuth* ψ
85.00°	15.5°	32.5°	53.0°
83.25°	11.5°	23.5°	36.5°
82.00°	9.5°	19.5°	30.0°
80.75°	8.0°	16.5°	25.0°
79.25°	7.0°	14.0°	21.0°
78.25°	6.5°	13.0°	19.0°

Table 5.11. *Azimuth angle ψ which cancels the lateral deviation for different lateral wind velocity.*

needed is of 53°. Many parameters influence the rocket trajectory and an azimuth angle greater than 45° has to be discarded for safety reasons. If the maximum azimuth angle is set to 45°, than the lateral deviation for the 85.00° elevation and 3 m/s lateral wind is reduced to 4.35 km.

In the unlikely event of a lateral wind with velocity greater than those analyzed, the deviation will be larger than those already calculated. The azimuth angles needed will in turn increase. Setting the maximum azimuth value at 45°, the azimuth angles and lateral deviation with a 5 m/s lateral wind are listed in table 5.12. With the elevation angles of 79.25° and 78.25° the azimuth angles can be lower than 45° and still cancel the lateral deviation.

Elevation β	*Azimuth* ψ	*Lateral deviation* $[km]$
85.00°	45.0°	16.89
83.25°	45.0°	10.97
82.00°	45.0°	6.27
80.75°	45.0°	1.12
79.25°	38.0°	≈ 0
78.25°	33.5°	≈ 0

Table 5.12. *Lateral deviation with a maximum value $\psi = 45°$ and a 5 m/s lateral wind.*

With a maximum azimuth of 45° the lateral deviation can be cancelled for all lateral wind up to 3 m/s and all cases except for 85.00° elevation. However, even for this case the lateral deviation can be reduced to less than

5 km.

It is important to underline how the lateral wind affects mostly the lateral component of the impact point, while the shift in the longitudinal component is negligible.

5.3 Explosion Analysis

The possibility of an explosion of the HTP used in the Sounding Rocket has been considered. In the oxidizer tank, there are 60 kg of liquid HTP. The explosion of the content of the tank could provoke two major possible dangers:

- Pressure wave due to the detonation of the HTP;
- Fragments from the oxidizer tank or other parts of the rocket.

To evaluate the possible damages of the explosion it is important to determine the explosive power of the HTP. In all calculation as a safety margin, the 60 kg of HTP have been considered as 60 kg of TNT. This is a very strong assumption since the H_2O_2 in liquid phase has a very low probability of detonation. A detonation can occur only in the presence of contaminants, strong confinement and a powerful ignition source. These conditions should not occur during both the ground operations and flight phase. Pure HTP is not sensitive to shock, mechanical impact or adiabatic compression. Moreover, the equivalent energy release of pure HTP is between $14 - 40\%$ of TNT, the exact value depends on various factors. Thus, setting the explosive mass equal to 60 kg means strongly overestimating the real explosive mass. However, for safety calculations, this is acceptable since the results will have an intrinsic safety margin [7].

5.3.1 Blast Wave Overpressure

A detonation can create a high-intensity shock front that moves outward from the explosion point. As the shock wave expands, it decreases its strength and velocity while increasing in duration. The overpressure caused by an explosion depends on the mass and the type of the explosive, the dis-

tance from the explosion origin and whatever the explosion occurs on the ground or in open-air.

A first classification of the burst is according to the position of the detonation: open air burst and ground burst. In an open-air burst, the blast wave generated by the explosion can move freely without obstacles and so it is not amplified. In a ground burst, the initial shock wave is reflected by the ground and thus its intensity is amplified.

The effects of the explosion and the deriving blastwave can be evaluated using a set of equations called the Sadovsky formulas[23]. The overpressure value can be evaluated with the equations 5.11

$$\Delta p_{air} = 0.84 \frac{\sqrt[3]{k_t m_{exp}}}{r} + 2.7 \frac{\sqrt[3]{(k_t m_{exp})^2}}{r^2} + 7 \frac{k_t m_{exp}}{r^3}$$

$$\Delta p_{ground} = 0.95 \frac{\sqrt[3]{k_t m_{exp}}}{r} + 3.9 \frac{\sqrt[3]{(k_t m_{exp})^2}}{r^2} + 13 \frac{k_t m_{exp}}{r^3} \tag{5.11}$$

where:

- Δp_{air} is the overpressure caused by an explosion in open air;
- Δp_{ground} is the overpressure caused by an explosion on the ground;
- r is the distance from the origin point in meters;
- m_{exp} is the explosive mass in kilograms;
- k_t is a parameter such as the product $k_t m_{exp}$ is the TNT equivalent mass.

These equations are not precise in the proximity of the explosion point because they become singular and overestimate the overpressure. However, they are precise for overpressure values below 10 atmospheres.

During ground operations, the whole 60 kg of HTP can be considered as detonating and, as already explained, to insert a safety margin $k_t = 1$ so that the 60 kg of HTP are considered to be 60 kg of TNT.

Blastwave can be a threat to both buildings and people. To determine how dangerous an explosion of the HTP in the tank could be, three reference values are taken into account:

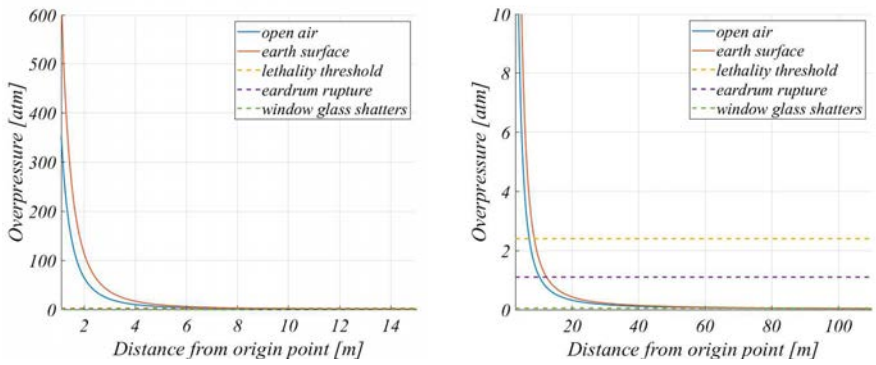

Figure 5.13. *Overpessure values for an explosion both in open air and on the ground.*

- *Lethality threshold*: 2.4 atm;
- *Eardrum rupture*: between 0.35 atm and 1.1 atm;
- *Windows glass breaking*: 0.05 atm.

The Lethality threshold is defined as the level at which the overpressure has the 1% chance to cause a casualty; the eardrum rupture is the most common injury at a low level of overpressure; the windows glass breaking is the first damage on buildings with a blastwave.

In figure 5.13 are shown the overpressure values for both an open-air and ground explosion. In the figure are also present the three reference values described above. The blastwave overpressure decreases quickly moving away from the explosion origin point. After 10 m, the blastwave causes an overpressure which is below the lethality threshold for both types of explosions. At 15 m, the values are below 1.1 atm. Thus, no injures on people should occur 15 m off the explosion origin. Since the lowest level of overpressure which causes damage to buildings is 0.05 atm, to avoid the windows glass breaking it is necessary to be at a distance of roughly 100 m.

It is possible to infer that an explosion is of no threat for the public with a distance of more than 15 m and for buildings with more than 100 m. Concluding, the pressure wave deriving from an improbable detonation of the entire HTP quantity stored in the tank will not damage anything above 100 m from the explosion point.

5.3.2 Debris Range

In the event of an explosion, a wide number of debris could be generated from the tank and the adjacent parts of the sounding rocket. To exclude any possible danger, it is important to evaluate how far these debris could travel [27]. There are two main sources of debris: the tank itself and the rocket parts close to the tank. In the first case, the debris are accelerated directly by the explosion since they enclose the mass which explodes, while in the second case the debris are accelerated by the blastwave that strikes them.

An explosion could occur both during ground operation and during flight. Thus, the debris range should be estimated with an explosion happening at different heights. On the ground, the whole 60 kg contained in the tank constitute the explosive mass, while, as the rocket climbs higher, the mass that could detonate decreases. Taking into account a vertical launch and the nominal burning time of 30 s, the mass decreases from 60 to 0 kg from 0 to 10 km.

All debris are considered to travel on a ballistic trajectory with an initial angle of 45°. An explosion and the subsequent fragmentation of the structures around the tank could generate a wide number of debris with a high degree of uncertainty in their mass and aerodynamic characteristics. Analyzing the drag coefficient c_D of various aerodynamic shape, the value ranges between $c_D = 0.5$ for a sphere to $c_D = 2$ for a narrow strip face-on with the flow. For the debris trajectory, c_D is set to 0.5. Thus, its value is a safety margin on the debris range because it is the lowest value the debris could experience and the distance travelled by the debris is the maximum range they could have.

5.3.2.1 Tank Fragments

Analysing the tank, the fragment velocity can be determined using the Gurney formulas. These are a set of equations which provide an estimation of the velocities of the fragments deriving from a detonation. These equations have different formulations depending on the geometry of the problem. For a configuration with a cylindrical body closed by two flat-plates, the Gurney

formulas can be expressed as in the equations 5.12 [5, 11].

$$v_s = \frac{D}{(A+1)} \cdot \left(\left(\frac{m_1}{C} + A^2 \frac{m_2}{C} + \frac{1}{3} \frac{(A^3+1)}{(A+1)} \right) \frac{h}{r} + \left(\frac{m_s}{C} + \frac{1}{2} \right) \right)^{-\frac{1}{2}}$$

$$v_1 = D \cdot \left(\left(\frac{m_1}{C} + A^2 \frac{m_2}{C} + \frac{1}{3} \frac{(A^3+1)}{(A+1)} \right) + (A+1) \left(\frac{m_s}{C} + \frac{1}{2} \right) \frac{r}{h} \right)^{-\frac{1}{2}}$$

$$v_2 = \frac{D}{A^2} \cdot \left(\left(\frac{m_1}{C} + A^2 \frac{m_2}{C} + \frac{1}{3} \frac{(A^3+1)}{(A+1)} \right) + \frac{(A+1)}{A^2} \left(\frac{m_s}{C} + \frac{1}{2} \right) \frac{r}{h} \right)^{-\frac{1}{2}} \tag{5.12}$$

where:

- v_s is the velocity of the fragments from the cylinder side wall;
- v_1 *and* v_2 are the velocities of the fragments from the cylinder end-plates;
- C is the TNT equivalent mass;
- m_1 *and* m_2 are the masses of the end-plates;
- r is the radius of the cylinder;
- h is the height of the cylinder;
- D is the Gurney constant and depends on the type of the explosive;
- A is a parameter that depends on the different masses of the problem

$$A = \left(1 + \frac{2m_1}{C} \right) / \left(1 + \frac{2m_2}{C} \right) \tag{5.13}$$

Considering the masses and the geometry of the tank, it is possible to fix the values of some of the parameters: $C = 60\ kg$, $m_1 = m_2 = 0.6\ kg$, $r = 0.2\ m$, $h = 1.6\ m$ and $A = 1$ because the two end-plates have the same mass.

The fragments generated by the tank are made of composite material or thin metallic sheets. In particular, the sidewalls of the tank are made only

of composite materials, while in the end-plates there are both composite metallic components. All the tank fragments have a small thickness, only a few mm. Fixing the thickness of the debris, the ballistic coefficient depends only on its density and on the drag coefficient, as described in equation 5.14.

$$c_B = \frac{m}{c_D A_f} = \frac{\rho \, thick \, A_f}{c_D A_f} = \frac{\rho \, thick}{c_D} \tag{5.14}$$

The thickness can be fixed to 3 mm since the side walls have a thickness of 2.91 mm and the metallic parts of the end-plates have a similar thickness. Since the fragments can be of different materials, there are two different density: the composites part have a density of 1600 kg/m^3 while the metallic parts have a density of 8000 kg/m^3. The two densities are chosen to match those of the rocket parts. The composite which forms the rocket structures has a density of 1600 kg/m^3. The metallic parts of the rocket are made of different metals, however, since a high density value gives a high ballistic coefficient, the density value chosen is the maximum value found in the rocket.

Explosion height	*Cylinder fragment*		End-plate	*End-plate Range [km]*	
	v_s $[m/s]$	*Range [km]*	v_1 $[m/s]$	*Composite*	*Metal*
0 km	489	0.057	3753	0.080	0.359
2 km	485	0.069	3724	0.096	0.432
4 km	480	0.082	3677	0.117	0.524
6 km	469	0.100	3589	0.142	0.640
8 km	440	0.121	3358	0.174	0.785

Table 5.13. *Ranges for the debris generated by the tank with an explosion at different heights.*

The ranges of the different debris are shown in table 5.13. Examining the table it is evident how the fragments of the sidewalls of the tank have a lower velocity than the others and so they have a smaller range. Comparing the ranges of the end-closure debris, it is possible to deduce how the metallic debris travell farthest. This because they have a higher density and thus a higher ballistic coefficient. The trajectories of the fragments after the explosion at different heights are shown in figure 5.14.

The tank fragments fall all within 1 km from the explosion point.

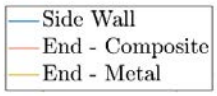

(a) Figure Legend

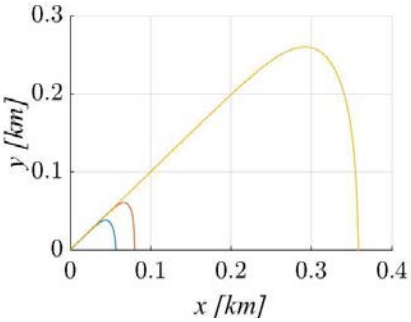

(b) $h_{exp} = 0\ km$

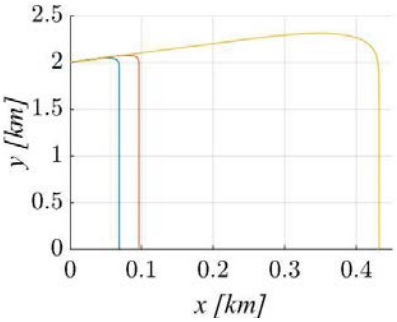

(c) $h_{exp} = 2\ km$

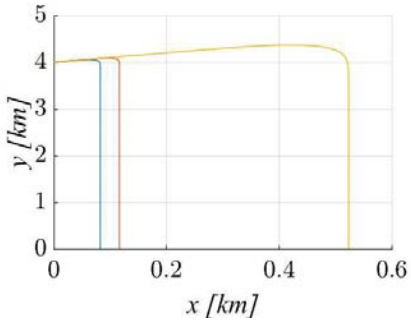

(d) $h_{exp} = 4\ km$

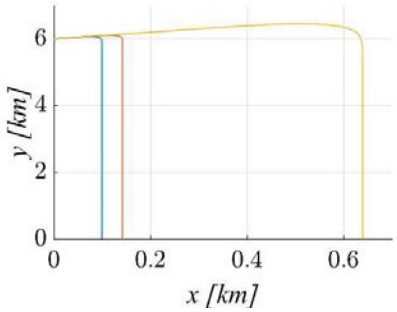

(e) $h_{exp} = 6\ km$

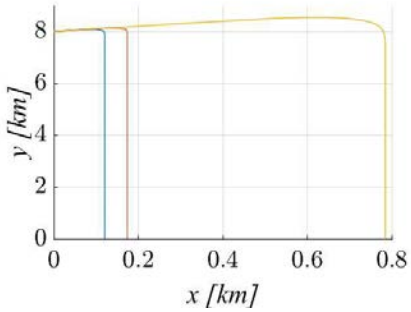

(f) $h_{exp} = 8\ km$

Figure 5.14. *Tank fragments trajectories after the explosion at different heights,* h_{exp}.

5.3.2.2 Other Fragments

The velocities of the fragments from parts adjacent to the tank can be determined through the overpressure value caused by the HTP detonation. The blastwave creates and accelerates the debris, and their velocity depends on the peak overpressure and the duration of the positive phase of the wave. Both can be evaluated using the Sadovsky formulas shown in equations 5.15

$$\Delta p_{air} = 0.84\ \frac{\sqrt[3]{k_t m_{exp}}}{r} + 2.7\ \frac{\sqrt[3]{(k_t m_{exp})^2}}{r^2} + 7\ \frac{k_t m_{exp}}{r^3}$$

$$\tau^+ = 1.3\ \sqrt[6]{k_t m_{exp}}\ \sqrt{r} \cdot 10^{-3} \tag{5.15}$$

where:

- Δp_{air} is the overpressure caused by an explosion in open air;
- τ^+ is the positive phase duration of the blastwave;
- r is the distance from the origin point in meters;
- m_{exp} is the explosives mass in kilograms;
- k_t is a parameter such as the product $k_t m_{exp}$ is the TNT equivalent mass.

Bearing in mind the possible sources of debris, the catalytic fragments are chosen to analyze the debris trajectory. This because the catalytic is close to the tank and, thus, the blastwave intensity is still high when it strikes it. Moreover, the catalytic is made by metals with high density and so a small fragment struck by the blastwave could travel far due to its high inertia. Considering the catalytic has the source of the debris, the distance from the explosion origin point is 1.2 m.

The force of the blastwave on the debris depends on the cross-sectional area of the debris and the pressure profile over time. The highest value of the pressure is found instantaneously as the wave strikes the objects and then decreases rapidly. This is the positive pressure phase. After this first phase, there is a negative pressure phase, characterized by a pressure lower

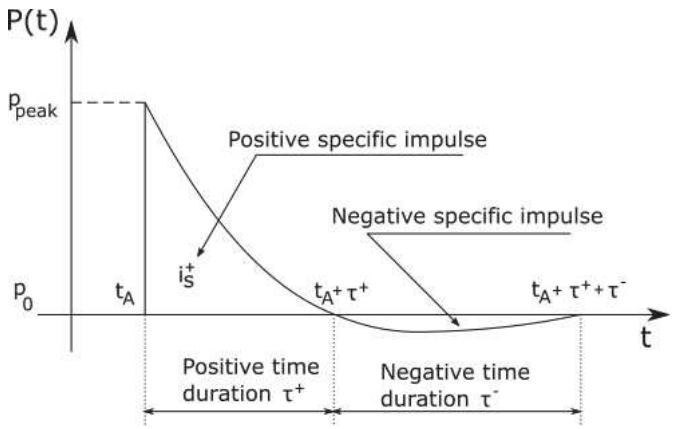

Figure 5.15. *Pressure profile due to a shock wave generated by a detonation.*

than the atmospheric value p_0, at the end of which the pressure slowly converges at p_0. This peculiar behaviour is shown in figure 5.15.

Taking into consideration only the positive phase, the impulse carried by the shock can be approximated with the area of the positive phase duration, which in turn can be approximated as a triangle having the peak pressure and the positive phase duration as legs

$$i_s^+ = \int_0^{\tau^+} \Delta p \, dt = \frac{\Delta p \cdot \tau^+}{2} \tag{5.16}$$

The velocity provided at the debris depends on the impulse, on the cross sectional area and on the mass of the debris.

$$v = i_s^+ \cdot \frac{A_f}{m} \tag{5.17}$$

The mass of the debris depends on its dimensions and density. Thus, the velocity of the debris can be expressed only in term of impulse, density and fragment height as follows

$$v = \frac{\Delta p \cdot \tau^+}{2} \frac{1}{\rho \, d} \tag{5.18}$$

If the catalytic is the source of the debris, a density of 8000 kg/m^3 can be used in the equation. The trajectories of two different cubic debris

Explosion height	*Blastwave* Δp $[atm]$	τ^+ $[ms]$	Velocity $v \cdot d$ $[m^2/s]$	d=0.1 m *Range* $[km]$	d=0.01 m *Range* $[km]$
0 km	274.5	2.82	4.90	0.677	0.228
2 km	221.6	2.72	3.82	0.780	0.541
4 km	168.6	2.59	2.77	0.834	0.491
6 km	114.8	2.42	1.76	0.823	0.355
8 km	60.0	2.15	8.17	0.621	81.7

Table 5.14. *Ranges for the debris generated by the catalytic with an explosion at different heights.*

are evaluated, the difference lies in the side dimension: one has a side of $d = 0.1\ m$ and the other of $d = 0.01\ m$.

The ranges of the two debris are listed in table 5.14. In the table are not reported the velocities of the different fragments but the product between the velocities and the debris side. Thus, the debris velocities can be obtained by this value by simply dividing it by the debris side. Since the sides have s dimension of 0.1 m and 0.01 m their velocity is one-tenth and one-percent of the values listed. The maximum range for both debris is in the case of an explosion at a height of 4 km. However, in all cases, the debris have a range lower than 1 km. The trajectories of the fragments after the explosion at different heights are shown in figure 5.16.

The catalytic fragment fall all within 1 km from the explosion point.

5.4 Failure and Response Modes

Several accidents could happen to the rocket while it is flying. Identifying the possible failure modes is important since different failure modes correspond to different response modes. The classification of the failure and response modes is fundamental to evaluate the possible consequences, which can range from having debris inside the scheduled impact region to the need for the Flight Termination System activation to avoid possible casualties or damages to buildings.

In table 5.15 are listed some of the major failure modes that the rocket could experience during flight. In the table are also listed the response modes and the possible consequences.

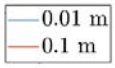

(a) Figure Legend

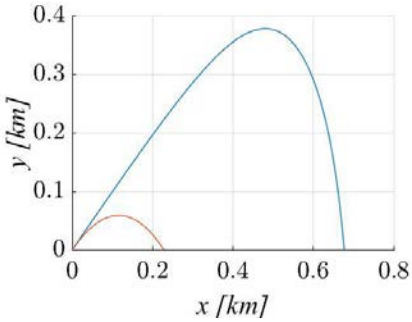

(b) $h_{exp} = 0\ km$

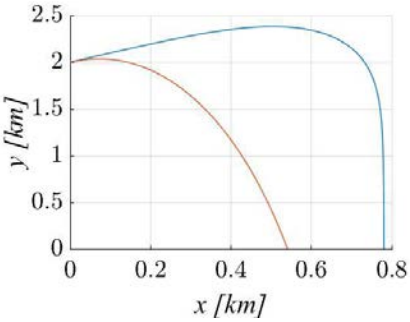

(c) $h_{exp} = 2\ km$

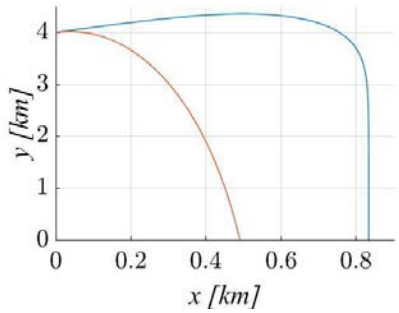

(d) $h_{exp} = 4\ km$

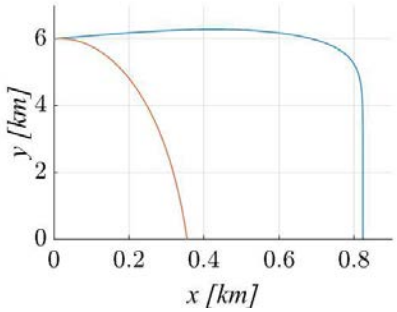

(e) $h_{exp} = 6\ km$

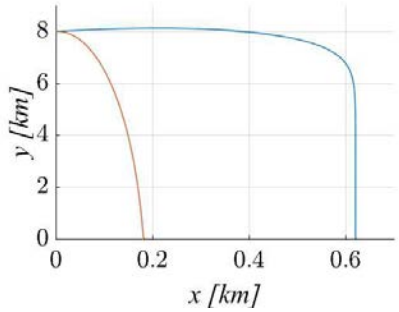

(f) $h_{exp} = 8\ km$

Figure 5.16. *Catalytic fragments trajectories after the explosion at different heights,* h_{exp}.

The failure modes listed can be divided into two main categories depending on whatever they pose or not a threat to public safety. Those failures which cause the rocket or some debris to fall inside the scheduled impact region are of no hazard to public safety. Those failures which bring the rocket off its nominal trajectory and outside the scheduled impact region must be further analyzed. In particular, these events are the premature parachute opening, the motor case burn-through, the nozzle-turn malfunction and the fin loss.

5.4.1 Loss of Thrust

If a malfunction in the main engine stops the combustion there is a loss of thrust. In this case, the rocket keeps flying on a ballistic trajectory with no major deviations and, thus, it should fall within the scheduled impact region with no threat to public safety.

5.4.2 Feeding Line Malfunction

A malfunction in the feeding line can have two main outcomes: it can interrupt the injection of the hydrogen peroxide in the main engine and so stop the combustion, or it can create an overpressure in either the engine or the tank causing an explosion. If the oxidizer flow is stopped, then the rocket experiences an on-trajectory loss of thrust and the rocket should fall within the schedule impact region. With an explosion, several debris can be generated but these should fall within the scheduled impact region. In both cases, there are no hazards for public safety.

5.4.3 Structural Failure

During its entire flight, the rocket should be able to withstand all loads. However, if the loads exceed the structural limits, the rocket could break. The structure can fail due to the failure of the junctions or for buckling due to the vibration and aerodynamic loads. In all cases, the rocket should break and the debris so generated should fall within the scheduled impact region, with no threat to public safety.

Failure Modes	*Response Modes*	*Consequences*
Loss of Thrust	On-Trajectory thrust loss	Rocket impact inside scheduled impact region
Structural Failure	On-Trajectory break-up	Debris inside scheduled impact region
Inertial Masses Loss	-	Debris inside scheduled impact region
Parachute Failure	-	Rocket destruction on impact
Feeding Line Malfunction	On-Trajectory thrust loss	Rocket impact inside scheduled impact region
	On-trajectory explosion	Debris inside scheduled impact region
Premature Parachute Opening	On-Trajectory break-up	Debris inside scheduled impact region
	Off-Trajectory turn	FTS activation
Motor Case Burn-Through	On-Trajectory thrust loss	Rocket impact inside scheduled impact region
	Off-Trajectory turn	FTS activation
Nozzle-Turn Malfunction	On-Trajectory break-up	Debris inside scheduled impact region
	Off-Trajectory turn	FTS activation
Fin Loss	On-Trajectory break-up	Debris inside scheduled impact region
	Off-Trajectory turn	Rocket impact outside scheduled impact region

Table 5.15. *Rocket failure and response modes.*

5.4.4 Loss of Inertial Masses

Even if the rocket's main structure can withstand all of the applied loads without breaking, some of its components may not. These can come from different sections of the rocket. The different nature of these parts can lead to different consequences. It is crucial to divide those parts whose loss could influence the rocket aerodynamic and those whose influence on the aerodynamic is negligible. Among the first are included the parachutes and the fins, while in the latter there are small parts as electric cables, screws, parts of the hatches, etc. Thus, three failure modes are analyzed separately: the loss of the parachute; the fin loss; the loss of inertial masses.

In the event of inertial mass loss, the rocket should continue in its flight but there could be debris inside the scheduled impact region without threat to public safety.

5.4.5 Parachute Failure

The parachute opening system should start the opening sequence after the rocket apogee passage. However, if a failure in the system occurs, the rocket will not slow down during its descent and it will impact the ground at high velocities. Thus, the rocket will complete its flight impacting the ground inside the scheduled impact region, but due to the high velocity, it will be destroyed. A parachute failure will pose no threat to public safety.

5.4.6 Premature Parachute Opening

The parachute could open prematurely during flight. This can happen for a malfunction in the opening system or due to the loss of the panel which closes the recovery bay. The premature opening can occur at high or low velocity with different consequences.

If the rocket is flying at high speed when the parachute opens, the induced loads should break either the main structure of the rocket or the shock cord that connects it to the parachute. If the main structure breaks, the debris generated should fall within the scheduled impact region. Instead, if the loads break the shock cord, the rocket continues in its flight but impacts the ground at high velocity and thus it will be destroyed at the

impact, which happens inside the scheduled impact region. A premature parachute opening at high speed poses no threat to public safety.

If the parachute opens at low velocities, the induced loads should not be high and neither the structure nor the shock cord should break. In this case, the parachute can act as an anchor, slowing down the rocket and forcing it to turn off its nominal trajectory. In this event, the FTS should be activated to prevent the rocket from causing any casualties or damages.

5.4.7 Motor Case Burn-Through

If there are problems in the main engine, the high temperature involved in the combustion could damage the external case and cause a motor case burn-through. This accident can lead to two main possible outcomes: an on-trajectory loss of thrust or an off-trajectory turn.

The motor case burn-through can change the conditions in the combustion chamber. Sudden changes in the combustion parameters can cause the combustion to stop. Therefore, there is a loss of thrust. As a consequence the rocket keeps flying on a ballistic trajectory and, thus, it should fall within the scheduled impact region with no threat to public safety.

It is possible that the combustion continues even after the motor case is damaged. In this case to the thrust through the nozzle must be added the component of thrust deriving from the motor case burn-through. The rocket should experience an off-trajectory turn and the FTS should be activated in order to prevent the rocket from causing any casualties or damages.

5.4.8 Nozzle-Turn Malfunction

Instability in the combustion chamber or malfunction in the nozzle could lead to a nozzle-turn malfunction. In this event, the thrust developed by the nozzle could experience an increase in the angle between its direction and the rocket axis. The main possible outcomes are an off-trajectory turn and an on trajectory break-up.

The sudden change in the thrust direction could create high loads on the main structure, breaking it. In this case, several debris could be generated. However, they should fall within the scheduled impact region without threat to public safety.

If the rocket resists the loads induced by the nozzle-turn, it could experience an off-trajectory turn. In this situation, the FTS should be activated to prevent the rocket from causing any casualties or damages.

5.4.9 Fin Loss

The fins are designed to resist the loads experienced during flight. However, in the case of unexpected loads or manufacturing errors, the rocket could lose one or more of its fins during flight. If this happens, the rocket should become unstable and the outcomes could be different depending mostly on the time of the event, or to be more precise, on the rocket velocity when it loses the fins.

If the rocket loses its fins at high velocity, the tumbling due to its unstable flight should give birth to high aerodynamic loads which should break the structure. Thus, there should be an on-trajectory break-up without threats to public safety.

If the rocket loses its fins at low velocity, the aerodynamic loads should have lower values and the rocket should withstand them. Thus, the rocket will continue its flight. However, due to its tumbling, it should experience an off-trajectory turn. In this case, the FTS should be activated in order to prevent the rocket from causing any casualties or damages.

Since the fin loss is principally caused by the aerodynamic loads on them, it is possible to infer how this accident is more likely to happen when the rocket velocity is higher. If the fin is lost at high velocity, the rocket is far off the launch site and it should break-up due to the aerodynamic loads without the need for the Flight Termination System. However, in the improbable possibility of the rocket remaining intact, the FTS could be activated to prevent the rocket from impacting outside the scheduled impact region. It is highly improbable to have a fin loss at low velocity, which means close to the launch site. In this improbable possibility, the FTS should be activated to reduce the distance travelled by the rocket avoiding any casualties or damages.

5.5 Flight Termination System

For safety reasons, a destructive Flight Termination System is installed on the rocket with the main purpose of avoiding the rocket, or any of its parts, to reach areas where they could cause any casualties or exit the safe zone. The FTS should be activated both in the event of an accident, like a nozzle-turn malfunction, and in the case in which the rocket, without any accident, follows a trajectory that brings it outside the safe zone. The FTS is located near the bottom of the oxidizer tank, in the liquid interstage as represented in figure 5.17.

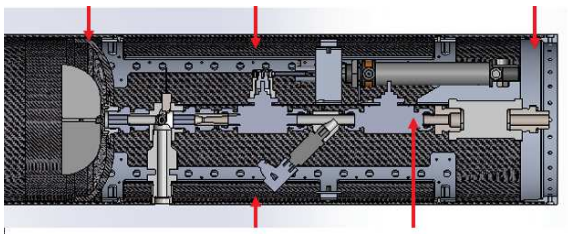

Figure 5.17. *Flight Termination System position in the rocket.*

On activation, it should break the rocket into two main parts, breaking the tank lower end-closure and releasing the HTP still stored in it before hitting the ground. Another consequence of the explosion is the cutting of the feeding line and, thus, the shutting-off of the main engine. With the FTS activation, the rocket will break into two main parts but also several smaller debris could be generated. These could consist of some part of the fluidic line, i.e. smaller pieces or valves which fall off with the explosion, or pieces of the tank, like the end-closure or small fragments of the main structure. The two main parts of the rocket after the FTS activation are show in figure 5.18 and they are:

- *Upper Part*: consisting of the nosecone, the recovery bay, the pressurizing line and the tank;

- *Lower Part*: consisting of the liquid line, the catalytic, the main engine and the fins.

Figure 5.18. *Upper and Lower parts of the rocket after the FTS activation.*

There are two main scenarios in which the FTS should be activated:

- *Launch behind launch site*;
- *Nozzle-turn malfunction.*

The scenario with the FTS activation after a nozzle-turn malfunction is used to model two other major accidents whose effects can be modelled in the same way: a motor case burn-through that produces a significant torque and the parachute premature parachute opening again in case it produces a torque.

5.5.1 Flight Termination System Description

The Flight Termination System consists of two independent systems, each one including a battery, an electric actuator and an explosive device, its scheme is shown in figure 5.19. The FTS system is composed of:

- 2 Antennas, each covering half sphere, thus, to ensure a complete coverage the antennas must be placed on opposite sides of the rocket;
- 1 Mixer and 1 Splitter to send signals to both Flight Termination Receivers;
- 2 Flight Termination Receivers;
- 2 Flight Termination Controllers;

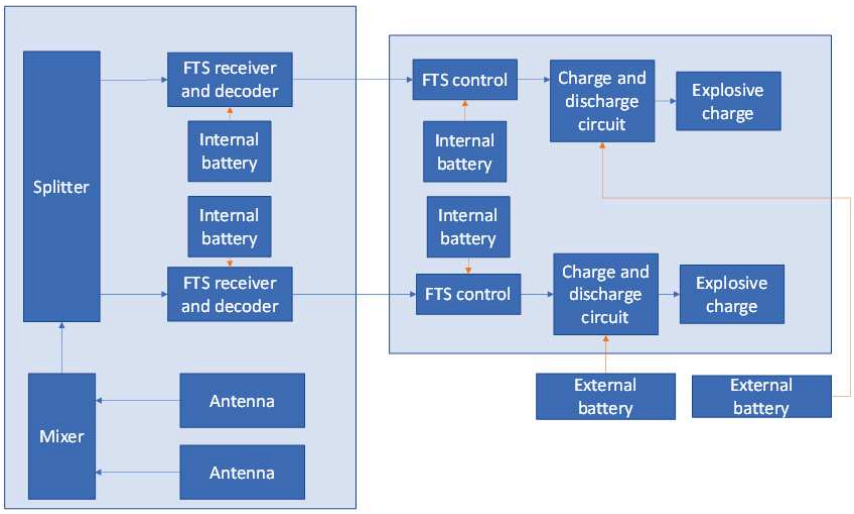

Figure 5.19. *Flight Termination System schematic.*

- 2 Explosive charges.

The probability of failure has been calculated considering an exponential distribution with MTBF of the flight termination as constant, i.e. time-independent, and the operation time of 1 hour, considering from power-on to splash-down.

$$p = 1 - e^{-\frac{time}{MTBF}} \tag{5.19}$$

The overall probability of failure must be evaluated considering the series of the different parts and the parallelism between the two systems. The probability of failure for parts in series is the sum of each item failure probability because if one part fails the entire series fails. For the parallel configuration, a failure occurs only if both FTR fail. The failure probability is squared to consider the failure of the two independent systems because the two devices are separated.

In view of the above considerations, the failure probability of the entire Flight Termination System can be fairly estimated to be below 10^{-3}.

5.5.2 FTS Activation Time

In the event of an accident, the Flight Termination System is not activated instantaneously, but there is an activation time related to the human re-

sponse time which depends on the moment and on the condition of flight. Considering different situations during flight, there are two scenarios associated with two activation time:

- Green code: 3 seconds activation time;
- Orange code: 1 second activation time;

The green code describes situations in which the rocket is flying on a nominal trajectory. In this case, if an accident occurs, the FTS is activated with a maximum time delay of 3 seconds. The orange code describes situations in which the rocket is flying deviating from its nominal trajectory, for example moving laterally instead or forward or climbing with a climbing angle too steep. In this case, the time delay is cut down to 1 second because the operator who has to activate the FTS is already in pre-alarm and, thus, has a shorter reaction time. At lift-off, the situation is by default an orange code. This because if an accident occurs shortly after launch, it is important to cut down the activation time and thus to prevent the rocket from reaching any areas where it could cause casualties. After lift-off, the code shifts from orange to green as the flight path angle of the rocket decreases. This because on a nominal trajectory the flight path angle always decreases with time. If the flight path angle should increase, then the rocket is on a non-nominal trajectory and it is important to maintain the pre-alarm state, i.e. the orange code. In figure 5.20 are shown the attitude and flight path angles of the rocket of some nominal trajectories for the first 15 seconds of flight.

On nominal trajectories the angles γ and β can have a slight increase in the first seconds after launch due to the wind effects. However, after a couple of seconds, they start to decrease. If there is an increase in either of them, the trajectory is classified as non-nominal. Thus, it is possible to justify an orange code if γ starts to increase a few seconds after lift-off.

Taking into account the performed simulations whose impact points are behind the launch site, it is possible to determine the time taken by the flight path angle to cross the 90° vertical. These times correspond to the moments in which the rocket starts to move backward. Their values are listed in table 5.16. In all cases, the rocket needs more than 3 seconds after lift-off to cross the 90°.

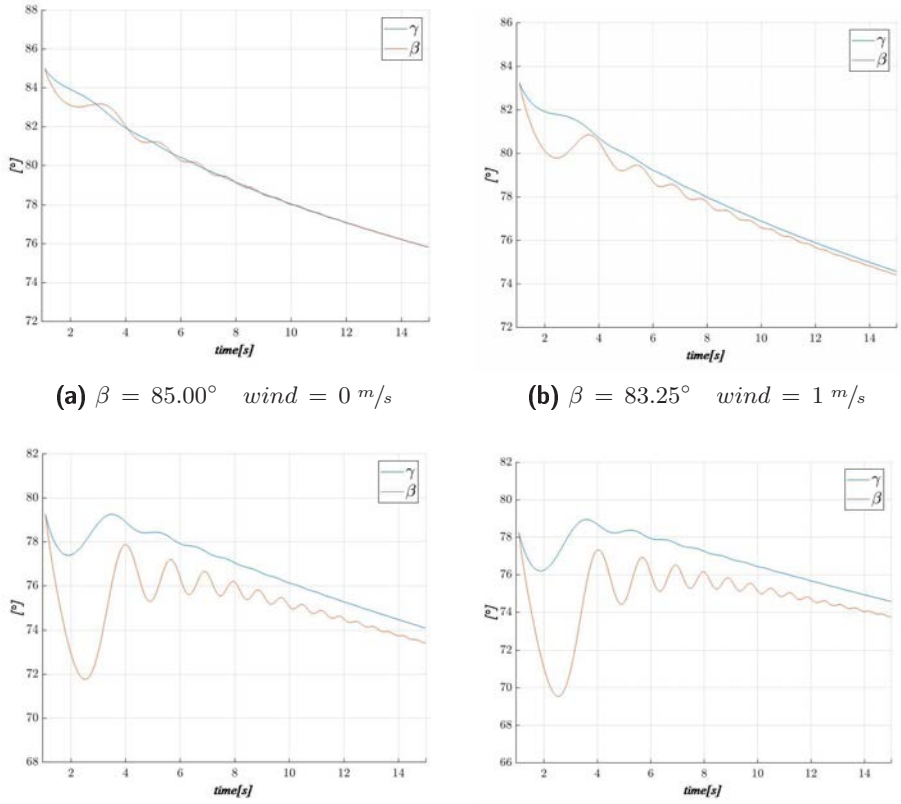

(a) $\beta = 85.00°$ $wind = 0\ ^m/_s$ **(b)** $\beta = 83.25°$ $wind = 1\ ^m/_s$

(c) $\beta = 79.25°$ $wind = 4\ ^m/_s$ **(d)** $\beta = 78.25°$ $wind = 5\ ^m/_s$

Figure 5.20. *γ and β angles for the first 15 seconds after launch for nominal trajectories.*

Elevation	*Impact Point*		*Slant Range*	90° *crossing*
β [°]	x [km]	z [km]	[km]	time [s]
84.78	-0.26	-1.04	1.07	11.9
85.16	-1.14	-2.57	2.82	5.1
85.15	-1.00	10.57	10.62	5.2
80.75	-0.02	-2.43	2.43	23.1
80.74	-1.12	-11.57	11.62	12.1
80.70	-2.34	18.80	18.95	7.0
79.24	-0.64	-17.52	17.54	19.9
78.50	-0.69	13.10	13.12	14.6
78.46	-0.92	1.66	1.89	14.4
78.37	-0.79	6.96	7.02	23.6
78.36	-0.10	0.25	0.25	23.1

Table 5.16. *Impact behind the launch site with* 90° *time crossing.*

The Flight Termination System should be activated only in the first 30 seconds of flight, i.e. during the thrusted flight. After burn-out, there are no possibilities to have a nozzle-turn or a motor case burn-through. There could be a parachute premature opening or a fin loss, and, in the latter, the FTS activation is not required even during thrusted flight. The parachute premature opening will simply slow down the rocket before it reaches the apogee, and it should not act as an anchor as in the thrusted flight. Thus, there will be no need for FTS activation.

5.5.3 Rocket Break-up after FTS Activation

After the Flight Termination System is activated, the rocket is divided into two main parts and several smaller debris. The two main part of the rocket after the FTS activation are:

- *Upper Part*: consisting of the nosecone, the recovery bay, the pressurizing line and the tank;
- *Lower Part*: consisting of the liquid line, the catalytic, the main engine and the fins.

The two parts have different aerodynamic characteristics. The Upper part has a low drag coefficient, but the absence of fins gives stability problems

due to the relative location of the centre of pressure and the centre of gravity. Thus, the part is unstable and after the explosion, it tumbles. The Lower part has a stable flight due to the fins, allowing this part to travel a ballistic trajectory, but having no nosecone it has a high drag coefficient. After the FTS activation, the trajectories of the two parts are simulated using a ballistic trajectory with the add of the drag effects.

The Upper part has an unstable flight and, thus, it is hard to determine its drag coefficient instant per instant. Therefore, the drag coefficient is assumed to be constant during the entire time. The value used in the simulations is the coefficient the part has on a stable flight, which is the lowest possible value the part can experience during its tumbling motion.

The Lower part has a high drag coefficient due to its geometry. After the FTS activation, there could be parts of the fluidic line or of the main structure which protrude and so increase the drag. The drag of this part is set to be equal to the drag of a cylinder, ignoring the contribution of the fins and other protruding parts. Another ignored characteristic which could cause an increase in the drag is the fact that not only there is no nosecone, but its frontal area is not closed. Thus, the drag coefficient of the Lower part in the simulation is lower than it should be in reality.

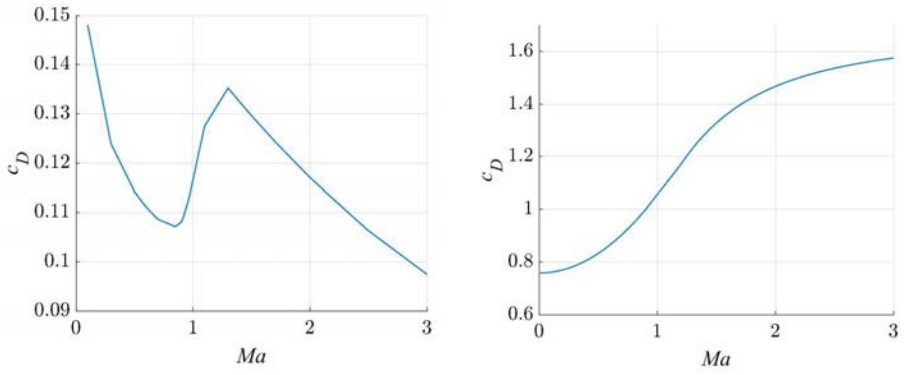

(a) Upper Part **(b)** Lower Part

Figure 5.21. *Drag coefficient of the Upper and Lower part of the Rocket after the FTS activation.*

The drag coefficients of the Upper and Lower part of the rocket after the FTS activation are shown in figure 5.21 in relation with the Mach number and an example of their trajectory is reported in figure 5.22. It is possible

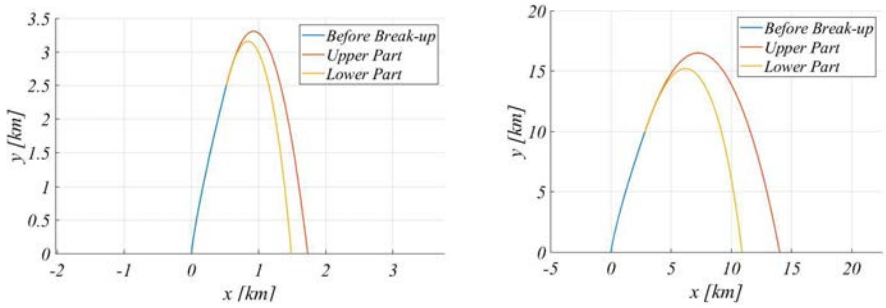

(a) 15 seconds FTS activation **(b)** 30 seconds FTS activation

Figure 5.22. *Trajectory of the Upper and Lower parts of the rocket after the FTS activation on a* 85.00° *nominal trajectory.*

to see the effects of the different drag coefficients in figure 5.22. The Lower part, having a higher drag travels a shorter distance and the difference between the Upper and Lower parts impact points is $\approx 0.3\ km$ and $\approx 3.5\ km$ respectively if the FTS is activated 15 or 30 seconds after lift-off.

For the Upper part, the drag coefficient used in the trajectory evaluation is the lowest value the part can experience during its flight due to the tumbling motion. The impact point of the part is the farthest distance it can reach and probably it will fall within a much shorter distance. The Lower part has a drag coefficient lower than in reality, but due to the simplicity of the ballistic trajectory simulation, it could fall on the ground close to the impact point but slightly farther off.

5.6 Analysis of Situations of Possible Land Impact

There are three main categories of events in which the rocket could impact the ground on land instead that at sea:

- Launch behind launch site;
- Nozzle-turn malfunction;
- Fin loss.

In the first two situations, the FTS should be activated. In the latter, it should not be necessary, but it could help in particularly if the fin is lost

near the launch site. In all three cases, the location of the impact must be evaluated to ensure it is not more than 3 kilometres behind the launch site.

5.6.1 Flight Termination on Launch behind Launch Site

Some of the launches simulated during the Monte Carlo fall behind the launch site. In these cases, the FTS should be activated to avoid the rocket from falling too far behind. The impacts points are shown on the map in figure 5.23 and their coordinates and slant ranges are listed in table 5.17.

In all cases even if the rocket falls behind the launch site, it never falls behind the $-3\ km$ requirement. However, the slant range of some of the trajectories is well above $3\ km$. In order to avoid any possible damage even far from the launch site, it is possible to activate the FTS, shut-off the main engine and break the rocket.

During these flights, no accident occurs and there are no sudden changes in the trajectory. The rocket slowly shifts its trajectory until it begins to move backwards. It is then possible to see these eventualities well before the rocket moves behind the launch site. As previously shown in table 5.16, the rocket starts to move backwards after more than $3\,seconds$ from lift-off. Activation times of 1 and $3\,seconds$ are used to evaluate where the rocket parts could end. However, since the change in trajectory is not instantaneous, also an activation time of $0\,second$ is considered. The activation time is taken from the moment in which the rocket flight path angle crosses the 90°, thus it is always more than $3\,seconds$ after lift-off. Considering the slow changes in the trajectory of these launches, the $0\,second$ activation time is the most probable.

The slant ranges of all different launches for all different activation times are listed in 5.18. With the 0 and $1\,second$ time delay, none of the parts of the rocket falls behind the launch site. However, with a $3\,seconds$ delay some of the launches fall behind the launch site, but the impacts are within 100 meters from the launch site. In all cases and for all activation times the slant range is lower than 3 kilometres. With a $0\,second$ activation time, the impacts are closer to the launch site, but even with a $3\,seconds$ activation time all parts are inside the $3\ km$ range. In figure 5.24 are shown the impacts points of both parts for the different activation times.

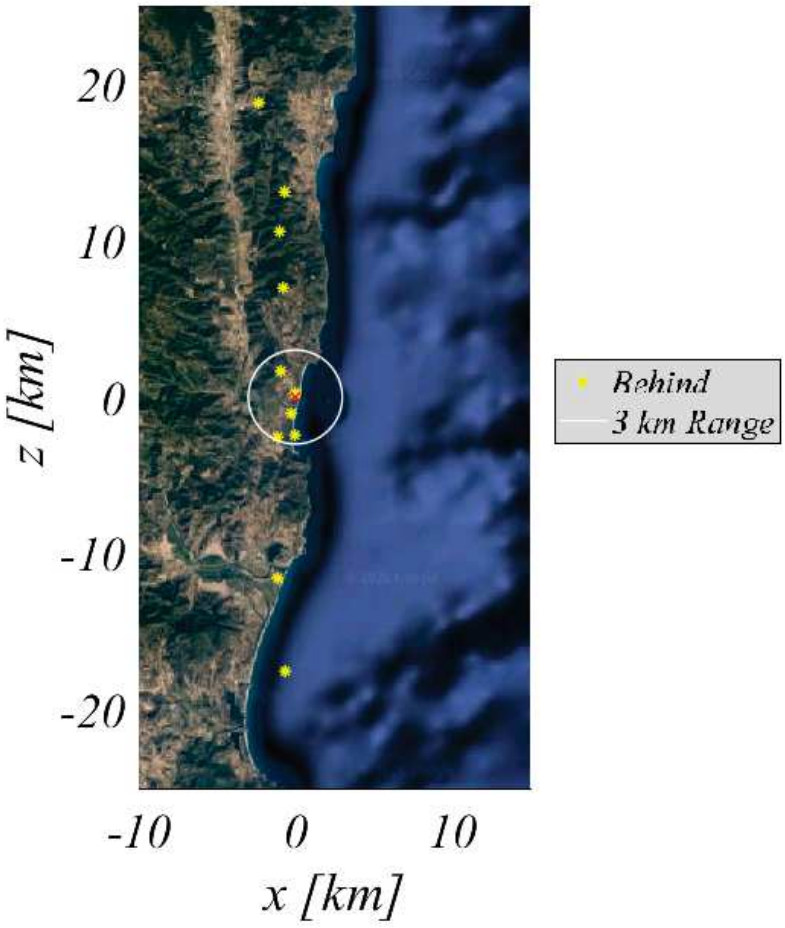

Figure 5.23. *Impact Points behind launch site of the Monte Carlo.*

Elevation	*Impact Point*		*Slant Range*
β [°]	x [km]	z [km]	[km]
85.16	-1.14	-2.57	2.82
85.15	-1.00	10.57	10.62
84.78	-0.26	-1.04	1.07
80.75	-0.02	-2.43	2.43
80.74	-1.12	-11.57	11.62
80.70	-2.34	18.80	18.95
79.24	-0.64	-17.52	17.54
78.50	-0.69	13.10	13.12
78.46	-0.92	1.65	1.89
78.37	-0.79	6.98	7.02
78.36	-0.01	0.25	0.25

Table 5.17. *Impact point of Monte Carlo launches behind launch site.*

β [°]	no FTS [km] Slant Range	3 s FTS [km] Upper	3 s FTS [km] Lower	1 s FTS [km] Upper	1 s FTS [km] Lower	0 s FTS [km] Upper	0 s FTS [km] Lower
85.16	2.82	0.18	0.16	0.01	0.01	0.01	0.01
85.15	10.62	0.12	0.11	0.05	0.05	0.03	0.03
84.78	1.07	0.12	0.10	0.08	0.07	0.07	0.06
80.75	2.43	0.74	0.56	0.58	0.59	0.53	0.42
80.74	11.62	0.65	0.56	0.45	0.39	0.36	0.32
80.70	18.95	0.37	0.34	0.21	0.19	0.15	0.14
79.24	17.54	2.99	2.36	2.29	1.86	1.99	1.64
78.50	13.12	1.31	1.10	0.96	0.82	0.80	0.70
78.46	1.89	0.11	0.12	0.10	0.11	0.09	0.10
78.37	7.02	2.37	1.73	1.83	1.39	1.61	1.25
78.36	0.25	0.25	0.26	0.23	0.25	0.22	0.24

Table 5.18. *Slant ranges of the Upper and Lower part of the rocket after the FTS activation with different activation time.*

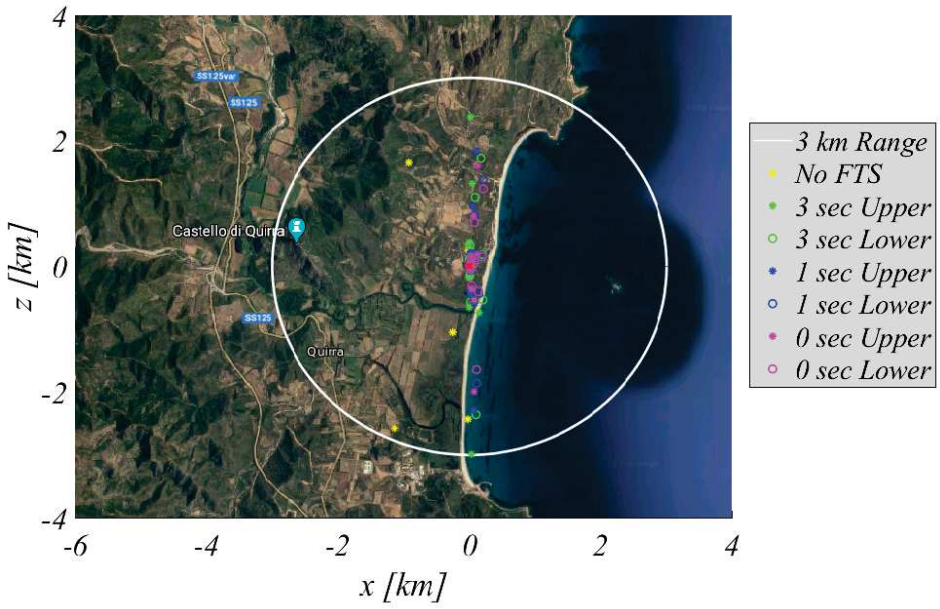

Figure 5.24. *Impact points of the parts of the rocket with the different activation times.*

5.6.2 Nozzle-Turn Malfunction

The rocket could deviate from its nominal trajectory due to a nozzle-turn malfunction. In this event, damages to the nozzle can cause the thrust misalignment angle to increase. Two other major accidents whose effects can be modelled in the same way are the motor case burn-through and the parachute premature opening. In the motor case burn-through, the composite case of the combustion chamber burns and crack and holes are formed in it. In this case, the nozzle has no damage, but the thrust produced by the holes in the combustion chamber must be added to the nominal axial thrust. Thus, there is a total thrust whose vector has a misalignment angle major than in the nominal case [32]. A premature parachute opening has effects on the rocket which could be modelled as a nozzle-turn since the parachute acts as an anchor and forces the rocket to turn from its trajectory increasing the angle between the velocity and the rocket.

To simulate the effects of a nozzle-turn malfunction, at fixed times during the rocket trajectory the thrust misalignment is modified. A misalignment thrust angle of 15° is considered for the nozzle-turn. This is a very high and improbable value. Nevertheless, it has been chosen to have a higher safety margin. Two sets of simulations are performed: a set with the rocket on a nominal trajectory and a set on a non-nominal trajectory.

An important difference between the nominal and non-nominal trajectories is the FTS activation time: in the first is set to $1\,seconds$ while in the latter is $3\,seconds$. On a non-nominal trajectory, the activation time is shorter since it is an orange code situation, in this case, the rocket is climbing almost vertically from the launch site. After the FTS activation, the ballistic trajectories of the two main parts of the rocket, the Upper part and the Lower part, are evaluated.

In the event of a nozzle-turn malfunction, the damages to the nozzle will preclude from having a full nominal thrust since there will be no ideal expansions of the exhausted gases. With a motor case burn-through, the hot gases exiting directly from the holes and cracks in the combustion chamber don't undergo an expansion process. Thus, these gases do not produce a significant thrust. Moreover, the exiting of the hot gases from the combustion chamber causes a reduction in the thrust produced by the nozzle. In both

cases, considering the total nominal thrust to keep acting even after the nozzle-turn malfunction or motor case burn-through means adding a safety margin to the simulations. Another safety margin added to these analyses is the direction in which the thrust misalignment acts, which forces the rocket to move backward. This is the worst-case scenario while in reality it could be forced to move in any direction, lowering the possibility of the rocket falling behind the launch site.

In the case of a nozzle-turn malfunction, or any other accident whose effects can be simulated in the same way, considering a 15° change in the thrust misalignment angle and the full thrust to keep acting after the accident will produce an overestimation of the change in directions and velocities of the rocket fragments. Moreover, considering how the Upper part while tumbling has a higher drag coefficient than the one used, it is possible to infer it should travel a shorter distance than in the simulations.

5.6.2.1 Nozzle-turn on Nominal Trajectory

In the case of a nominal trajectory, the FTS activation time is of 3 seconds, the situation is a green code. The possible effects of the nozzle-turn are evaluated for three of the $\beta-wind$ pairs used in the Monte Carlo, specifically they are 85.00° $0\,m/s$, 83.25° $1\,m/s$ and 78.25° $5\,m/s$. The nozzle-turn is set to happen at fixed times during the rocket flight. The impact points for the Upper and Lower parts of the rocket after the FTS activation in case of a nozzle-turn malfunction on a nominal trajectory are listed in table 5.19. In all cases analyzed, both parts of the rocket fall forward the launch site.

Nozzle-turn time [s]	85° Impact [km]		83.25° Impact [km]		78.25° Impact [km]	
	Upper	Lower	Upper	Lower	Upper	Lower
5	0.09	0.09	0.11	0.11	0.15	0.15
10	0.27	0.27	0.36	0.35	0.42	0.42
15	2.24	1.88	2.48	2.10	2.65	2.16
20	1.09	1.14	1.57	1.53	1.54	1.59
25	5.55	4.57	6.16	4.94	6.09	4.50

Table 5.19. *Impact points of nozzle-turn malfunction on nominal trajectories with 3 seconds activation time.*

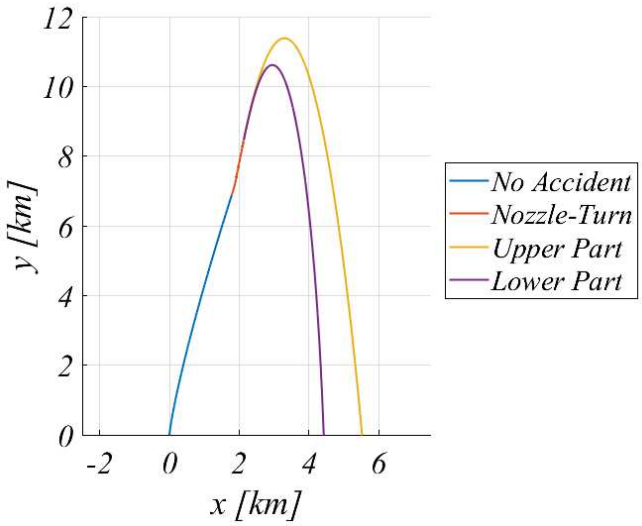

Figure 5.25. *Trajectories of the Upper and Lower parts of the Rocket after a Nozzle-turn malfunction at t=25 s and the FTS activation with a 3 seconds delay on a* 85.00° *nominal trajectory.*

An example of the trajectory of the two parts of the rocket after the FTS activation in case of a nozzle-turn malfunction on a nominal trajectory is reported in figure 5.25.

5.6.2.2 Nozzle-turn on Non-Nominal Traejectory

In the case of a non-nominal trajectory, the FTS activation time is of 1 second, the situation is an orange code. The possible effects of the nozzle-turn is evaluated for three of the $\beta - wind$ pairs used in the Monte Carlo, specifically they are 85.00° $0\,m/s$, 83.25° $1\,m/s$ and 78.25° $5\,m/s$. The nozzle-turn is set to happen at fixed times during the rocket flight. The impact points for the Upper and Lower parts of the rocket after the FTS activation in case of a nozzle-turn malfunction on a non-nominal trajectory are listed in table 5.20.

An example of the trajectory of the two parts of the rocket after the FTS activation in case of a nozzle-turn malfunction on a nominal trajectory is reported in figure 5.26.

In the case of a nozzle-turn malfunction on a non-nominal trajectory, the two parts of the rocket fall behind the launch site. However, they never fall behind the $-3\,km$ range imposed.

Accident time [s]	85° Impact [km] Upper	Lower	83.25° Impact [km] Upper	Lower	78.25° Impact [km] Upper	Lower
5	-0.04	-0.03	-0.03	-0.02	0.01	0.01
10	-0.23	-0.19	-0.20	-0.16	-0.14	-0.10
15	0.05	0.05	0.09	0.10	0.16	0.19
20	-0.74	-0.52	-0.67	-0.44	-0.58	-0.31
25	-2.18	-1.41	-2.08	-1.30	-2.05	-1.17

Table 5.20. *Impact points of nozzle-turn malfunction on non-nominal trajectories with* 1 *second activation time.*

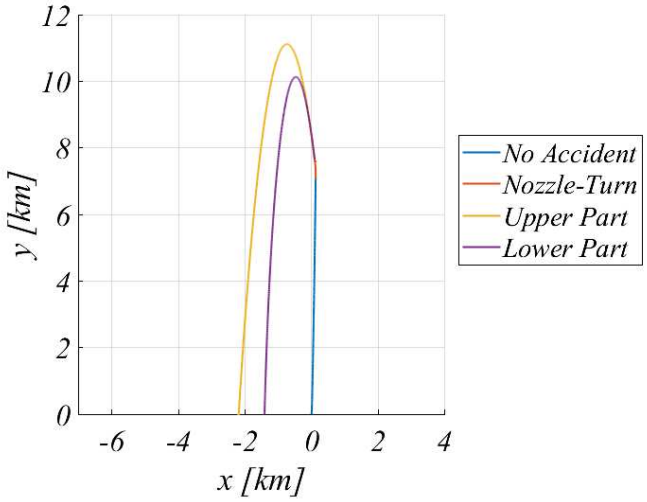

Figure 5.26. *Trajectories of the Upper and Lower parts of the Rocket after a Nozzle-turn malfunction at t=25 s and the FTS activation with a 1 seconds delay on a* 85.00° *non-nominal trajectory.*

5.6.3 Fin Loss

If the loads on the fins exceed their structural limits, one or more of the fins could be lost. In this case, the rocket could become unstable and, therefore, start tumbling. During the tumbling motion, the velocity vector will turn and the rocket will slow down. Considering all the nominal values for the elevation angle and wind levels of the Monte Carlo, the consequences of the fin loss are evaluated at fixed time intervals.

Before evaluating the impact points in case of fin loss, the shift in the velocity vector must be analyzed. Taking into consideration the time intervals needed for the rocket to rotate of about 180°, the velocity vector

rotation ranges between 5° and 15°. The highest values of the rotation are found for the lower times in which the fin is lost.

For the evaluation of the impact points after the fin loss, the accident happens at fixed times, then its velocity vector is tilted and then its motion is simulated as a ballistic flight. The velocity of the rocket after the fin loss and, thus, after the velocity tilt is set to be equal to the velocity before the accident. This is a safety margin because, during the tumbling, the rocket will slow down decreasing its velocity. The rocket should never fall more than 3 kilometres behind the launch site even in the event of a fin loss.

5.6.3.1 Rocket Behaviour after Fin Loss

The rocket behaviour is different and depends if one or more fins are lost. This because the aerodynamic characteristics of the flight, in particular the relative location of the centre of pressure and the centre of gravity, depends on the number of fins lost.

As a first step, the position of the centre of pressure and lift coefficient of the rocket with and without fins are evaluated. Thus, it is possible to determine the fin contribution to the lift coefficient and so to determine the position of the centre of pressure if only one fin is lost.

$$c_{L_{fin}} = c_{L_{full}} - c_{L_{body}} \tag{5.20}$$

$$x_{cp_{1fin}} = \frac{x_{cp_{body}} \cdot c_{L_{body}} + 0.5 \cdot c_{L_{fin}} \cdot l_{fin}}{c_{L_{body}} + 0.5 \cdot c_{L_{fin}}} \tag{5.21}$$

where:

- $c_{L_{fin}}$ is the lift coefficient of two fins;
- $c_{L_{full}}$ is the lift coefficient of the entire rocket;
- $c_{L_{body}}$ is the lift coefficient of the rocket without fins;
- $x_{cp_{1fin}}$ is the centre of pressure of the rocket if it loses one fin;
- $x_{cp_{body}}$ is the centre of pressure of the rocket without fins;
- l_{fin} is the distance between the centre of pressure and the fin.

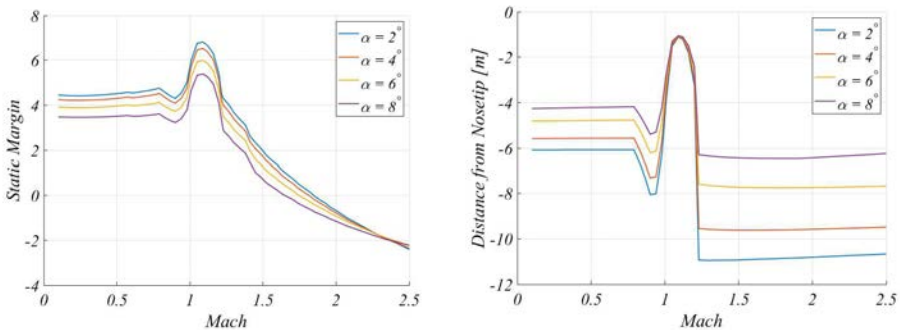

(a) Static margin without 1 fin **(b)** Static margin without fins

Figure 5.27. *Rocket static margin in case of 1 or more fins loss.*

From the position of the centre of pressure it is possible to evaluate the static margin of the rocket and, thus, to determine if it has or not a stable flight. The static margins in case of one or more fin loss are reported in figure 5.27. The static margin in case of more than one fin loss is always below zero. Thus, the rocket without fins is always unstable. If the rocket losses only one of its fins, then it could have a stable flight depending on the Mach number. The fins loss depends on the loads acting on them and it is more probable to occur when the velocities are high, so the rocket will become unstable even with only one fin loss.

After the fin loss, the rocket motion is simulated as a ballistic trajectory. The velocity vector is tilted by an angle between 5° and 15° starting from the direction it has before the fin loss. However, the real behaviour of the rocket is different. In particular, the rocket tumbles and the flight path angle γ starts to oscillate around a value that can be lower or higher with respect to the initial value depending on many flight conditions at the moment of the accident.

The flight path angle and the trajectory for the first 25 seconds of the rocket flying on a 90° trajectory with the fin loss 10 seconds after lift-off are reported in figures 5.28. In figure 5.29 is reported angle γ of a 85° trajectory with $5\,m/s$ and a fin loss 10 seconds after lift-off. The flight path angle after the loss of the fins oscillates. Initially, the value is higher than before the loss. However, the oscillations reduce the velocity and the flight path angle decreases quickly. Simulating the rocket on a ballistic trajectory

with an initial velocity equal to the velocity at the moment of the accident means introducing a safety margin because no decrease in the velocity is considered even if the rocket is tumbling.

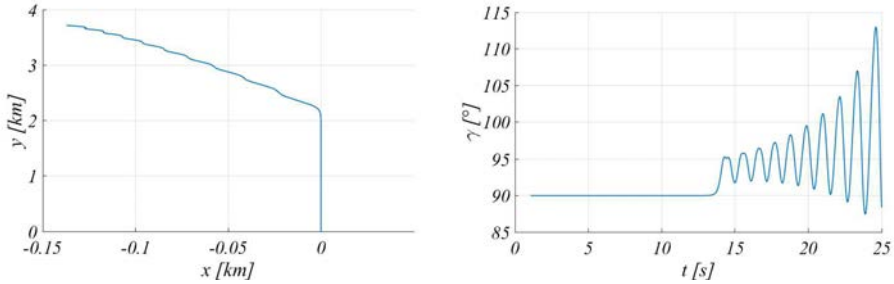

Figure 5.28. *Flight path angle and trajectory for the first 25 seconds of a trajectory with $\beta = 90°$ and no wind.*

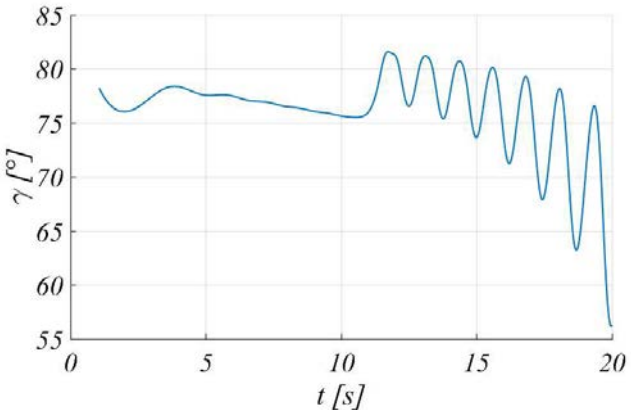

Figure 5.29. *Flight path angle for the first 20 seconds of a trajectory with $\beta = 78.25°$ and 5 $^{m}/_{s}$ wind.*

After the fin loss, the rocket tumbles and it could break due to the dynamic pressure, q. Considering that the rocket during the tumbling has a maximum attack angle of 90°, the products $\alpha \cdot q$ are evaluated for different accident time and are listed in table 5.21. The product has high values, especially if the fin is lost after more than 15 seconds after lift-off. Due to these high values, the rocket will probably break in the event of a fin loss at high speed.

The drag coefficient during ballistic flight is set to be equal to the drag coefficient of the rocket without fins with a 0° angle of attack. This means

Accident time [s]	$\alpha \cdot q$ $[^{(rad \cdot kg)}/_{(m \cdot s^2)}]$	
	Nominal	*Non-Nominal*
5	$1.16 \cdot 10^4$	$1.14 \cdot 10^4$
10	$4.58 \cdot 10^4$	$4.50 \cdot 10^4$
15	$9.31 \cdot 10^4$	$9.06 \cdot 10^4$
20	$1.33 \cdot 10^5$	$1.30 \cdot 10^5$
25	$1.63 \cdot 10^5$	$1.58 \cdot 10^5$

Table 5.21. *Value of the product $\alpha \cdot q$ for different fin loss time.*

that the c_D used is the lowest possible value the rocket could experience during its tumbling motion. As it tumbles, the drag coefficient will be higher and so the rocket velocity will decrease in a shorter time. Thus, the impact point found is much farther than the typical distance the rocket could reach.

5.6.3.2 Fin Loss on Nominal Trajectory

The impact points of the rocket in the event of a fin loss while the rocket is flying on a nominal trajectory are listed in table 5.22. For the nominal trajectories, a velocity tilt of 15° is considered for each time, even if for the higher times the rotation should be much lower.

Time [s]	85.00° *Fall [km]*	83.25° *Fall [km]*	82.00° *Fall [km]*
5	-0.20	-0.12	-0.07
10	-0.20	0.06	0.15
15	0.26	0.77	0.93
20	1.25	2.12	2.35
25	3.20	4.81	4.62

Time [s]	80.75° *Fall [km]*	79.25° *Fall [km]*	78.25° *Fall [km]*
5	-0.02	0.05	0.09
10	0.26	0.45	0.50
15	1.10	1.47	1.52
20	2.60	3.21	3.22
25	2.28	6.25	6.00

Table 5.22. *Impact points after fin loss on a nominal trajectory with a 15° tilt angle.*

The dynamic pressure during flight is high and it will probably cause the rocket to break-up as it tumbles after the fin loss. In none of the analyzed trajectories, the rocket falls more than 3 kilometres behind the launch site. Moreover, only in the improbable event of fin loss within the first 10 seconds, the rocket falls behind the launch site. In this case, the rocket falls within 200 metres without the need for the FTS activation.

5.6.3.3 Fin Loss on Non-Nominal Trajectory

The impact points of the rocket in the event of fin loss on non-nominal trajectory are listed in table 5.23. A first evaluation is made using a tilt of the velocity vector of 15° for each time.

Time [s]	85.00° *Fall [km]*	83.25° *Fall [km]*	82.00° *Fall [km]*
5	-0.48	-0.41	-0.36
10	-1.72	-1.59	-1.16
15	-2.72	-2.49	-2.38
20	-4.32	-3.93	-3.73
25	-7.72	-7.15	-6.92

Time [s]	80.75° *Fall [km]*	79.25° *Fall [km]*	78.25° *Fall [km]*
5	-0.13	-0.26	-0.22
10	-1.47	-1.34	-1.23
15	-2.40	-2.23	-2.07
20	-3.72	-3.39	-3.07
25	-7.02	-6.59	-6.11

Table 5.23. *Impact points after fin loss on a non-nominal trajectory with a* 15° *tilt angle.*

On the non-nominal trajectories, the rocket falls behind the $-3\,km$ limit if a fin is lost after the 20^{th} second of flight imposing a 15° tilt angle. The velocity rotation for non-nominal trajectory after more than 15 seconds after lift-off is lower than 5°. Thus, a too safety high margin has been taken and it is possible to evaluate the impact points of the rocket in the case of fin loss using a lower tilt angle for the higher times. Even if the tilt angle imposed on the velocity is 5°, it is still higher than the one the rocket should

Time [s]	85.00° Fall [km]	83.25° Fall [km]	82.00° Fall [km]
20	-1.39	-0.95	-0.74
25	-2.55	-1.88	-1.62

Time [s]	80.75° Fall [km]	79.25° Fall [km]	78.25° Fall [km]
20	-0.73	-0.39	-0.04
25	-1.67	-1.27	-0.75

Table 5.24. *Impact points after fin loss on a non-nominal trajectory with a 5° tilt angle.*

experience in reality, thus, maintaining a safety margin. In the table 5.24 are listed the impact points of the rocket with a velocity tilt angle of 5° if the fin loss happens 20 and 25 seconds after lift-off. A tilt angle of 5° for the velocity vector still brings the rocket to fall behind the launch site. However, it never moves more than 3 kilometres behind it.

Considering a rotation of 15° for the times up to 15 seconds and of 5° for the times above 15 seconds, the rocket in case of a fin loss on a non-nominal trajectory falls behind the launch site, but never falls behind the -3 kilometre line.

5.7 Failure Probability Tables

All the situations described in the above paragraphs can be summarized within failure probability tables and the different situations can then be divided into three main categories depending on the possible threat to public safety:

- *Low*: probability of the event to occur is below 10^{-6} or the rocket does not fall behind the launch site;
- *Medium* : probability of the event to occur is below $5 \cdot 10^{-4}$ and the rocket does not fall more than 3 km behind the launch site;
- *High*: probability of the event to occur is above $5 \cdot 10^{-4}$ or the probability of the event to occur is above 10^{-6} and the rocket falls more than 3 km behind the launch site.

In the tables, the situations with and without accidents, on nominal and non-nominal trajectories, with and without a failure of the Flight Termination System are analyzed separately.

The first situation to be analyzed is the trajectory without accidents. The trajectory probability is evaluated considering the 90% cumulative probability because it is higher than the most probable value evaluated from the Monte Carl outputs. The results are listed in tables 5.25 and 5.26. The possibility of the rocket falling behind the launch site with the FTS failure is below the imposed threshold. In the case of the FTS successful activation, different danger levels are present depending on the activation time delay. If the FTS is activated in the moment in which there is the passage between the orange code and the red code or 1 *second* later, the debris will fall on the sea. In case the delay of the activation is of 3 *seconds* or more, some debris could fall a few hundred meters behind. It is necessary to underline how, in the situations described in this tables, the orange code will last more than 3 *seconds* before becoming a red code. Thus, a further delay of another 3 *seconds* for the activation should not be plausible.

The total probability in case of an accident is the product of the probability of the trajectory (nominal or non-nominal), the probability that the accident is the one analyzed and the probability that the accident brings the rocket back the direction of the launch site. Based on literature data and engineering estimations, the probability of a rocket failure is below 10%[31]. For example, NASA sounding rocket program has a failure rate of 5%. By far the majority of rocket failures end with an on-trajectory break-up, a loss of performance or a slight trajectory deviation. The probability of a nominal trajectory is < 1 while that of a non-nominal trajectory is $< 10^{-2}$.

Analyzing the possibility of a nozzle-turn malfunction, this accident is divided into four particular cases: nominal trajectory and FTS success, nominal trajectory and FTS failure, non-nominal trajectory and FTS success, non-nominal trajectory and FTS failure. The probability that an accident is a nozzle-turn is below 10%. If the rocket is on its nominal path, the probability that the rocket will turn in the direction of the launch site with a significant angle is estimate to be below 5%. This assessment is fairly accurate because the majority of large turn malfunctions are related to the thrust vectoring, which is not present on the sounding rocket analysed. In

Event	*Probability*	*FTS Status*	*FTS Probability*	*|x|*	*Total Probability*	*Danger*
Behind Launch site	$< 5 \cdot 10^{-4}$	Failure	$< 10^{-3}$	$< 3\ km$	$< 5 \cdot 10^{-7}$	Low
Slant Range $> 3\ km$	$< 10^{-4}$	Failure	$< 10^{-3}$	$< 3\ km$	$< 10^{-7}$	Low

Table 5.25. *Failure probability table of Non-Nominal trajectory - FTS Failure.*

Event	*Probability*	*FTS Status*	*FTS Probability*	*|x|*	*Total Probability*	*Danger*
Behind Launch site	$< 5 \cdot 10^{-4}$	Works at event $+0\,s$	< 1	*Forward*	$< 5 \cdot 10^{-4}$	Low
Behind Launch site	$< 10^{-4}$	Works at event $+1\,s$	< 1	*Forward*	$< 5 \cdot 10^{-4}$	Low
Behind Launch site	$< 10^{-4}$	Works at event $+3\,s$	< 1	$< 0.1\ km$	$< 5 \cdot 10^{-4}$	Medium

Table 5.26. *Failure probability table of Non-Nominal trajectory - FTS Success.*

Trajectory	*Probability*	*Accident Probability*		*Threat*	*FTS*		*/x/*	*Total*	*Danger*
		General	*Specific*	*Level*	*Status*	*Probability*		*Probability*	
Nominal	< 1	$< 10^{-1}$	$< 10^{-1}$	$< 5 \cdot 10^{-2}$	Works	< 1	Forward	$< 5 \cdot 10^{-4}$	Low
Nominal	< 1	$< 10^{-1}$	$< 10^{-1}$	$< 5 \cdot 10^{-2}$	Fails	$< 10^{-3}$	N/A	$< 5 \cdot 10^{-7}$	Low
Non-Nominal	$< 10^{-2}$	$< 10^{-1}$	$< 10^{-1}$	< 1	Works	< 1	$< 3\ km$	$< 10^{-4}$	Medium
Non-Nominal	$< 10^{-2}$	$< 10^{-1}$	$< 10^{-1}$	< 1	Fails	$< 10^{-3}$	$< 3\ km$	$< 10^{-7}$	Low

Table 5.27. *Failure probability table in case of Nozzle-turn malfunction.*

Trajectory	*Probability*	*Accident Probability*		*Threat*	*/x/*	*Total*	*Danger*
		General	*Specific*	*Level*		*Probability*	
Nominal up to $10\,s$	< 1	$< 10^{-1}$	$< 10^{-2}$	$< 5 \cdot 10^{-1}$	$< 0.2\ km$	$< 5 \cdot 10^{-4}$	Medium
Nominal After $10\,s$	< 1	$< 10^{-1}$	$< 10^{-1}$	$< 5 \cdot 10^{-2}$	Forward	$< 5 \cdot 10^{-4}$	Low
Non-Nominal	$< 10^{-2}$	$< 10^{-1}$	$< 10^{-1}$	< 1	$< 3\ km$	$< 10^{-4}$	Medium

Table 5.28. *Failure probability table in case of Fin loss.*

a sounding rocket without thrust vector control, a nozzle failure is generally associated with a small angle deviation, a significant thrust loss or an explosion. The probabilities just described must be multiplied by the probability of the FTS success or failure. Thus, the possibility that the rocket falls behind the launch site is below the imposed threshold. The failure probabilities for the nozzle-turn are listed in table 5.27.

The last case to analyze is a fin loss. In this case, since the rocket tumbles, the use of the FTS is recommended but not essential. The fin loss is divided into three particular cases: nominal trajectory up to 10 *seconds*, nominal trajectory after 10 *seconds* and non-nominal trajectory. The probability that an accident is a fin loss is below 10% at high speeds. If the rocket is flying at high speed, then the probability that it turns in the direction of the launch site without breaking is estimated to be below 5%. The probability of a fin loss at low speed is considered to be less than the 10% of the probability of a fin loss, i.e. a 1%. This because at low speed the loads are small and two fins need to be lost to make the rocket unstable. The probability that the rocket will turn upward in the direction of the launch site is much less than 50%. Actuating the FTS, the rocket will fall in the sea, without actuation it could impact the ground a few hundred meters behind the launch pad. The failure probabilities for a fin loss are listed in table 5.28.

Concluding, following the proper procedure regarding the green, orange, and red codes based on the flight path angle or the axial velocity, the launch of the sounding rocket will respect the imposed safety constraints.

Conclusions

T4i - Technology for Propulsion and Innovation in collaboration with the University of Padua is developing a sounding rocket as a technology demonstrator for their hybrid engine. Before a launch campaign can start, it is fundamental to ensure the rocket is not a threat to public safety. Two main topics have been taken into consideration and developed in this thesis: the load analysis and the safety range analysis.

The load analysis is carried out to ensure the rocket can resist all of the applied loads throughout its life, from the handling and transportation, to the flight and recovery. The analysis focused on the loads acting on the sounding rocket during its flight phases. This choice derives from the fact that in these moments the applied loads are more severe and, thus, a structural failure is more likely to occur and it could be of concerns for public safety. The main structure reacts to the applied loads developing shear and axial forces and bending moments. These are not constant over the rocket length, but can vary in consideration with the section in which they are evaluated. Thus, for a more accurate analysis, the variations along the rocket length can be evaluated with the load diagrams. Among the loads considered there are the aerodynamics forces, i.e. the lift and drag forces, the gravity force and the thrust. In addition to them, the Jet Damping and a simplified version of the thrust misalignments are also introduced in the loads equations. This because their presence causes significant differences in the maximum magnitude of the total applied loads and, thus, of the reactions of the main structure. The creation of the load diagrams allowed to infer how the analysed applied loads caused axial and shear forces and bending moments whose magnitudes are not sufficient to cause a structural failure.

Concluding, the rocket and all of its main components should withstand the applied loads during the flight phases and carry out the flight without major accidents.

To ensure the safety of the sounding rocket launch, the possible trajectories and failure modes have been deeply analysed. As a safety requirement, a casualty probability lower than 10^{-6} has been chosen. Due to the complexity in the determination of the casualty probability, the requirement has been changed in the probability of a land impact. Thus, the major safety requirement is a land probability lower than 10^{-6}. Moreover, another requirement on the rocket impact point is considered, the rocket should not fall more than 3 kilometres behind the launch site. The rocket trajectory has been simulated with a 6 Degree of Freedom code. The analyses have been divided into different categories with respect to the type of trajectory, which can be nominal or non-nominal, and the presence or absence of accidents. A non-nominal trajectory is determined when the flight path angle increases with time, or as an equivalent indicator when the axial velocity decreases with time during the burning phase. The safety analyses have focused on a Monte Carlo, on the wind influence, on the consequences of an HTP explosion, on the action of the Flight Termination System and on all those situations which could cause a land impact. As an overall result, the failure probability tables are created. From these, it is possible to determine the danger level represented by the different situations and confront it with the safety requirements.

As a first step, a Monte Carlo has been performed to determine the rocket nominal dispersion area. The possible manufacturing errors, parameters uncertainties and wind changes have been taken into account in the definition of the parameters variations to account for the non-linear effects of their possible combinations. With the results provided by these simulations, an impact envelope can be determined. Its dimensions have been evaluated to include at least the 99.7% of the impacts. For a better evaluation of the probability of an impact in a specific area, i.e. behind the launch site, the kernel density estimation has been used. This allows to transform a sharp impact point in an interval centred in the same point spreading the probability of the impact from its single sharp location to

the adjacent areas. The impact probabilities obtained with the different evaluation methods used are reported in the following table

	Behind Launch Site	*Behind* $-3\,km$
Most Probable Value	0.0092 %	0 %
90% Cumulative	0.0138 %	0.0019 %
Kernel Density $h = 1.5\,km$	0.0114 %	0.0009 %

The probability obtained from the kernel density reported in the table is evaluated with a bandwidth of $1.5\,km$, which is a good compromise since it allows to spread the impact influence on the surrounding area without losing too much information. Taking into account all the possible methods, an impact behind the launch site has a probability lower than $1.5{\cdot}10^{-4}$, while behind the $-3\,km$ the probability is lower than $2 \cdot 10^{-5}$. These probabilities are higher than the requirement. However, this is not a problem since they are evaluated without taking into account the presence of the Flight Termination System.

The wind has great effects on the rocket trajectory, thus, a thorough evaluation of its components, both in magnitude and direction, variations and influences is necessary. Bearing in mind the wind time variability, the correction of the launch angle with respect to the wind intensity is justified. The influence of possible wind changes as the rocket climbs higher in the atmosphere have been evaluated with the wind weighting function. It was shown how the wind accomplishes the 90% of its effects in the first $0.5\,km$. A change in the wind intensity from 0 to $5\,m/s$ above $1\,km$, causes a shift in the impact point of less than 5% from the reference value, i.e. whole trajectory without wind. In all analyses, the wind implemented is a longitudinal west-east wind. Lateral winds cause lateral deviations in the rocket trajectory, these can be balanced adjusting the azimuth launch angle. For safety reasons, no azimuth angles greater than 45° are allowed. Considering lateral winds up to $3\,m/s$, the correction in the launch angle can compensate for the deviations for all the elevation angles considered in the analyses except for the 85° case. With $0\,m/s$ and an elevation of 85° the lateral deviation cannot be cancelled, but it is limited to less than $4.5\,km$. In the evaluation of the influence of the lateral wind, it is important to

underline how the influence is mostly on the lateral component of the impact point, while on the longitudinal component the influence is negligible.

A possible, yet improbable explosion of the HTP stored in the tank of the sounding rocket has been assessed as of no threat for public safety above $1\,km$ from the explosion point. This result was obtained analyzing two main consequences, which are the overpressure deriving from the blastwave and the debris generated by the explosion and accelerated by the blast wave. Concentrating firstly on the blastwave overpressure, its value after $10\,m$ from the explosion origin has decreased in strength enough not cause casualties, and after $15\,m$ no injuries to people will occur. To avoid any possible dangers to buildings, a distance of $100\,m$ is necessary. The debris generated by the explosions can derive from the tank itself or from the adjacent parts, like the catalytic. Simulating the fragment ballistic trajectories after an explosion on the ground or as the rocket flying on a vertical path, all fragments should fall within $1\,km$ from the explosion point. Several safety margins have been introduced in this analysis and, thus, an improbable explosion should represent a possible threat within a smaller range than that reported. Among the safety margins introduced, there are the translation of the whole $60\,kg$ of HTP into $60\,kg$ of TNT, which should instead be much lower, and the drag coefficient of the fragments set to 0.5, corresponding to the coefficient of a sphere and, thus, lower than the others possible shapes the debris could have.

A destructive Flight Termination System is installed on the rocket to prevent it or any of its parts to reach areas where they could cause damages or casualties. The activation of the FTS causes the rocket to break into at least two main parts, it breaks the tank releasing the oxidizer left and it cuts the feeding line shutting-off the main engine. The two pieces of the rocket have lower ballistic coefficients than the full rocket, thus, reducing the distance travelled. The activation of the Flight Termination System has been simulated considering the human response time. A 3 *seconds* delay has been considered in case of a green code, i.e. a nominal trajectory, and a 1 *second* delay in case of an orange code, i.e. when there is a pre-alarm status because the rocket is following a non-nominal trajectory.

Considering all the possible accidental events the rocket can experience during its flight, two of them have shown the possibility of a ground im-

pact: the nozzle-turn malfunction and a fin loss. Also the Monte Carlo has provided several launches in which the rocket impacts the ground on land. These three situations have been deeply analyzed to better evaluate the threat they could pose to public safety. In the event of the Monte Carlo launches behind the launch site and of a nozzle-turn malfunction, the FTS should be activated, breaking the rocket into at least two main parts. In the event of a fin loss, the FTS activation is not required. From the results of the Monte Carlo, none of the launches fall behind the $-3\,km$. However, the FTS activation can break the rocket and prevent all parts so generated from moving backward. During these flights, no accidents occur and the rocket slowly changes its trajectory. Thus, the situation is an orange code and a delay of $0\,second$ after the rocket flight path angle has crossed the $90°$ is the most probable FTS activation time and all parts of the rocket in all cases fall forward the launch site. Even with a $1\,second$ activation, the fragments remain forward and with $3\,seconds$ the impacts are still within $100\,m$ behind the launch site. A nozzle-turn malfunction could cause the rocket to move backward and fall behind the launch site. The nozzle-turn is used to simulate two other major accidents whose effects on the rocket are similar: a motor-case burn through and a premature parachute opening. The nozzle-turn effects are simulated with a thrust misalignment of $15°$, which is a high and improbable value. However, it was chosen to add a safety margin to the simulations. A further safety margin is the fact that the nominal thrust value is considered to keep acting even after the nozzle-turn, which doesn't correspond to the real thrust after the accident. Considering a nominal trajectory and a $3\,seconds$ activation time for the FTS, in none of the cases analyzed the two rocket parts fall behind the launch site. Considering a non-nominal trajectory and a $1\,second$ activation time for the FTS, the two parts fall behind the launch site, but never behind the $-3\,km$ line as required. A fin loss could cause the rocket flight to become unstable. A fin loss is more probable at high velocities since the loads on the fins are higher. Thus, a fin loss directly after lift-off is improbable. If the rocket loses one fin it becomes unstable at high velocities, when it is more plausible to lose a fin, with two fins lost it is always unstable. After this accident the rocket starts tumbling and, during its motion, the velocity vector shifts in space and decreases in magnitude. The tilt angle has been evaluated for

different trajectories and times of accident. Evaluating the maximum angle of rotation of the velocity vector during the first half-rotation of the rocket, the tilt angle was always lower than 15°. In case of a fin loss on a nominal trajectory with a tilt angle of 15°, the rocket falls within a short distance from the launch site. To be more specific, if the fin loss happens within the first 10 seconds after lift-off, the rocket can fall 200 m behind the launch site, while if the fin loss happens after more than 10 seconds, the rocket falls forward. For the non-nominal trajectories, two different tilt angles have been used in the simulations. If a fin is lost within the first 20 seconds, the tilt angle is 15°, however, if the fin is lost after that moment the tilt angle is 5°. In both cases, the rocket falls behind the launch site, but never behind the $-3\,km$ line. Implementing the simulation with a tilt angle of 5° means lowering the safety margin. However, at high velocities, the real tilt angle experienced by the rocket is lower than the one implemented. Thus, even if the safety margin is lowered it is still present. Another safety margin present in all the fin loss simulations is the actual velocity of the rocket, this because the full velocity was considered to keep acting even after the accident. In reality, as the rocket tumbles it quickly slows down, decreasing the distance travelled. Moreover, the drag coefficient of the rocket on its ballistic trajectory after the loss was set to be equal to the coefficient with a 0 angle of attack, thus, the minimum value it could experience.

Considering all the possible situations which can cause the rocket to fall behind the launch site, it is possible to evaluate the danger level they represent in relation to their probability and to the impact location. Three levels are considered:

- *Low*: probability of the event to occur is below 10^{-6} or the rocket does not fall behind the launch site;
- *Medium* : probability of the event to occur is below $5 \cdot 10^{-4}$ and the rocket does not fall more than 3 km behind the launch site;
- *High*: probability of the event to occur is above $5 \cdot 10^{-4}$ or the probability of the event to occur is above 10^{-6} and the rocket falls more than 3 km behind the launch site.

It is possible to summarize all the different events in a failure probability

table. In it, for every event are listed the probability of the event and the relative impact point. With there two indicators it is possible to evaluate the danger level.

Launches Behind Launch site

Trajectory	*FTS Status*	|x|	*Probability*	*Danger*
Behind Launch site	Failure	$< 3\,km$	$< 5 \cdot 10^{-7}$	Low
Slant Range $> 3km$	Failure	$< 3\,km$	$< 10^{-7}$	Low
Behind Launch site	Works at $+0\,s$	*Forward*	$< 5 \cdot 10^{-4}$	Low
Behind Launch site	Works at $+1\,s$	*Forward*	$< 5 \cdot 10^{-4}$	Low
Behind Launch site	Works at $+3\,s$	$< 0.1\,km$	$< 5 \cdot 10^{-4}$	Medium

Nozzle-turn Malfunction

Trajectory	*FTS Status*	|x|	*Probability*	*Danger*
Nominal	Works	*Forward*	$< 5 \cdot 10^{-4}$	Low
Nominal	Fails	N/A	$< 5 \cdot 10^{-7}$	Low
Non-Nominal	Works	$< 3\,km$	$< 10^{-4}$	Medium
Non-Nominal	Fails	$< 3\,km$	$< 10^{-7}$	Low

Fin Loss

Trajectory	*FTS Status*	|x|	*Probability*	*Danger*
Nominal up to 10 s	N/A	$< 0.2\,km$	$< 5 \cdot 10^{-4}$	Medium
Nominal after 10 s	N/A	*Forward*	$< 5 \cdot 10^{-4}$	Low
Non-Nominal	N/A	$< 3\,km$	$< 10^{-4}$	Medium

Concluding, considering the Flight Termination System reliability, in no case the rocket has a probability of falling on the ground above 10^{-6} outside a 3 km perimeter around the launch pad. Thus, the probability of casualties is lower than the safety requirement.

Bibliography

[1] D. Altman and A. Holzman. Overview and history of hybrid rocket propulsion. *Progress in Astronautics and Aeronautics*, 218:1, 2007.

[2] J. Anthoine and M. Prévost. Hybrid propulsion: an overview of the onera activities. In *4th European Conference for Aero-Space Sciences*. EUCASS Association Belgium, 2011.

[3] J. Arves, M. Gnau, K. Joiner, D. Kearney, C. McNeal, and M. Murbach. Overview of the hybrid sounding rocket(hysr) project. *Powered Flight- The Next Century*, 2003.

[4] F. Barato. Numerical and experimental investigation of hybrid rocket motors transient behavior. 2013.

[5] B. A. Breech. Extension of the gurney equations to two dimensions for a cylindrical charge. Technical report, Army Research Lab Aberdeen Proving Ground MD Weapons and Materials Research, 2011.

[6] C. Butt, D. Padilha, J. Tisato, and S. Wilson. Determining appropriate failure response mode probabilities for high-altitude sounding rockets.

[7] D. D. Davis, L. A. Dee, B. Greene, S. D. Hornung, M. B. McClure, and K. A. Rathgeber. Fire, explosion, compatibility and safety hazards of hydrogen peroxide. 2005.

[8] M. Faenza, A. J. Boiron, B. Haemmerli, and C. J. Verberne. Development of the nucleus hybrid propulsion system: Enabling a successful flight demonstration. In *AIAA Propulsion and Energy 2019 Forum*, page 3839, 2019.

[9] M. Faenza, A. J. Boiron, B. Haemmerli, and C. J. Verberne. The nammo nucleus launch: Norwegian hybrid sounding rocket over 100km. In *AIAA Propulsion and Energy 2019 Forum*, page 4049, 2019.

[10] M. G. Faenza, A. J. Boiron, B. Haemmerli, L. Solli, O. Verberne, and T. Vesterås. Getting ready for space: Nammo's development of a 30 kn hybrid rocket based technology demonstrator. In *Proceedings of the 7th EUCASS conference, paper*, volume 410, 2017.

[11] N. Hu, X. Zhu, and C. Chen. Theoretical calculation of the fragment initial velocity following aerial explosion of the cylindrical warhead with two terminals. In *IOP Conference Series: Materials Science and Engineering*, volume 274, page 012049. IOP Publishing, 2017.

[12] A. Karabeyoglu, J. Stevens, D. Geyzel, B. Cantwell, and D. Micheletti. High performance hybrid upper stage motor. In *47th AIAA/ASME/SAE/ASEE Joint Propulsion Conference & Exhibit*, page 6025, 2011.

[13] D. Kearney, K. Joiner, M. Gnau, and M. Casemore. Improvements to the marketability of hybrid propulsion technologies. In *AIAA Space 2007 Conference & Exposition*, page 6144, 2007.

[14] R. KNIFFEN. Development status of the 200,000 lbf thrust hybrid rocket booster. In *Space Programs and Technologies Conference*, page 1657, 1992.

[15] T. Knop, J. Wink, R. Huijsman, R. Werner, J. Ehlen, S. Powell, B. Zandbergen, and A. Cervone. Failure mode investigation of a sorbitol-based hybrid rocket flight motor for the stratos ii sounding rocket. In *51st AIAA/SAE/ASEE Joint Propulsion Conference*, page 4133, 2015.

[16] W. H. Knuth, M. J. Chiaverini, J. A. Sauer, and D. J. Gramer. Solid-fuel regression rate behavior of vortex hybrid rocket engines. *Journal of Propulsion and power*, 18(3):600–609, 2002.

[17] M. Kobald, C. Schmierer, U. Fischer, K. Tomilin, and A. Petrarolo. A record flight of the hybrid sounding rocket heros 3. *Transactions*

of the Japan Society for Aeronautical and Space Sciences, Aerospace Technology Japan, 16(3):312–317, 2018.

[18] M. Kobald, C. Schmierer, U. Fischer, K. Tomilin, A. Petrarolo, and M. Rehberger. The hyend stern hybrid sounding rocket project. *Progress in Propulsion Physics–Volume 11*, 11:25–64, 2019.

[19] M. Military Handbook. Hdbk-762. *Design of aerodynamically stabilized free rockets*, 1990.

[20] A. Okninski. On use of hybrid rocket propulsion for sub-orbital vehicles. *Acta Astronautica*, 145:1–10, 2018.

[21] D. Ordahl and W. Rains. Recent developments and current status of hybrid rocket propulsion. *Journal of Spacecraft and Rockets*, 2(6): 923–926, 1965.

[22] J. E. Ronningen, J. Husdal, M. Berger, R. Vesterås, and G. Raudsandmoen. Nammo hybrid rocket propulsion trl improvement program. In *48th AIAA/ASME/SAE/ASEE Joint Propulsion Conference & Exhibit*, page 4311, 2012.

[23] M. Sadovsky. Mechanical effects of air shockwaves from explosions according to experiments. *Geophysics and Physics of Explosion (ed. MA Sadovsky), Nauka Press, Moscow*, 2004.

[24] C. Schmierer, M. Kobald, K. Tomilin, U. Fischer, M. Rehberger, and S. Schlechtriem. Heros-sounding rocket development by the hyend project. 2015.

[25] M. Stamatelatos, H. Dezfuli, G. Apostolakis, C. Everline, S. Guarro, D. Mathias, A. Mosleh, T. Paulos, D. Riha, C. Smith, et al. Probabilistic risk assessment procedures guide for nasa managers and practitioners. 2011.

[26] G. Story and J. Arves. Flight testing of hybrid-powered vehicles. *PROGRESS IN ASTRONAUTICS AND AERONAUTICS*, 218:553, 2007.

[27] Y. Wang, H. Wang, C. Cui, B. Zhao, and T. Xin. Damage analysis of explosion blast wave to rocket structure and payload. In *IOP Conference Series: Earth and Environmental Science*, volume 237, page 032060. IOP Publishing, 2019.

[28] S. Węglarczyk. Kernel density estimation and its application. In *ITM Web of Conferences*, volume 23, page 00037. EDP Sciences, 2018.

[29] J. R. Wertz, R. C. Conger, M. Rufer, N. Sarzi-Amadé, and R. E. Van Allen. Methods for achieving dramatic reductions in space mission cost. In *Reinventing Space Conference*, pages 2–6, 2011.

[30] P. Wilde, D. Murray, and J. Chrostowski. Catastrophe risk management and evaluation of maximum probable loss for launch vehicle explosions. In *33rd DoD Explosives Safety Seminar, Palm Springs, CA*, 2008.

[31] P. D. Wilde. Range safety requirements and methods for sounding rocket launches. *Journal of space safety engineering*, 5(1):14–21, 2018.

[32] P. D. Wilde, A. O. Weil, and C. Draper. A four degree of freedom malfunction trajectory analysis for public safety. *ESASP*, 680:96, 2010.

[33] P. D. Wilde, E. L. Morse, P. Rosati, and C. Cather. Probability of failure analysis standards and guidelines for expendable launch vehicles. *ESASP*, 715:42, 2013.

[34] R. Wubben, E. Gilleran, K. de Kievit, B. Kevers, M. van Heijningen, and M. C. Olde. Isasi 2019-investigation of the in-flight failure of the stratos iii sounding rocket.

[35] S. Yuasa, K. Yamamoto, H. Hachiya, K. Kitagawa, and Y. Oowada. Development of a small sounding hybrid rocket with a swirling-oxidizer-type engine. In *37th Joint Propulsion Conference and Exhibit*, page 3537, 2001.

[36] G. Zilliac. Hybrid rocket propulsion: Past, present, and future. *Presentation, November*, 2010.